



# UNIVERSIDAD DE INVESTIGACIÓN DE TECNOLOGÍA EXPERIMENTAL YACHAY

Escuela de Ciencias Físicas y Nanotecnología

## **TÍTULO: Spin Thermopower in Chiral Molecules**

Trabajo de integración curricular presentado como requisito para la  
obtención del título de Físico

### **Autor:**

Limaico Ibadango Franklin Ronaldo

### **Tutora:**

Ph.D - González Vázquez Gema

### **Cotutora:**

Ph.D - Varela Salazar Solmar Alexandra

Urcuquí, Noviembre 2024

# Autoría

Yo, **Franklin Ronaldo Limaico Ibadango**, con cédula de identidad 1004291223, declaro que las ideas, juicios, valoraciones, interpretaciones, consultas bibliográficas, definiciones y conceptualizaciones expuestas en el presente trabajo; así cómo, los procedimientos y herramientas utilizadas en la investigación, son de absoluta responsabilidad de el/la autor/a del trabajo de integración curricular. Así mismo, me acojo a los reglamentos internos de la Universidad de Investigación de Tecnología Experimental Yachay.

Urcuquí, Noviembre 2024.

---

Franklin Ronaldo Limaico Ibadango

CI: 1004291223

# Autorización de publicación

Yo, **Franklin Ronaldo Limaico Ibadango**, con cédula de identidad 1004291223, cedo a la Universidad de Investigación de Tecnología Experimental Yachay, los derechos de publicación de la presente obra, sin que deba haber un reconocimiento económico por este concepto. Declaro además que el texto del presente trabajo de titulación no podrá ser cedido a ninguna empresa editorial para su publicación u otros fines, sin contar previamente con la autorización escrita de la Universidad.

Asimismo, autorizo a la Universidad que realice la digitalización y publicación de este trabajo de integración curricular en el repositorio virtual, de conformidad a lo dispuesto en el Art. 144 de la Ley Orgánica de Educación

Urcuquí, Noviembre 2024.

---

Franklin Ronaldo Limaico Ibadango

CI: 1004291223

# Dedication

To my dear mother. This achievement is as much yours as it is mine.

Franklin Ronaldo Limaico Ibadango

# Acknowledgment

Firstly, I give thanks to the people who made this work possible, my advisor and co-advisors. Thanks to Dr. Gema Gonzáles, Dr. Solmar Varela, Dr. Rafael Gutierrez, and Dr. Mayra Peralta for their patience and the knowledge that they shared with me and for encouraging my passion for Physics from the beginning of my career. I am also grateful to my professors from the School of Physical Science and Nanotechnology: Wladimir, Helga, Henry, and Clara for rekindling my passion for Physics even more with their interesting classes this past semester. You all are my role models as a scientist and as a person.

To my mother, Elizabeth Limaico, for her unwavering support and faith. Thank you for being my pillar, my refuge, and for always believing in me. You showed me that if there is a thing that can transcend space and time, it is the love of a mother to her son.

To my friends who were there from the beginning of this journey; Bradley, Jeremy, Anthony, Saire, Santiago, and Mateo; who shared with me happy and sad moments. Finally, to all my career friends: Vicente, Brandon, Osmer, Daniel, Alexis, Lizbeth, Bryan, and others; who showed me that Physics is fun and with whom I have shared the dream of becoming a Physicist and leaving a mark on this world. All of you advised me never to give up and taught me the value of friendship and fellowship in all its facets. I sincerely wish you success in all your projects and dreams.

Franklin Ronaldo Limaico Ibadango

# Resumen

En el transporte de electrones, los efectos termoeléctricos en estructuras meso- y nanoscópicas han ganado relevancia en la Física y la Ingeniería gracias a su potencial para explotar los efectos cuánticos en controlar el acoplamiento de corrientes de calor y carga, con el objetivo de aprovechar el calor residual. En la espintrónica, el efecto de selectividad de espín inducida por quiralidad (en inglés CISS) es ampliamente estudiada para cuantificar el impacto de la quiralidad estructural de sistemas moleculares en los grados de libertad del espín para inducir polarización de espín sin la necesidad de introducir campos magnéticos externos. Ambos proporcionan un sólido tema de investigación casi inexplorado dentro de la caloritrónica de espín, los efectos térmicos sobre el transporte de carga y espín a través de moléculas quirales.

En esta tesis, investigamos el transporte dependiente de espín inducido por un gradiente de temperatura (efecto Seebeck de espín) en modelos fenomenológicos de dos terminales (electrodos) conectados a través de un sistema quiral simplificado en presencia de interacciones espín-órbita. Comenzamos utilizando el formalismo de Landauer basado en funciones de Green fuera del equilibrio para calcular la corriente de espín en dímeros tipo cable y establecer un punto de referencia para notar la filtración de espín en los casos de dímeros tipo quiral. Luego, después de calcular la termopotencia de espín sólo para los casos quirales (a través de una expansión de tipo Sommerfeld), encontramos que la termopotencia de espín se modifica ligeramente debido a la interferencia cuántica.

**Palabras Clave:**

Espín, carga, transporte, termopotencia, dímero, quiral

# Abstract

In electron transport, thermoelectric effects in meso-/nanoscopic structures have gained relevance in Physics and Engineering due to their potential to exploit quantum effects to control the coupling of heat and charge currents, with the aim of scavenging waste heat. In Spintronics, the Chirality-induced Spin Selectivity (CISS) effect is widely studied to quantify the impact of the structural chirality of molecular systems over the spin-dependent effects during the electron transport to induce spin polarization or spin filtering without the need of introducing external magnetic fields. Both provide a solid almost unexplored research subject within spin caloritronics, the thermal effects over the electron and spin transport through chiral molecules.

In this thesis, we investigate the spin-dependent transport induced by a temperature gradient (Spin Seebeck effect) in phenomenological models of two terminals (electrodes) connected through a simplified chiral system in the presence of spin-orbit interaction. We start with using the Landauer's formalism based on non-equilibrium Green functions to compute the spin current for wire-like dimers and to establish a reference in order to point out the spin filtering in the chiral-like dimer cases. Then, after computing the spin thermopower only for the chiral cases (via a Sommerfeld-type expansion), we find that spin thermopower gets slightly modified due to quantum interference.

**Keywords:**

Spin, charge, transport, thermopower, dimer, chiral

# Contents

<b>Dedication</b>	<b>iii</b>
<b>Acknowledgment</b>	<b>iv</b>
<b>Resumen</b>	<b>v</b>
<b>Abstract</b>	<b>vi</b>
<b>Contents</b>	<b>vii</b>
<b>List of Tables</b>	<b>ix</b>
<b>List of Figures</b>	<b>x</b>
<b>1 Introduction</b>	<b>1</b>
1.1 Problem statement . . . . .	3
1.2 Objectives . . . . .	3
1.2.1 General Objective . . . . .	3
1.2.2 Specific Objectives . . . . .	3
<b>2 Theoretical Framework</b>	<b>5</b>
2.1 Green Functions and Quantum Mechanics . . . . .	5
2.2 Second Quantization . . . . .	6
2.3 Equilibrium and Non-equilibrium Green Functions . . . . .	7
2.3.1 Equilibrium Green Functions . . . . .	7
2.3.2 Retarded GF for a Dimer . . . . .	12
2.3.3 Non-equilibrium Green Functions . . . . .	13
2.4 Quantum Transport Coefficients for Mesoscopic Tunneling Systems . . . . .	15

2.4.1	Two-Terminals transport system . . . . .	17
2.5	NEGF and Landauer-Büttiker Formalism . . . . .	22
2.6	Linear Non-equilibrium Thermodynamics and the Onsager Transport Coef- ficients . . . . .	25
2.6.1	Thermoelectric Phenomena . . . . .	25
2.6.2	Spin Thermoelectric Phenomena . . . . .	26
<b>3</b>	<b>Methodology</b>	<b>29</b>
3.1	Model Hamiltonian for Two-Terminals Transport . . . . .	29
3.2	Linear double-dot model . . . . .	30
3.3	T-shape model . . . . .	33
3.4	T-shape dimer model . . . . .	35
3.5	Michaeli-Geyer Model . . . . .	38
3.6	Extended Michaeli-Geyer Model . . . . .	41
<b>4</b>	<b>Results and Discussion</b>	<b>43</b>
4.1	Linear double-dot model: Landauer Transmission . . . . .	43
4.1.1	Contact polarization influence . . . . .	46
4.2	T-shape model: Anti- and Fano- resonances . . . . .	50
4.2.1	Contact polarization influence . . . . .	54
4.3	T-shape dimer model . . . . .	55
4.3.1	Contact polarization influence . . . . .	56
4.4	Michaeli-Geyer Model: CISS effect . . . . .	57
4.5	Extended Michaeli-Geyer model: Fano resonance and Spin Polarization . .	60
4.6	Thermopower analysis . . . . .	62
<b>5</b>	<b>Conclusions</b>	<b>67</b>
	<b>Bibliography</b>	<b>69</b>

# List of Tables

2.1	Langreth Rules for the analytic continuation. Adapted from [1] . . . . .	15
4.1	Max. amplitude for different polarization values . . . . .	49
4.2	Spin filtering behavior for chiral-like dimers . . . . .	62

# List of Figures

2.1	Schematic picture of a dimer model. The circles represent structures where electrons get confined (e.g., quantum dots) and thus contain discrete quantum levels. . . . .	13
2.2	Keldysh contour $C_k$ that is splitting into two branches: $C_{k_+}$ goes from $-\infty$ to $\infty$ and $C_{k_-}$ goes from $\infty$ to $-\infty$ . Adapted from [1]. . . . .	14
2.3	Mesoscale systems ordered in terms of the size. The systems are measured in terms of the nanoscale. Images extracted from: [2, 3, 4, 5, 6, 7, 8], a) to g) respectively. . . . .	17
2.4	Schematic general representation of the system treated in this work. Here L(R) refers to the left(right) contact, while $\Sigma_{L(R)}^r(E)$ is the retarded self-energy function that quantifies the tunneling of electrons from the contacts to the scattering region. In the scattering region, we can find structures like the dimer with horizontal or vertical orientation that will be treated in this thesis. . . . .	18
2.5	Scheme about the SE and SSE domains. We observe that the Spin Seebeck Effect (SSE) is limited to magnetic conductors. . . . .	28
3.1	The schematic representation for spin-dependent electron transport in a horizontal junction. Here L(R) refers to the left(right) contact from which free electrons tunnel in and out to the molecules, while $\Gamma_{L(R)}$ is the level width function that quantifies the tunneling from the contacts to the molecular junction, while the hopping $V$ quantifies the contribution of the mixed spatial states 1 and 2. . . . .	30

- 3.2 Schematic representation for the spin-dependent electron transport in a vertical junction. Here  $\Gamma_{L(R)}$  is the tunneling rate from the left to right contact while the hopping  $V$  quantifies the contribution of the mixed spatial states 1 and 2. . . . . 33
- 3.3 Schematic representation for the spin-dependent transport for an array of two laterally coupled double quantum dots (DQDs). Here  $\omega$  quantifies the mixed states contribution for the sites  $\{(0, 1), (1, 1)\}$  and  $\{(0, 2), (1, 2)\}$  while  $V$  quantifies the mixed states contribution for the sites  $\{(0, 1), (0, 2)\}$ . The generalization of this model for  $N$  laterally coupled DQDs is used for studies in thermal spin filters [9]. . . . . 35
- 3.4 Schematic representation of the Helical Cylinder system. Here  $\{\mathbf{t}, \mathbf{e}_1, \mathbf{e}_2\}$  refers to the rotated frame and  $\{\mathbf{t}, \mathbf{n}, \mathbf{b}\}$  refers to the Frenet frame, both basis vectors to parametrize the curve and global z-axis. Extracted from Ref.[10] . . . . . 39
- 4.1 Landauer Transmission for the linear double dot model; when  $\Delta = 0 meV$ ,  $\gamma = 0.5 meV$  and  $p_\alpha = 0$  ; for different values of the hopping term  $V$  in an energy interval of  $[-4, 4] meV$ , with a) The same site energies,  $\epsilon_1 = \epsilon_2 = 0 meV$ . b) Different site energies,  $\epsilon_1 = -0.5 meV$  and  $\epsilon_2 = 0.5 meV$ . The peaks from both figures are called resonances and represent the energy where the Transmission is the maximum (i.e.  $T_{max}$ ). . . . . 44
- 4.2 Landauer transmission for the double-dot model ( $\epsilon_1 = \epsilon_2 = 0 meV$ ,  $\Delta = 0 meV$ ,  $\gamma = 0.5 meV$  and  $V = 4\gamma$ ) for different polarization values  $p_\alpha$ . The solid line represents the total transmission profile while the dashed/dash-dot is for the spin up/down transmission. . . . . 47
- 4.3 Landauer Transmission for the linear double dot model ( $\epsilon_1 = \epsilon_2 = 0 meV$ ,  $\Delta = 0 meV$ ,  $\gamma = 0.5 meV$  and  $V = 4\gamma$ ) for polarization  $p_L = 1$  and  $p_R = 0$  in an energy interval of  $[-4, 4] meV$ . The transmission is divided into spin channels: a) for spin up, b) for spin down, and c) for the total contribution of a) and b). Transmission near the Fermi energy is allowed only for one spin channel. . . . . 50

- 4.4 Transmission for T-shape model; when  $\Delta = 0 \text{ meV}$ ,  $\gamma = 0.5 \text{ meV}$  and  $p_\alpha = 0$ . For different values of hopping term  $V$  within an energy interval of  $[-4, 4] \text{ meV}$ , we observe distinct Quantum Interference profiles. a) When the site energies are equal, e.g.,  $\epsilon_1 = \epsilon_2 = 0 \text{ meV}$  and  $V = 1 \gamma$  we have a case of antiresonance (symmetric shape). b) When the site energies are not equal, e.g.,  $\epsilon_1 = -0.5 \text{ meV}$  and  $\epsilon_2 = 0.5 \text{ meV}$  and  $V = 1 \gamma$  we have a case of Fano resonance (asymmetric shape). . . . . 51
- 4.5 Fano resonance for different values of polarization  $p_\alpha$ . Here, the solid line represents the total transmission profile while the dashed/dash-dot is for the spin up/down transmission. The parameters are:  $\epsilon_1 = -0.5 \text{ meV}$ ,  $\epsilon_2 = 0.5 \text{ meV}$ ,  $\Delta = 0$ ,  $\gamma = 0.5 \text{ meV}$  and  $V = 0.5 \gamma$  . . . . . 54
- 4.6 Quantum Interference profiles for the T-shape dimer model; when  $\epsilon_1^0 = \epsilon_2^0 = 0 \text{ meV}$ ,  $\epsilon_1^1 = \epsilon_2^1 = 1 \text{ meV}$ ,  $\Delta = 0 \text{ meV}$ ,  $\gamma = 0.5 \text{ meV}$ ,  $p_\alpha = 0$  and  $V = 4\gamma$ ; for different values of intra-hopping  $\omega$ . . . . . 55
- 4.7 Fano resonance for the T-shape dimer model; when  $\epsilon_1^0 = \epsilon_2^0 = 0 \text{ meV}$ ,  $\epsilon_1^1 = \epsilon_2^1 = 1 \text{ meV}$ ,  $\gamma = 0.5 \text{ meV}$ ,  $V = 4\gamma$  and  $\omega = 0.5\gamma$ ; for different values of polarization  $p_\alpha$ . Here, the solid line represents the total transmission profile while the dashed/dash-dot is for the spin up/down transmission. . . . . 57
- 4.8 Landauer transmission for the simplified chiral molecule [10] ( $n=2$  lattice sites case) for the angular momentum ( $L = 0, +1$ ),  $\epsilon_1 = \epsilon_2 = 0 \text{ meV}$ ,  $\gamma = 0.5 \text{ meV}$ ,  $t = 7\gamma$ ,  $\lambda_2 = 0.5$  and  $B = -2$ . The transmission is divided into spin channels: a) for spin up, b) for spin down, and c) for the total contribution of a) and b). When  $L = 0$ , we recover the linear double dot case (dashed lines); for  $L = +1$ , we have the CISS effect due to the coupling in the spin orbit term (solid line). . . . . 58
- 4.9 Spin Polarization (solid red line) and Landauer transmissions (dashed black and blue lines) for  $\epsilon_1 = \epsilon_2 = 0 \text{ meV}$ ,  $\gamma = 0.5 \text{ meV}$ ,  $t = 7\gamma$ ,  $\lambda_2 = 0.5$ ,  $B = -2$  and  $L = +1$ .  $T_{UP}$  highlights the Transmission for  $p_L = 1, p_R = 0$ .  $T_{DOWN}$  highlights the Transmission for  $p_L = -1, p_R = 0$ . . . . . 59

- 4.10 Landauer transmission (QI profiles) for the simplified chiral molecule [10] (n=2 lattice sites case), including side dots, for the angular momentum  $L = +1$ :  $\epsilon_1^0 = \epsilon_2^0 = 0 \text{ meV}$ ,  $\epsilon_1^1 = \epsilon_2^1 = 1 \text{ meV}$   $\gamma = 0.5 \text{ meV}$ ,  $t = 7\gamma$ ,  $\omega = 0.4\gamma$ ,  $\lambda_2 = 0.5$  and  $B = -2$ . For  $L = +1$  we have the spin filtering due to the coupling in the spin orbit term. Additionally, we have Fano resonances. . . . . 61
- 4.11 Spin Polarization (solid red line) and Landauer transmissions (QI profiles) for  $\epsilon_1^0 = \epsilon_2^0 = 0 \text{ meV}$ ,  $\epsilon_1^1 = \epsilon_2^1 = 1 \text{ meV}$   $\gamma = 0.5 \text{ meV}$ ,  $t = 7\gamma$ ,  $\omega = 0.4\gamma$ ,  $\lambda_2 = 0.5$  and  $B = -2$ .  $T_{UP}$  (dashed black line) highlights the transmission for  $p_L = 1$ ,  $p_R = 0$ .  $T_{DOWN}$  (dashed blue line) highlights the Transmission for  $p_L = -1$ ,  $p_R = 0$ . . . . . 62
- 4.12 Charge (red line) and Spin (blue line) thermopower for a) the Michaeli-Geyer model based on  $T_{UP}$ , b) based on  $T_{DOWN}$ , c) the Michaeli-extended model based on  $T_{UP}$  and d)  $T_{DOWN}$ . The analysis was performed under cryogenic conditions (approximately  $T = 3K$ ). . . . . 63
- 4.13 Charge (orange line) and Spin (blue line) thermopower for a) the linear double-dot model based on  $T_{UP}$ , b) based on  $T_{DOWN}$ , c) the T-shape dimer model based on  $T_{UP}$ , and d)  $T_{DOWN}$ . The analysis was performed under cryogenic conditions (approximately  $T = 3K$ ). . . . . 64

# Chapter 1

## Introduction

Thermoelectric (TE) effects allude to physical phenomena in which direct conversion of heat into electrical energy (or vice versa) is observed. The term refers to the Seebeck and Peltier effects, but our focus is on the first one. The Seebeck effect (SE), discovered by T.J Seebeck in 1821 [11], is when a temperature gradient produces an electromotive force (e.m.f) between two junctions when there is no electrical current. This effect is quantified by the Thermopower  $S$ , also called Thermoelectric Power or Seebeck Coefficient, which computes the ratio between the charge flow produced and temperature difference, in a case where there is no extra electric current [12]. Additionally, it reflects the coupling of heat and charge currents and it finds applications in thermometers, power generators and coolers.

On the other hand, spin is an intrinsic property related to angular momentum and it endows to particles with an intrinsic magnetic momentum due to their connection with electric charge, another intrinsic property. So, as the charge current, spin in the electrons can be transported between electrodes (contacts) even though there is no charge flow, it is the spin current [13]. However, special attention is given to manipulating the spin currents along with charge currents in materials, where such coupling can vary, which has spawned the Spintronics. This field is important because miniaturization, as it is described by Moore's Law [14], has boosted the manufacturing of spintronic devices to enhance the information storage, where the spin state of electrons can represent bits of data [15], through the creation of technologies based on those properties, such as magnetic tunnel junctions [16] and spin valves [17].

Heat currents can also interact with spin currents [18] from which the inter-field of spin caloritronics has been spawned, whose objective is to influence spin currents through temperature differences (or vice versa). Similar to the interaction between heat and charge currents, we focus on the Seebeck effect studies in which depending on how the temperature gradient is applied, we obtain two types of spin-based Seebeck effect. Firstly, the spin-dependent Seebeck effect (SDSE), where a spin-dependent transport happens in bulk materials directly due to the temperature differences [18, 19]. Secondly, the Spin Seebeck effect (SSE) that is a two-step process happening at interface systems where a ferromagnetic (FM) material, that produces a spin polarized current (spin current generator), is connected to a nonmagnetic (NM) material (spin sink) through an intermediate interface [18]. SSE offers unique advantages for 'green' technologies compared to the TE effects, as the optimization process is different for both. For TE systems, the strengthening (optimization) of the electronic part usually leads to the weakening of the thermal part and vice versa. On the other hand, in SSE, the optimization is handled separately into the thermal-magnetic properties of the spin current generator and the electronic properties of the spin sink [19].

A highly relevant research area within spintronics and spin caloritronics is the *Chiral Induced Spin Selectivity* (CISS) effect, discovered in 1999 by Naaman et al. [20]. The CISS effect refers to an unusual phenomenon where the polarization of a current is produced by geometries that break parity symmetry (called chiral) [21]. Chirality is not only found in molecules like DNA but also in non-helical molecules such as enantiomers. In those cases, we can physically understand the CISS effect as an electron scattering process in systems where the spin of the electrons takes a relevant role in terms of the handedness of the molecule. For instance, the enhancement (diminishment) in the transmission rates for electrons with spin up (down) in right-handed molecules and the opposite for left-handed molecules. Some sources allude to a more formal description, as an electron scattering process in a system with strong spin-orbit interactions and where both space inversion and time-reversal invariance are broken [22]. In any case, it is a broad field of study applied to asymmetry reactions [23][24], model spin transport over spin-based tunneling phenomena [25], conduction in DNA structures [26], transport under magnetic field perturbation [27], among others.

## 1.1 Problem statement

The SSE has been extensively investigated in interface systems mediated by semiconductors, metallic-like materials, and similar bulk systems. However, investigations addressing SSE in chiral structures are rare. Such structures display high spin filtering, an effect denoted as Chirality-Induced Spin Selectivity (CISS). Additionally, the possible influence of quantum interference effects, which are ubiquitous in nano- and mesoscale systems, deserve a closer investigation in conjunction with spin-dependent transport. In this study, we develop a minimal theoretical model for wire- and chiral- like dimers to address the impact of the CISS effect and quantum interference on the SSE. The model studies in this Thesis contribute to the understanding of the physics behind spintronic devices that incorporate discrete quantized states in the scattering region such as molecular junctions and molecular transistors.

## 1.2 Objectives

### 1.2.1 General Objective

This thesis aims to clarify qualitatively and theoretically the SE and SSE over 2 terminal-*s*/contacts toy models whose mediator (scattering region) has discrete quantized states and can perform spin filtering in the presence of spin-orbit interactions (CISS effect). Then, the influence of quantum interference effects over the SE and SSE in the same models will be analyzed.

### 1.2.2 Specific Objectives

- To derive in a consistent way the equations for the quantum transport from the Green's function formalism
- To derive in a consistent way the equations for the thermopower  $S$  and spin thermopower  $S^s$  from the Green based transmission functions by using Sommerfeld expansion.
- To use the Green's function technique to compute the electron and spin transport in

toy models that do not polarize the spin alignment (wire-like dimer models).

- To compare the electron and spin transport results of the previous models with a simplified chiral model that presents spin filtering based on the CISS effect (chiral-like dimer model).
- To propose a modified chiral-like model that includes quantum interference effects.
- To compare the thermopower and spin thermopower of the models which present spin filtering.

# Chapter 2

## Theoretical Framework

The aim of this chapter is to introduce and discuss the general theoretical background employed in this work. The starting point is a brief introduction to the Non-Equilibrium Green's Functions technique and the derivation of the Landauer transmission for mesoscopic systems. Then, the derivation of thermoelectric coefficients, in particular of the thermopower, is provided in terms of the moments of the Landauer transmission function.

### 2.1 Green Functions and Quantum Mechanics

Within nonrelativistic quantum mechanics, the state of a given physical system can be described by the Schrödinger equation:

$$i\hbar \frac{\partial}{\partial t} \Psi(\vec{r}, t) = \mathbf{H} \Psi(\vec{r}, t), \quad (2.1)$$

where  $\mathbf{H} = -\frac{\hbar^2}{2m} \nabla^2 + V(\vec{r}, t)$  is the Hamiltonian of the system. However, Eq.(2.1) is a partial differential equation, which, depending on the  $V(\vec{r}, t)$  shape, becomes hard to solve analytically. Additionally, Eq.(2.1) is challenging to solve computationally when we are treating with many-electron atoms or with molecules because of the many-body nature of the problem.

An equivalent formulation of the Schrödinger equation, which can be exploited to develop perturbative treatments, can be achieved by introducing Green's function (GF), thus treating Eq.(2.1) as a Sturm-Liouville operator problem (i.e. eigenvalue operator

problem)[28]:

$$\Rightarrow \left[ i\hbar \frac{\partial}{\partial t} + \frac{\hbar^2}{2m} \nabla^2 \right] \Psi(\vec{r}, t) = V(\vec{r}, t) \Psi(\vec{r}, t). \quad (2.2)$$

Finding a simplified solution for Eq. (2.2) involves treating  $V(\vec{r}, t) \Psi(\vec{r}, t)$  as the inhomogeneous source. The idea is to solve Eq.(2.1) by using the solution for the free case, i.e. when there is no external potential  $V(\vec{r}, t)$ . Then, the formal solution can be written as:

$$\Rightarrow \Psi(\vec{r}, t) = \int G(\vec{r}, t; \vec{r}', t') \Psi(\vec{r}', t') V(\vec{r}', t') d^3\vec{r}' dt', \quad (2.3)$$

where  $G(\vec{r}, t; \vec{r}', t')$  is the Green function that must satisfy:

$$\left[ i\hbar \frac{\partial}{\partial t} + \frac{\hbar^2}{2m} \nabla^2 \right] G(\vec{r}, t; \vec{r}', t') = \delta(\vec{r} - \vec{r}') \delta(t - t').$$

It should be noted that Eq.(2.3) pertains to the free particle case. Consequently, the wave function can be evaluated iteratively from the equation (2.3) in the sense of perturbation theory. Alternatively, Green's function can be directly solved perturbatively using the Dyson equation method, which will be elaborated in the chapter 2.4. This concept is important in this work because the resulting transmission in phenomenological models (e.g. the linear double-dot model from chapters 3.2 and 4.1) are computed by considering the flow of free particles through a scattering region (i.e. molecules).

Additional to the highly computational power that Green's functions performs due to iteration, it is worth to mention that in Quantum Mechanics such functions usually are interpreted as the mathematical representation of the propagator for single particles [29].

## 2.2 Second Quantization

In the second quantized approach, particles are treated as Quantum Fields. In summary, most physics is contained in the operators rather than in the states [29] and such a framework provides a theoretical frame in which the idea of occupation number within an associated Fock space is introduced, and creation and annihilation operators are defined. The Hamiltonian from the Schrödinger equation (2.1) is then reformulated in terms of creation (annihilation) operators  $c_i^\dagger$  ( $c_i$ ) and the respective solutions for (2.1) are reformulated in terms of the same ones. These operators must satisfy, in the case of fermions, the

anticommutation relations:

$$\begin{aligned}\{c_i, c_i\} &= \{c_i^\dagger, c_i^\dagger\} = 0, \\ \{c_i, c_j^\dagger\} &= \{c_j^\dagger, c_i\} = \delta_{ij},\end{aligned}\tag{2.4}$$

where the curly brackets are the anticommutators:

$$\{a, b\} = ab + ba.$$

The physical interpretation is that  $c_i^\dagger$  creates a particle on state  $i$  in the Fock space, for a given quantum property (e.g. position, spin, momentum, etc), while  $c_j$  annihilates a particle on the state  $j$  (for the same property).

## 2.3 Equilibrium and Non-equilibrium Green Functions

Green's functions are not only a mathematical tool but also have physical significance. In Quantum Mechanics, Green's function is interpreted as the propagator for the probability amplitudes (i.e. solutions to eq.(2.1) or namely the wavefunction  $\Psi(\vec{r}, t)$ ) from one point to another in space-time [29] and, in the context of second quantization, as the propagator of the quantum field operators. Depending on whether we are considering systems in thermodynamic equilibrium or situations where transport processes take place, we can define two types of Green functions: equilibrium GF and non-equilibrium (or Keldysh) GF.

### 2.3.1 Equilibrium Green Functions

Equilibrium Green's functions are implemented to solve a Hamiltonian that describes quantum systems in thermodynamic equilibrium. When we define a quantum system to be analyzed, we must include thermal baths and particle reservoirs (both playing the role of the environment) connected to the quantum system, i.e., it becomes an open quantum system. In this regard, we say the system is in equilibrium if there are no flows of any type involved.

We begin the resolution process by using the interaction picture representation to split

the Hamiltonian:

$$H = H_0 + V, \quad (2.5)$$

where  $H_0$  is the exact solvable term and  $V$  is the hard to solve perturbation that represents many body interactions, with both terms being time independent due to the separation of the wavefunction into temporal and stationary part.

Once the Hamiltonian is expressed in terms of second quantization formalism, we need to include propagation characteristics. So, we use the Feynman Green's functions definition based on the Wick-Time ordering symbol  $T$  [29]:

$$G(\vec{r}, t; \vec{r}', t') = -i\langle T [\Psi(\vec{r}, t)\Psi^\dagger(\vec{r}', t')] \rangle,$$

$$G(\vec{r}, t; \vec{r}', t') = -i\Theta(t - t')\langle \Psi(\vec{r}, t)\Psi^\dagger(\vec{r}', t') \rangle + i\Theta(t' - t)\langle \Psi^\dagger(\vec{r}', t')\Psi(\vec{r}, t) \rangle, \quad (2.6)$$

where the brackets  $\langle \dots \rangle$  for an operator (in interaction picture)  $O(t) = e^{\frac{i}{\hbar}H_0t} O e^{-\frac{i}{\hbar}H_0t}$  are a thermodynamic average using the Grand-canonical density matrix  $\rho = e^{-\beta(H-\mu N)} / \text{Tr}(e^{-\beta(H-\mu N)})$  because we are dealing with a system at finite temperatures, which in turn depends on the Hamiltonian given by equation (2.5) [1]:

$$\langle O(t) \rangle \equiv \frac{\text{Tr} \left( e^{-\beta(H-\mu N)} O(t) \right)}{\text{Tr} \left( e^{-\beta(H-\mu N)} \right)}, \quad (2.7)$$

where  $N$  is the occupation number operator and  $\beta = \frac{1}{k_B T}$ .

In Condensed Matter Physics, Eq.(2.6) is called Time-Ordered Green Function, Causal Green Function or Finite-Temperature Green Function [1]. It represents the motion of the field operator  $\Psi$  from  $(\vec{r}, t)$  to  $(\vec{r}', t')$  and the motion of the field operator  $\Psi^\dagger$  from  $(\vec{r}', t')$  to  $(\vec{r}, t)$ . Green's functions allow for a perturbation expansion because the Hamiltonian is constructed in a manner that aligns with the perturbation scheme [1]

Additionally, for reasons that will be explained later, we define the Lesser and Greater Green's functions from Eq.(2.6) as follows:

$$\begin{aligned} G^<(\vec{r}, t; \vec{r}', t') &= i\langle \Psi^\dagger(\vec{r}', t')\Psi(\vec{r}, t) \rangle, \\ G^>(\vec{r}, t; \vec{r}', t') &= -i\langle \Psi(\vec{r}, t)\Psi^\dagger(\vec{r}', t') \rangle, \end{aligned} \quad (2.8)$$

then, we rewrite Eq.(2.6) in terms of (2.8):

$$G(\vec{r}, t; \vec{r}', t') = \Theta(t - t')G^>(\vec{r}, t; \vec{r}', t') + \Theta(t' - t)G^<(\vec{r}, t; \vec{r}', t').$$

Also retarded and advanced Green's functions can be defined as:

$$\begin{aligned} G^r(\vec{r}, t; \vec{r}', t') &\equiv -i\Theta(t - t')\langle\{\Psi(\vec{r}, t), \Psi^\dagger(\vec{r}', t')\}\rangle = \Theta(t - t')\left(G^>(\vec{r}, t; \vec{r}', t') - G^<(\vec{r}, t; \vec{r}', t')\right), \\ G^a(\vec{r}, t; \vec{r}', t') &\equiv i\Theta(t' - t)\langle\{\Psi(\vec{r}, t), \Psi^\dagger(\vec{r}', t')\}\rangle = -\Theta(t' - t)\left(G^>(\vec{r}, t; \vec{r}', t') - G^<(\vec{r}, t; \vec{r}', t')\right), \end{aligned} \quad (2.9)$$

where equations (2.8) and (2.9) are taken from Ref.[1] for the case of fermions.

In order to obtain information about the temporal evolution for Green's Functions, the (Heisenberg) equation of motion technique for the corresponding time-dependent creation/annihilation operators can be used:

$$\begin{aligned} i\frac{d\mathbf{O}(t)}{dt} &= [\mathbf{O}, \mathbf{H}] \\ \frac{d\mathbf{O}(t)}{dt} &= i[\mathbf{H}, \mathbf{O}] \end{aligned} \quad (2.10)$$

where  $\mathbf{O}$  is an operator,  $\mathbf{H}$  is the total Hamiltonian of the system and  $\hbar = 1$  (natural units). In the case of time-independent Hamilton operators, a Fourier transform to the energy space can be further defined as:

$$\begin{aligned} G(E) &= \mathcal{F}\{G(t, t')\} = \int_{-\infty}^{\infty} G(t) e^{iE(t-t')} dt, \\ G(t, t') &= \mathcal{F}^{-1}\{G(E)\} = \frac{1}{2\pi} \int_{-\infty}^{\infty} G(E) e^{-iE(t-t')} dE, \end{aligned} \quad (2.11)$$

following the convention of Zubarev [30].

For example, for a system of noninteracting free electrons, there is an associated Kinetic Energy Hamiltonian (2.12):

$$H_{kin} = \sum_k \epsilon_k c_k^\dagger c_k, \quad (2.12)$$

where  $c_k^\dagger(c_k)$  creates (annihilates) an electron in the eigenstate  $k$ , corresponding to the wavenumber  $\vec{k}$ , and  $\epsilon_k$  is the associated eigenvalue, in this case is the dispersion relation ( $\epsilon_k = \frac{\hbar^2 k^2}{2m}$ ).

As we know, the Green's functions are associated to the operators  $c_k^\dagger$  and  $c_k$  from  $H_{kin}$ . So, we have to extract information about the temporal evolution of such operators, by using the equation of motion technique (2.10):

$$\begin{aligned}\frac{dc_k}{dt} &= -i[c_k, H_{kin}] = -i\epsilon_k c_k \Rightarrow c_k(t) = e^{-i\epsilon_k t} c_k, \\ \frac{dc_k^\dagger}{dt'} &= -i[c_k^\dagger, H_{kin}] = i\epsilon_k c_k^\dagger \Rightarrow c_k^\dagger(t') = e^{i\epsilon_k t'} c_k^\dagger,\end{aligned}$$

so, we can define the causal Green's function as:

$$G_k(t, t') = -i\langle T [c_k(t), c_k^\dagger(t')] \rangle, \quad (2.13)$$

having the retarded and advanced Green's function as:

$$G_k^r(t, t') = -i\Theta(t - t') \langle \{c_k(t), c_k^\dagger(t')\} \rangle = -i\Theta(t - t') e^{-i\epsilon_k(t-t')} \delta_{kk}, \quad (2.14)$$

$$G_k^a(t, t') = i\Theta(t' - t) \langle \{c_k(t), c_k^\dagger(t')\} \rangle = i\Theta(t' - t) e^{i\epsilon_k(t'-t)} \delta_{kk},$$

and the lesser and greater Green's functions as:

$$G_k^<(t, t') = i\langle c_k^\dagger(t') c_k(t) \rangle = i e^{i\epsilon_k(t'-t)} \langle c_k^\dagger c_k \rangle,$$

$$G_k^>(t, t') = -i\langle c_k(t) c_k^\dagger(t') \rangle = -i e^{-i\epsilon_k(t-t')} \langle c_k c_k^\dagger \rangle.$$

The retarded and advanced GFs are useful to calculate physical responses of the system such as DOS (density of states), scattering rates and spectral properties [1]. On the other hand, the lesser and greater GFs are useful to compute kinetic properties, i.e. the observables of the system, such as particle densities or currents (directly related to quantum transport phenomena)[1].

For example, for the retarded Green's function for the noninteracting free electrons case, we can convert it to the energy space by taking the integral representation of the Heaviside Function [30]:

$$\Theta(t - t') = \frac{i}{2\pi} \int_{-\infty}^{\infty} dE \frac{e^{-iE(t-t')}}{E + i\eta},$$

over Eq.(2.14) (remember  $\delta_{kk} = 1$ ):

$$G_k^r(t, t') = \frac{1}{2\pi} \int_{-\infty}^{\infty} dE \frac{e^{-i(E+\epsilon_k)(t-t')}}{E + i\eta},$$

where, using the change of variable  $E \rightarrow E - \epsilon_k$ , we obtain:

$$G_k^r(t, t') = \frac{1}{2\pi} \int_{-\infty}^{\infty} dE \frac{e^{-iE(t-t')}}{E - \epsilon_k + i\eta}.$$

Finally, by comparing with the Fourier Transform (2.11), the resulting retarded Green's function in the energy space for  $G_k^r(t, t')$  is obtained:

$$\Rightarrow G_k^r(E) = \frac{1}{E - \epsilon_k + i\eta}. \quad (2.15)$$

Notice that the denominator in equation (2.15) contains the poles of the retarded Green's function and they represent the energy eigenvalues of the state  $k$ . For this specific case ( $H = H_{kin}$ ), we rename the Green's function as the Free Green's functions  $G_k(E)$ 's. According to Ref.[1], these functions are the building blocks for the perturbation series used to solve more complex Hamiltonians. This is because, in general,  $H = H_{kin} + V$ , where  $V$  encodes many-body interactions.

For example, we consider the Hamiltonian for  $N$  confined non-interacting electrons:

$$H = \sum_n^N \epsilon_n c_n^\dagger c_n + \sum_{n,m}^N (V c_n^\dagger c_m + h.c.), \quad (2.16)$$

so, we can define the retarded Green's function as:

$$G_{nm}^r(t, t') = -i\Theta(t - t') \langle \{c_n(t), c_m^\dagger(t')\} \rangle. \quad (2.17)$$

and use the equation of motion technique (2.10) to obtain information about the temporal evolution of  $G_{nm}^r(t, t')$ :

$$\begin{aligned} i \frac{\partial}{\partial t} G_{nm}^r(t, t') &= \delta(t - t') \delta_{nm} - i\Theta(t - t') \langle \{i\dot{c}_n(t), c_m^\dagger(t')\} \rangle, \\ \Rightarrow i \frac{\partial}{\partial t} G_{nm}^r(t, t') &= \delta(t - t') \delta_{nm} - i\Theta(t - t') \langle \{[c_n, H], c_m^\dagger\} \rangle, \end{aligned} \quad (2.18)$$

we solve the equation (2.18) by solving the commutator operation:

$$[c_n, H] = \left[ c_n, \sum_{n'}^N \epsilon_{n'} c_{n'}^\dagger c_{n'} + \sum_{n',m'}^N (V c_{n'}^\dagger c_{m'} + h.c.) \right] = \epsilon_n c_n + \sum_{n',m'}^N V (\delta_{nn'} c_{m'} + \delta_{nm'} c_{n'}),$$

and thus, the anticommutator operation:

$$\begin{aligned} \{[c_n, H], c_m^\dagger\} &= \left\{ \epsilon_n c_n + \sum_{n',m'}^N V (\delta_{nn'} c_{m'} + \delta_{nm'} c_{n'}), c_m^\dagger \right\} \\ \Rightarrow \{[c_n, H], c_m^\dagger\} &= \epsilon_n \{c_n, c_m^\dagger\} + \sum_{n',m'}^N V \left( \delta_{nn'} \{c_{m'}, c_m^\dagger\} + \delta_{nm'} \{c_{n'}, c_m^\dagger\} \right), \end{aligned}$$

we obtain as a result:

$$i \frac{\partial}{\partial t} G_{nm}^r(t, t') = \delta(t - t') \delta_{nm} + \epsilon_n G_{nm}^r(t, t') + \sum_{n',m'}^N V \left( \delta_{nn'} G_{m'm}^r(t, t') + \delta_{nm'} G_{n'm}^r(t, t') \right). \quad (2.19)$$

We can use the Fourier Transform and then some reordering to convert the differential equation (2.19) into a set of algebraic equations:

$$G_{nm}^r(E) = \delta_{nm} G_n^r(E) + \sum_{n',m'}^N V G_n^r(E) G_{m'm}^r(E) \delta_{nn'} + \sum_{n',m'}^N V G_n^r(E) G_{n'm}^r(E) \delta_{nm'}, \quad (2.20)$$

where  $G_n^r(E) = \frac{1}{E - \epsilon_n + i\eta}$  is the Free Green's function.

### 2.3.2 Retarded GF for a Dimer

In chemistry, dimer refers to a molecule composed of two identical molecules called monomers, for example, the nitrogen dioxide ( $\text{NO}_2$ ) forming dinitrogen tetroxide ( $\text{N}_2\text{O}_4$ ) at lower temperatures. Alternatively, in solid-state physics, dimer refers to a theoretical model used to investigate the interaction or hybridization between two relevant structures, not necessarily molecules. For instance, it might represent two relevant orbitals in a molecule chain, a dimer (as a molecule), two quantum dots, two atoms, etc.

In this work, we will consider the dimer (model) as electrons confined in two certain locations called sites  $\{\epsilon_1, \epsilon_2\}$ , see Fig.2.1. So, we can derive such a model from the Hamiltonian for  $N$  confined non-interacting electrons by considering the states  $n(m)$  as spatial states (i.e., positions in the dimer), hybridization with neighbor sites and  $N = 2$  confined

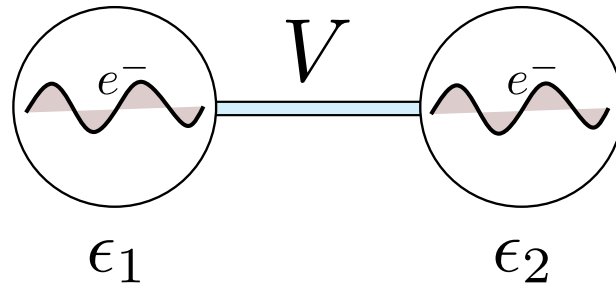


Figure 2.1: Schematic picture of a dimer model. The circles represent structures where electrons get confined (e.g., quantum dots) and thus contain discrete quantum levels.

non-interacting electrons, then the Hamiltonian will be:

$$H = \sum_n^2 \epsilon_n c_n^\dagger c_n + \sum_n^1 (V c_n^\dagger c_{n+1} + h.c.). \quad (2.21)$$

where *h.c.* stands for the *hermitian conjugate*, an operation that reverses the order and applies complex conjugation. In this case, the hermitian conjugate of  $V c_n^\dagger c_{n+1}$  is *h.c.* =  $V^* c_{n+1}^\dagger c_n = V c_{n+1}^\dagger c_n$  as  $V$  is a real number. So, the retarded Green Function for this case will be:

$$G_{nm}^r(E) = G_n^r(E) \delta_{nm} + V G_n^r(E) G_{2m}^r(E) \delta_{n1} + V G_n^r(E) G_{1m}^r(E) \delta_{n2}. \quad (2.22)$$

Since our terminology is focused on the physical standpoint, we will refer to dimer as a model from now on. It will be explicitly mentioned the cases when we refer to dimer as a molecule. Finally, this model will play a central role in chapter 3.

### 2.3.3 Non-equilibrium Green Functions

Although systems in thermodynamic equilibrium provide a useful framework for solving open quantum systems, it is crucial to recognize that such a condition is an idealized construct. Every system encountered in daily life are out of equilibrium. In the context of the open quantum system, the defining characteristic of a non-equilibrium system is the presence of not compensating flows. Consequently, the study of nonequilibrium systems primarily focuses on transport phenomena and thus the implementation of Non-equilibrium Green's functions (NEGF), also called Keldysh-Green's functions.

NEGF are Green's functions implemented to solve a hamiltonian that describes a system

that is out of the thermodynamic equilibrium. Therefore, the construction will be, in principle, different from the equilibrium case by the fact that the constant flow of matter or energy introduces mathematically a time dependence in the system. If so, the Hamiltonian will be restructured to take into account such time dependence [1]:

$$H = h + H'(t), \quad (2.23)$$

where  $h \equiv H_0 + V$  is the Hamiltonian from the equilibrium case, and  $H'(t)$  is the time-dependent perturbation referring to the source. Examples of such sources include an electric field, a light excitation pulse, or, as assumed in this work, the connection of two contacts (terminals) at different (electro)chemical potentials.

Including additional term  $H'(t)$  necessitates its incorporation into the density matrix  $\rho$  and Green's functions, resulting in more complex transformations than the equilibrium case. Fortunately, as asserted in Refs.[1, 31], both Equilibrium Green's Function (EGF) and Nonequilibrium Green's Function (NEGF) theories can be rendered structurally equivalent. This structural equivalence has been leveraged in additional studies (Refs.[32, 33, 34, 7]). Consequently, NEGF operates fundamentally analogous to the equilibrium theory, with the unique distinction being the replacement of real-axis integrals with contour integrals.

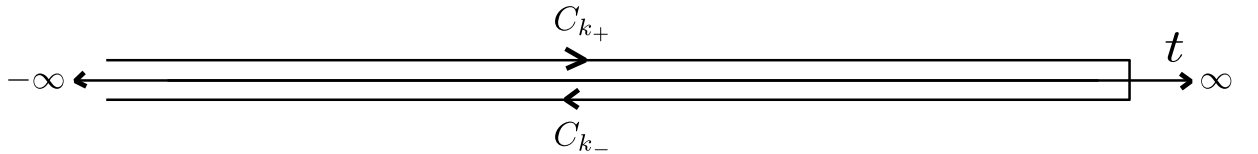


Figure 2.2: Keldysh contour  $C_k$  that is splitting into two branches:  $C_{k+}$  goes from  $-\infty$  to  $\infty$  and  $C_{k-}$  goes from  $\infty$  to  $-\infty$ . Adapted from [1].

The Keldysh Green Function is defined by taking both time labels to follow over two contour branches according to Fig.2.2:

$$G(t, t') = -i \langle T_{C_k} [\Psi(t) \Psi^\dagger(t')] \rangle, \quad (2.24)$$

where now the time ordering is over a path called the Keldysh contour. Additionally, the causal Green function is defined as well:

$$G_{Ck}(t, t') = -i \langle T [\Psi(t) \Psi^\dagger(t')] \rangle, \quad t, t' \in C_{k+}, \quad (2.25)$$

Table 2.1: Langreth Rules for the analytic continuation. Adapted from [1]

Contour	Real Axis
$C = \int_C AB$	$C^< = \int_t [A^r B^< + A^< B^a]$ $C^r = \int_t A^r B^r$
$D = \int_C ABC$	$D^< = \int_t [A^r B^r C^< + A^r B^< C^a + A^< B^a C^a]$ $D^r = \int_t A^r B^r C^r$
$C(\tau, \tau') = A(\tau, \tau')B(\tau, \tau')$	$C^< = A^<(t, t')B^<(t, t')$ $C^r = A^<(t, t')B^r(t, t') + A^r(t, t')B^<(t, t')A^r(t, t')B^r(t, t')$
$D = A(\tau, \tau')B(\tau, \tau')$	$D^< = A^<(t, t')B^>(t', t)$ $D^< = A^<(t, t')B^a(t', t) + A^r(t, t')B^<(t', t)$

notice that (2.25) is the same expression as (2.6) and, therefore, the same as the example (2.13) from the previous subchapter.

Now, we must deal with contour integrals in a complex time. Fortunately, we can use the Langreth Theorem, which, using the analytic continuation, asserts to correlate complex time contour integrals with real-time integrals [1]. Some of the main results of applying this theorem over Green functions are shown in the Table 2.1.

Additionally, the treatment in Ch.2.3.1 was based on identifying the retarded Green's function and working over it. However, in the non-equilibrium case, it is better to use the causal Green's function (which in this work it will be referred just as Green's function from now on) because it contains all the other Green's functions.

## 2.4 Quantum Transport Coefficients for Mesoscopic Tunneling Systems

Transport phenomena involve the transfer of electrons that contain properties like charge, spin, energy, mass, etc, between different parts of a system. And, as it was mentioned before, the Non-equilibrium Green's functions (NEGF) provide a very flexible analytical framework to compute transport coefficients [1].

Using the equation of motion technique over NEGF leads to the Dyson Equation which

(usually) is presented in the following form:

$$G(\tau, \tau') = G_0(\tau, \tau') + \int d\tau_1 G_0(\tau, \tau_1)U(\tau_1)G(\tau_1, \tau') + \int d\tau_1 \int d\tau'' G_0(\tau, \tau_1)\Sigma(\tau_1, \tau'')G(\tau'', \tau'), \quad (2.26)$$

where  $\tau$  represents the complex time ( $t$  represent the real time). It is also assumed a one-body external potential  $U$  that represents the non-equilibrium term in the Hamiltonian and the irreducible Self-Energy  $\Sigma[G]$  standing for the interactions [1].

Eq.(2.21) from the Ch.2.3.2 has the corresponding Dyson Equation from the perturbation expansion of the Green's function:

$$G_{nm}(\tau, \tau') = \delta_{nm} \int d\tau_1 \delta(\tau, \tau_1)G_n(\tau_1, \tau') + \delta_{n1}V \int d\tau_1 G_n(\tau, \tau_1)G_{2m}(\tau_1, \tau') + \delta_{n2}V \int d\tau_1 G_n(\tau, \tau_1)G_{1m}(\tau_1, \tau'), \quad (2.27)$$

that, after applying the Langreth Rules (Table 2.1) and then Fourier Transform, Eq.(2.22) is recovered.

In general, once the required Green Function is defined, the NEGF technique lies in using the equation of motion technique to get the Dyson Equation (2.26) from a perturbation expansion. Then, making use of Langreth Rules and Fourier Transform over it to get the matrix form of the Dyson equation:

$$\mathbf{G}^r(E) = \mathbf{G}_0^r(E) + \mathbf{G}_0^r(E)\mathbf{\Sigma}^r(E)\mathbf{G}^r(E), \quad (2.28)$$

where  $\mathbf{G}_0^r(E)$  is the unperturbed retarded Green Function matrix which is composed of free retarded Green's functions  $G_0^r(E)$ , Eq.(2.15), and  $\mathbf{\Sigma}^r(E)$ , that is defined as the retarded self energy function. Consequently, equation (2.28) corresponds to the matrix generalization for non-equilibrium systems of Eq.(2.20).

Until now, we are not mentioned anything relevant related to the scale lengths in our derivations, e.g. the dimer model from section 2.3.2. The only thing that we know is the systems are sufficiently small to consider the effects of quantum mechanics and thermodynamics. Alternatively, the works related to quantum transport coefficients have been performed within a defined size scale, the mesoscopic. It refers to a size range that lies between nano-scale and micro-scale [35]. While other definitions asserts that it pertains to

material scales larger than a "few of atoms but not large enough to be ohmic" [31].

In any case, since this thesis takes the works performed in dimers (molecules) [2], molecular systems [3, 36, 37, 38, 39, 40] and quantum dots [41, 42, 4, 43, 44, 9] as reference for quantum transport coefficients computations, we will define the mesoscale systems in terms of the definition of Ref. [31]. However, we will restrict ourselves to those that contain bound states and where quantum tunneling plays a significant role. Regarding the scale order of such systems, we have the first row of Fig.2.3. In the second row, we observe higher size systems, as a result, the methods that we will employ in this work can also be applied to those systems as they also contain bound states in some manner, e.g., the helical polymer from Ref.[8].

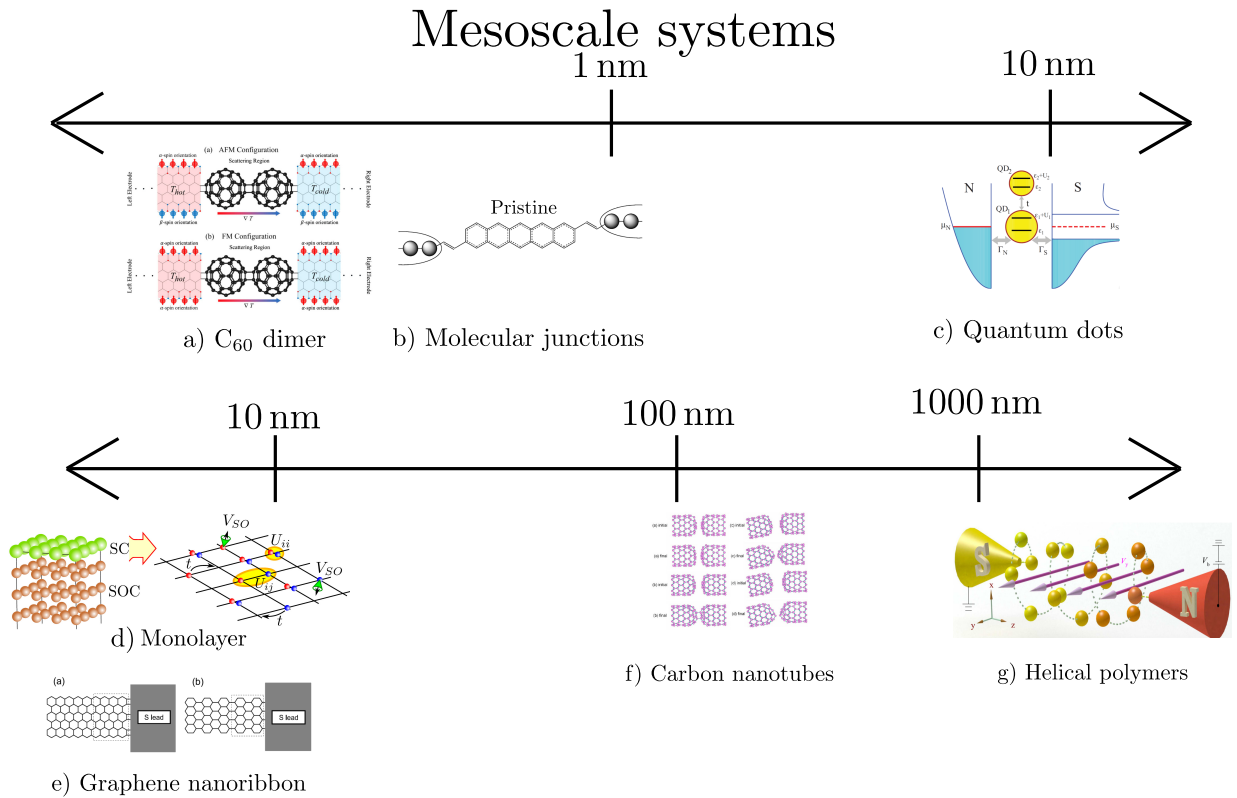


Figure 2.3: Mesoscale systems ordered in terms of the size. The systems are measured in terms of the nanoscale. Images extracted from: [2, 3, 4, 5, 6, 7, 8], a) to g) respectively.

### 2.4.1 Two-Terminals transport system

Now, we define the system that we will work from now on. Fig.(2.4) shows the general structure that we will consider and that match with the systems of the first row in Fig.2.3.

It is made of two contacts with different electrochemical potentials that produce a voltage and then a current, connected to a central region where the quantum wave scattering process is performed. The idea is to treat both contacts and the scattering region as decoupled systems at thermal equilibrium [1] in which the electrons are localized in the case of the central region and delocalized in the case of the contacts. Then, we include a coupling (tunneling) between regions and contacts through the retarded self-energy for the left(right) contact  $\Sigma_{L(R)}^r(E)$ . In this way, we obtain a system that describes the transport of electrons between regions in thermal equilibrium, i.e., the overall system is now out of equilibrium.

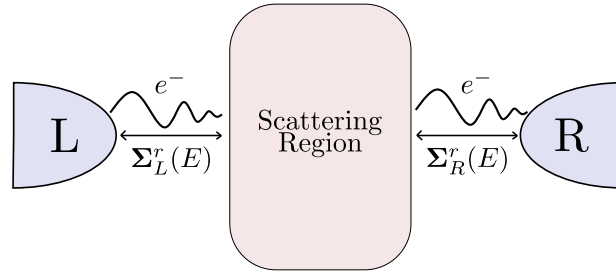


Figure 2.4: Schematic general representation of the system treated in this work. Here L(R) refers to the left(right) contact, while  $\Sigma_{L(R)}^r(E)$  is the retarded self-energy function that quantifies the tunneling of electrons from the contacts to the scattering region. In the scattering region, we can find structures like the dimer with horizontal or vertical orientation that will be treated in this thesis.

From Fig.2.4, we define the Hamiltonian form once solving techniques (i.e. Dyson equation) were introduced. The Hamiltonian splits into three regions:  $H = H_c + H_{cen} + H_T$ . Here  $H_c$ ,  $H_{cen}$  and  $H_T$  stand for the contacts (i.e., left and right electrodes), the structure between the contacts (i.e., the scattering region) and the coupling between the contacts and the center, respectively [1]. Each piece is usually set up as follows:

- The contact Hamiltonian is written in such way that it produces non-interacting electrons.

$$H_c = \sum_{k, \alpha \in \{L, R\}} \epsilon_{k\alpha} c_{k\alpha}^\dagger c_{k\alpha}, \quad (2.29)$$

- The tunneling Hamiltonian is written in such a way that it produces creation and annihilation particles in both electrodes and scattering region.

$$H_T = \sum_{k, \alpha \in \{L, R\}} V_{k\alpha, m} c_{k\alpha}^\dagger d_m + h.c., \quad (2.30)$$

- The central region has a variety of shapes to ensemble the respective Hamiltonian. Here some examples provided by [1]:

- For a central region which consist of noninteracting levels:

$$H_{cen} = \sum_m \epsilon_m d_m^\dagger d_m. \quad (2.31)$$

- For a central region which couples charge carriers to phonons:

$$H_{cen}^{el-ph} = \epsilon_0 d^\dagger d + d^\dagger d \sum_{\vec{q}} M_{\vec{q}} [a_{\vec{q}}^\dagger + a_{-\vec{q}}], \quad (2.32)$$

Here,  $a_{\vec{q}}^\dagger(a_{\vec{q}})$  creates (destroys) a phonon in mode  $\vec{q}$ .

- For a central region produced by the Anderson-type model for electron interactions in the central region.

$$H_{cen} = \sum_{\sigma} \epsilon_0 d_{\sigma}^\dagger d_{\sigma} + U n_{\uparrow} n_{\downarrow}, \quad (2.33)$$

Here,  $\sigma$  states a label for the spin state, while  $n_{\sigma}$  is the occupation number operator of spin-state  $\sigma$  and  $U$  describes the on-site Coulombic repulsion. If we computed the Green function of this Hamiltonian, without taking into account  $H_c$  and  $H_T$ , we would notice the lack of Kondo behavior because of the lack of the correlation term with free electrons.

Notice that the central section has rich options that provide plenty of variety of systems to work on. Also, this background establishes the base for the derivation of the quantum transport coefficients for mesoscopic systems in general.

Now, following the idea from Ch.2.3.1 about observables of the system, let's compute the electron current  $J$  for mesoscopic systems in general by using NEGF. For the setup (Fig. 2.4), the current  $J$  is obtained from the occupation number operator over one of the contacts e.g. left contact  $N_L$ . In such a case, to obtain more information about  $N_L$

behavior, we need to compute the time derivative of it. So, using the equation of motion technique (2.10), the electron current expression derivation starts from the definition of the current for the left contact ( $J_L$ ) which is written as the time derivative of the occupation number operator  $N_L$ :

$$J_L = -e\langle \dot{N}_L \rangle = -\frac{ie}{\hbar} \langle [H, N_L] \rangle, \quad (2.34)$$

where  $N_L = \sum_{k,\alpha \in L} c_{k\alpha}^\dagger c_{k\alpha}$  and  $H = H_c + H_T + H_{cen}$ . Using the commutation relations from Eq.(2.4) results in  $[H, N_L] = [H_T, N_L]$  which, defining new Green's functions i.e. Eq.(2.36), leads to:

$$\begin{aligned} J_L &= \frac{ie}{\hbar} \sum_{\substack{k,\alpha \in L \\ n}} [V_{k\alpha,n} \langle c_{k\alpha}^\dagger d_n \rangle - V_{k\alpha,n}^* \langle d_n^\dagger c_{k\alpha} \rangle], \\ &= \frac{2e}{\hbar} Re \left[ \sum_{\substack{k,\alpha \in L \\ n}} V_{k\alpha,n} G_{n,k\alpha}^<(t,t) \right], \end{aligned} \quad (2.35)$$

where:

$$\begin{aligned} G^<(t,t') &\equiv i \langle c_{k\alpha}^\dagger(t') d_n(t) \rangle, \\ G^<(t,t') &\equiv i \langle d_n^\dagger(t) c_{k\alpha}(t') \rangle, \end{aligned} \quad (2.36)$$

Additional, the derivation of  $G_{n,k\alpha}^<(t,t)$  over Eq.(2.35) comes from the time diagonal components and the property  $G_{k\alpha,n}^<(t,t) = -[G_{n,k\alpha}^<(t,t)]^*$  of the Green Functions (2.36).

Next step is to derive an expression for  $G^<(t,t')$ . The equation of motion technique (2.10) with Langreth Rules and Fourier Transform are used over the Green Function  $G(t,t')$  which leads to:

$$\begin{aligned} G_{n,k\alpha}^<(t,t') &= \sum_m V_{k\alpha,m}^* \int \frac{dE}{2\pi} [G_{nm}^r(E) g_{k\alpha}^<(E) + G_{nm}^<(E) g_{k\alpha}^a(E)] \exp[-iE(t-t')], \\ \Rightarrow G_{n,k\alpha}^<(t,t) &= \sum_m V_{k\alpha,m}^* \int \frac{dE}{2\pi} [G_{nm}^r(E) g_{k\alpha}^<(E) + G_{nm}^<(E) g_{k\alpha}^a(E)], \end{aligned}$$

and replacing in (2.35) leads to:

$$J_L = \frac{2e}{\hbar} \int \frac{dE}{2\pi} Re \left\{ \sum_{\substack{k,\alpha \in L \\ n,m}} V_{k\alpha,n} V_{k\alpha,m}^* [G_{nm}^r(E) g_{k\alpha}^<(E) + G_{nm}^<(E) g_{k\alpha}^a(E)] \right\}, \quad (2.37)$$

where:

$$\begin{aligned}
g^<(t-t') &= i\langle c_{k\alpha}^\dagger(t')c_{k\alpha}(t)\rangle, \\
&= if(\epsilon_{k\alpha}^0)\exp[-i\epsilon_{k\alpha}(t-t')], \\
g^{r,a}(t-t') &= \mp i\Theta(\pm t \mp t')\langle\{c_{k\alpha}(t), c_{k\alpha}^\dagger(t')\}\rangle, \\
&= \mp i\Theta(\pm t \mp t')\exp[-i\epsilon_{k\alpha}(t-t')],
\end{aligned} \tag{2.38}$$

here  $f(\epsilon_{k\alpha}) = [\exp[(\epsilon_{k\alpha} - \mu_\alpha/k_B T)] + 1]^{-1}$  is the equilibrium Fermi Distribution in a given contact [1].

Moreover, the electrode Self-energies ( $\Sigma$ ) are introduced to convert the summations related to momentum (i.e.  $k$ ) into a single expression:

$$\begin{aligned}
\Sigma_{\alpha,mn}^<(E) &= \sum_k V_{k\alpha,m}^* V_{k\alpha,n} g_{k\alpha}^<(E), \\
\Sigma_{\alpha,mn}^{r,a}(E) &= \sum_k V_{k\alpha,m}^* V_{k\alpha,n} g_{k,\alpha}^{r,a}(E).
\end{aligned} \tag{2.39}$$

Applying (2.39) to (2.37), and after rewriting, the following is obtained:

$$J_L = \frac{2e}{\hbar} \int \frac{dE}{2\pi} \text{Re} \left\{ \text{Tr} \left( \mathbf{G}^r(E) \Sigma_L^<(E) + \mathbf{G}^<(E) \Sigma_L^a(E) \right) \right\}, \tag{2.40}$$

by using some relations and identities from the Green functions, equation (2.40) leads to the general current expression from the left contact:

$$J_L = \frac{e}{\hbar} \int \frac{dE}{2\pi} \text{Tr} \left\{ \mathbf{G}^>(E) \Sigma_L^<(E) - \mathbf{G}^<(E) \Sigma_L^>(E) \right\}, \tag{2.41}$$

for  $J_R$  is an analogous process:

$$J_R = \frac{e}{\hbar} \int \frac{dE}{2\pi} \text{Tr} \left\{ \mathbf{G}^>(E) \Sigma_R^<(E) - \mathbf{G}^<(E) \Sigma_R^>(E) \right\}. \tag{2.42}$$

Finally, considering steady state, the total current will be uniform which leads to  $J_L = -J_R$  [1]. Such fact allows us to symmetrize the current ( $J = J_L + J_L = J_L - J_R$ ) which leads to a general expression for the current:

$$J = \frac{e}{\hbar} \int \frac{dE}{2\pi} \text{Tr} \left\{ \mathbf{G}^>(E) \left( \Sigma_L^<(E) - \Sigma_R^<(E) \right) - \mathbf{G}^<(E) \left( \Sigma_L^>(E) - \Sigma_R^>(E) \right) \right\}, \tag{2.43}$$

with:

$$\mathbf{G}^{<, >}(E) = \mathbf{G}^r(E) \left( \Sigma_{\text{int}}^{<, >}(E) + \Sigma_L^{<, >}(E) + \Sigma_R^{<, >}(E) \right) \mathbf{G}^a(E),$$

where  $\Sigma_{\text{int}}^{<, >}$  is the lesser/greater self energy due to interactions within the central region. Depending on the constant factor in the symmetrization, e.g.  $J = \frac{(J_L + J_R)}{2} = \frac{(J_L - J_R)}{2}$ , it is possible obtain:

$$J = \frac{e}{2\hbar} \int \frac{dE}{2\pi} \text{Tr} \left\{ \mathbf{G}^>(E) \left( \Sigma_L^<(E) - \Sigma_R^<(E) \right) - \mathbf{G}^<(E) \left( \Sigma_L^>(E) - \Sigma_R^>(E) \right) \right\}. \quad (2.44)$$

Both versions are valid but we will use (2.43) from now on.

## 2.5 NEGF and Landauer-Büttiker Formalism

The Landauer formula refers to a quantum approximation in which the main quantity to be computed is the transmission function from one contact to another without taking into account the state or shape of the central region [31]. In such approximation, the expression for the current is obtained following the Büttiker equation [31], this leads to the formula used in the Landauer-Büttiker (L-B) formalism:

$$J = \frac{2e}{\hbar} \int \frac{dE}{2\pi} (f_L(E) - f_R(E)) T, \quad (2.45)$$

where  $T$  is related to the quantum mechanical transmission coefficient [32, 26, 45, 34, 46, 31].

On the other hand, the NEGF formalism consists of using Eq.(2.43) to compute the transport between contacts. Unlike the L-B formalism, NEGF takes into account the shape of the central region by considering the interactions that can occur within it. Examples of such interacting central regions are the Hamiltonian (2.32), which involves electron-phonon interactions, and (2.33) which involves electron-electron interactions. As we can infer, NEGF can, in principle, lead to the L-B formalism if we restrict ourselves to the case of a non-interacting central region.

To arrive at a general expression relating current and transmission of L-B, we start

with the general expression for the current from NEGF (2.43):

$$J = \frac{e}{\hbar} \int \frac{dE}{2\pi} \text{Tr} \left\{ \mathbf{G}^>(E) \left( \boldsymbol{\Sigma}_L^<(E) - \boldsymbol{\Sigma}_R^<(E) \right) - \mathbf{G}^<(E) \left( \boldsymbol{\Sigma}_L^>(E) - \boldsymbol{\Sigma}_R^>(E) \right) \right\}.$$

For the case of non-interacting central region, we introduce new expressions:

$$\begin{aligned} \mathbf{G}^<(E) &= \mathbf{G}^r(E) \left( \boldsymbol{\Sigma}_L^<(E) + \boldsymbol{\Sigma}_R^<(E) \right) \mathbf{G}^a(E), \\ \mathbf{G}^>(E) &= \mathbf{G}^r(E) \left( \boldsymbol{\Sigma}_L^>(E) + \boldsymbol{\Sigma}_R^>(E) \right) \mathbf{G}^a(E), \\ \boldsymbol{\Sigma}_\alpha^<(E) &= i f_\alpha(E, \mu_\alpha) \boldsymbol{\Gamma}_\alpha(E), \\ \boldsymbol{\Sigma}_\alpha^>(E) &= -i (1 - f_\alpha(E, \mu_\alpha)) \boldsymbol{\Gamma}_\alpha(E), \end{aligned} \tag{2.46}$$

where  $f_\alpha(E, \mu_\alpha)$  is the Fermi-Dirac distribution:

$$f_\alpha(E, \mu_\alpha) = \frac{1}{\exp\left(\frac{E - \mu_\alpha}{k_B T_\alpha}\right) + 1},$$

and,  $\boldsymbol{\Gamma}_\alpha(E)$  is the level width function. We will use  $\boldsymbol{\Gamma}_\alpha(E)$  as the function to quantify the coupling (tunneling) between the non-interacting regions from now on.

Finally, replacing (2.46) over (2.43) and after some algebra, the electronic current is obtained:

$$\begin{aligned} J &= \frac{2e}{\hbar} \int \frac{dE}{2\pi} (f_L(E, \mu_L) - f_R(E, \mu_R)) \text{Tr} \left\{ \mathbf{G}^r(E) \boldsymbol{\Gamma}_L(E) \mathbf{G}^a(E) \boldsymbol{\Gamma}_R(E) \right\}, \\ \Rightarrow J &= \frac{2e}{\hbar} \int \frac{dE}{2\pi} (f_L(E, \mu_L) - f_R(E, \mu_R)) T(E), \end{aligned} \tag{2.47}$$

where  $T(E)$  is the *Landauer Transmission*:

$$T(E) \equiv \text{Tr} \left\{ \mathbf{G}^r(E) \boldsymbol{\Gamma}_L(E) \mathbf{G}^a(E) \boldsymbol{\Gamma}_R(E) \right\}. \tag{2.48}$$

In the remaining thesis, the main goal will be to explicitly calculate the Landauer transmission function for different model systems. Since the spin degree of freedom will play a crucial role in our investigation, we have to generalize the previous developments to include the spin label in the operators, i.e.  $c_{n\sigma}^\dagger(c_{n\sigma})$ , with  $\sigma = \{\uparrow, \downarrow\}$  being the spin label. This leads to:

$$T(E) = \text{Tr} \left\{ \mathbf{G}^r(E) \boldsymbol{\Gamma}_L(E) \mathbf{G}^a(E) \boldsymbol{\Gamma}_R(E) \right\} = \sum_{\sigma} T_{\sigma}(E), \tag{2.49}$$

where  $T_\sigma(E)$  is the spin-dependent Landauer Transmission that is determined by the explicit solution of the required system. Henceforth, the Green's function formula for the charge current previously derived (2.47) becomes:

$$J^e \equiv J = \sum_\sigma \frac{e}{\hbar} \int \frac{dE}{2\pi} (f_L(E, \mu_L) - f_R(E, \mu_R)) T_\sigma(E), \quad (2.50)$$

and the spin current:

$$J^s = \sum_\sigma \frac{1}{\hbar} \int \frac{dE}{2\pi} \left( \hat{\sigma} \frac{\hbar}{2} \right) (f_L(E) - f_R(E)) T_\sigma(E), \quad (2.51)$$

where  $\sigma = \{\uparrow, \downarrow\}$  is the spin label and  $\hat{\sigma} = \{+, -\}$  is the mathematical operator for up and down spin respectively. And it is also worth deriving the energy current or also called the heat current:

$$J^h = \sum_\sigma \frac{1}{\hbar} \int \frac{dE}{2\pi} (E - \mu_L) (f_L(E) - f_R(E)) T_\sigma(E). \quad (2.52)$$

It is worth mentioning that this formalism encompasses only coherent transport because the electrons involved do not interact with any particles, resulting in no phase-breaking processes occurring [31, 47]. Thus, the presence of interactions within the central region play a crucial role in determining whether the transport is coherent or non-coherent.

In general, the NEGF formalism for transport serves as an alternative quantum approximation method akin to the Landauer-Büttiker (L-B) formalism. The key distinction between the two lies in the scope of electron transport behavior considered: while the L-B formalism accounts exclusively for coherent transport the NEGF formalism can encompass both components of the transport phenomena [31]: the coherent and non-coherent. Given that our focus will be restricted to coherent transport, both approximations become equivalent.

Lastly, although both approximations lie in the same regime, NEGF is chosen for its suitability in numerical computations. Given the Hamiltonian of the scattering region  $H_{cen}$  and the level-width function per contact  $\Gamma_\alpha(E)$ , Eq.(2.48) can be directly applied to evaluate the current. If a phase-breaking process or more complex shapes for the contacts need to be included, it would require additional effort to determine the appropriate retarded self-energy function  $\Sigma_\alpha^r(E)$ , but this is a one-time effort [47], resulting in a method that is both mechanical and straightforward.

## 2.6 Linear Non-equilibrium Thermodynamics and the Onsager Transport Coefficients

The linear regime for Nonequilibrium Thermodynamics refers to a system that is close to equilibrium. In such approximation, linear relations are assumed between the forces and flows through constant coefficients called Onsager coefficients [12]:

$$J_k = \sum_j L_{kj} F_j.$$

In such a framework, simplifications derived by Onsager are included  $L_{ij} = L_{ji}$ . It leads to the Symmetry Principle which states that *"macroscopic causes always have fewer or equal symmetries than effects they produce"*. It allows us to restrict the force-flow coupling that helps in the construction of the phenomenological framework.

### 2.6.1 Thermoelectric Phenomena

In general terms, TE phenomena involve thermal gradients producing not only heat flow but also electrical currents and vice-versa. Such effects can be described by linear phenomenological laws for bulk systems as [45]:

$$\begin{aligned} J^e &= L_{ee} \frac{\Delta V}{T} + L_{eh} \frac{\Delta T}{T^2}, \\ J^h &= L_{he} \frac{\Delta V}{T} + L_{hh} \frac{\Delta T}{T^2}. \end{aligned} \quad (2.53)$$

Considering now the expressions for charge and heat current from the NEGF formalism (with  $J \equiv J^e$ ):

$$\begin{aligned} J^e &= \frac{2e}{\hbar} \int \frac{dE}{2\pi} (f_L(E) - f_R(E)) T(E), \\ J^h &= \frac{2}{\hbar} \int \frac{dE}{2\pi} (E - \mu_L) (f_L(E) - f_R(E)) T(E), \end{aligned} \quad (2.54)$$

and using an expansion around the electrochemical potential  $\mu$  (Fermi Energy) and temperature  $T$  up to linear order in applied electric potential and temperature differences (i.e. Sommerfeld-type expansion) leads to the phenomenological laws for meso- and nanoscopic

systems:

$$\begin{aligned} J^e &= \Delta\mu e L_0 + \frac{\Delta T}{T} e L_1, \\ J^h &= \Delta\mu L_1 + \frac{\Delta T}{T} L_2, \end{aligned} \tag{2.55}$$

where  $L_n$  are moments of the Landauer transmission and thus, provide explicit expressions for the Onsager coefficients in a non-interacting quantum mechanical system in contact with heat and particle reservoirs:

$$L_n \equiv \frac{2}{\hbar} \int \frac{dE}{2\pi} (E - \mu)^n \left( -\frac{\partial f}{\partial E}(E, \mu) \right) T(E).$$

From Eq.(2.55) expressions for the familiar transport coefficients can be derived: the (isothermal) electric conductance  $G$ , the thermal conductance  $K$  and the thermopower, or also called *Seebeck coefficient*  $S$  [45].

For example, the Seebeck coefficient is deduced by considering a case where, knowing there is no charge current  $J^e = 0$ , a voltage bias ( $\Delta V$ ) appears by the presence of a temperature difference ( $\Delta T$ ), so:

$$S = - \left( \frac{\Delta V}{\Delta T} \right)_{J^e=0} = \frac{1}{eT} \frac{L_1}{L_0}.$$

Another example, we have the thermal conductance which is deduced by computing the ration between the heat current and temperature difference in a case where there is no charge current:

$$\kappa = \left( \frac{J^h}{\Delta T} \right)_{J^e=0} = \frac{1}{T} \left[ L_2 - \frac{L_1^2}{L_0} \right].$$

From now on, the Seebeck effect (and its spin version) will be the focus in this work as we are concentrated only in the thermopower and spin thermopower analysis.

## 2.6.2 Spin Thermoelectric Phenomena

When spin dependence is involved in the phenomenological law formulae, the linear response approximation around the electrochemical potential  $\mu$  and temperature  $T$  is applied over equations (2.50) to (2.52), so that the Onsager coefficients become in general

spin dependent.

$$\begin{aligned}
J^e &= \sum_{\sigma} \Delta\mu e L_{0\sigma} + \sum_{\sigma} \frac{\Delta T}{T} e L_{1\sigma}, \\
J^s &= \frac{\hbar}{2} \sum_{\sigma} \hat{\sigma} \Delta\mu L_{0\sigma} + \frac{\hbar}{2} \sum_{\sigma} \hat{\sigma} \frac{\Delta T}{T} L_{1\sigma}, \\
J^h &= \sum_{\sigma} \Delta\mu L_{1\sigma} + \sum_{\sigma} \frac{\Delta T}{T} L_{2\sigma},
\end{aligned} \tag{2.56}$$

where:

$$L_{n\sigma} \equiv \frac{1}{\hbar} \int \frac{dE}{2\pi} (E - \mu)^n \left( -\frac{\partial f}{\partial E}(E, \mu) \right) T_{\sigma}(E). \tag{2.57}$$

In conclusion, once the retarded Green function is found, the Landauer Transmission (2.48) is obtained, and it allows to compute the thermoelectric coefficients eventually including the spin degree of freedom.

In this way, the so-called Seebeck Effect (SE) is a phenomenon where, knowing there is no charge and spin current, a voltage bias ( $\Delta V$ ) appears in the presence of a temperature difference. The Seebeck (Thermopower) coefficient  $S$  is the voltage ( $\Delta V$ ) and temperature difference ( $\Delta T$ ) ratio when  $J^e = 0$  and  $J^s = 0$ :

$$S = \left( \frac{\Delta V}{\Delta T} \right)_{J^e=0, J^s=0} = -\frac{1}{2eT} \left( \frac{L_{1\uparrow}}{L_{0\uparrow}} + \frac{L_{1\downarrow}}{L_{0\downarrow}} \right), \tag{2.58}$$

and it is useful to compute the efficiency of conversion from heat to electric current.

The *Spin Seebeck coefficient*  $S^s$  is the spin voltage ( $\Delta V^s$ ) and temperature difference ( $\Delta T$ ) ratio when  $J^e = 0$  and  $J^s = 0$ :

$$S^s = \left( \frac{\Delta V^s}{\Delta T} \right)_{J^e=0, J^s=0} = -\frac{1}{2eT} \left( \frac{L_{1\uparrow}}{L_{0\uparrow}} - \frac{L_{1\downarrow}}{L_{0\downarrow}} \right), \tag{2.59}$$

and it quantifies the efficiency of conversion from heat into spin current. The so called Spin Seebeck Effect (SSE). A physical interpretation is given by the case where, knowing there is no charge and spin current, a spin current potential denoted by  $\frac{\mu_{\uparrow} - \mu_{\downarrow}}{e}$  [48], spin voltage bias ( $\Delta V^s$ ), appears produced by a temperature gradient.

Finally, we organize the regimes of influence due to heat for the SE and SSE in the following scheme, see Fig.2.5. From this figure, we conclude that both SE and SSE occur in similar systems. However, while SE occurs in any conductor, the SSE is limited to

magnetic conductors, where the spin of the electrons plays a significant role.

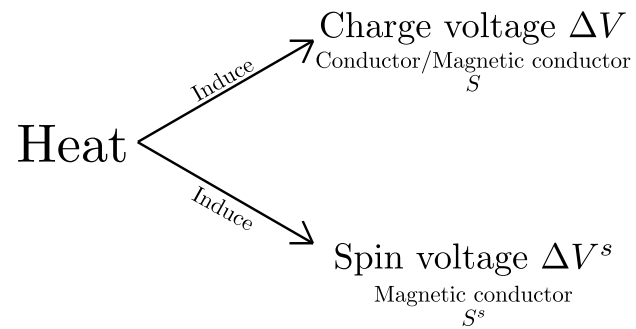


Figure 2.5: Scheme about the SE and SSE domains. We observe that the Spin Seebeck Effect (SSE) is limited to magnetic conductors.

# Chapter 3

## Methodology

In this chapter, the mathematical tools introduced in Chapter 2 will be applied to models that will be used in the next chapter (spin-independent and spin-dependent versions). The main focus will be on the calculation of the retarded Green's function, a crucial element for transport analysis.

### 3.1 Model Hamiltonian for Two-Terminals Transport

Let's remember (from Ch.2.4.1) the Hamiltonian system splits into three parts as follows:

$$H = H_c + H_{cen} + H_T. \quad (3.1)$$

Both the NEGF and the Hamiltonian setups of the following models will be mainly based on Eq.(3.1). Since we are interested in the scattering section (i.e., the central region), we define the Green Function based on the basis for  $H_{cen}$  which is assumed to be  $d_{n\sigma}(d_{m\sigma'}^\dagger)$ , thus:

$$G_{nm,\sigma\sigma'}(t, t') = (-i)\langle T\{d_{n\sigma}(t)d_{m\sigma'}^\dagger(t')\}\rangle. \quad (3.2)$$

Finally, the NEGF method for non-interacting central region leads to the Eq.(2.28) which is computed explicitly by using the following matrix form given by [31] for coherent transport:

$$\mathbf{G}^r(E) = \left[ E I - \hat{H}_{cen} - \Sigma^r(E) \right]^{-1}, \quad (3.3)$$

where:  $\Sigma^r = \Sigma_L^r + \Sigma_R^r$ . The explicit expression for  $\Sigma_{L(R)}^r(E)$  depends on the approximation

employed, however one important feature is that  $-2 \text{Im}(\Sigma_{L(R)}^r(E)) = \Gamma_{L(R)}(E)$ , where  $\Gamma_{L(R)}(E)$  is the level width function. The level width function  $\Gamma_{L(R)}(E)$  is related to the lifetime of the electronic density of states of the contacts within the scattering region. This is because electrons from the contacts do not remain in the central region indefinitely; they eventually leak away into the contacts [47].

### 3.2 Linear double-dot model

The linear double-dot model describes the electron flow between two metallic contacts connected to a central region, which consists of two discrete energy level structures linked by a hopping parameter  $V$ , sometimes denoted by  $t$  or  $\omega$ , i.e. a dimer, in a horizontal orientation. Fig.3.1 illustrates the commonly employed schematic representation for analyzing electron transport in horizontal molecular junction configurations [36, 37]. In this model, both contacts contain free electrons. These electrons tunnel from the contact with excess electrons to the dimer where after undergoing scattering processes between sites 1 and 2, the resulting electrons then tunnel to the contact with electron deficit. For example, in Fig.3.1 it is assumed that the left contact has the excess of electrons while the right contact has the deficit. As a result, the electrons flow from left to right.

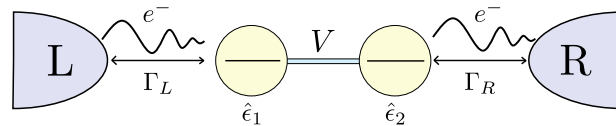


Figure 3.1: The schematic representation for spin-dependent electron transport in a horizontal junction. Here L(R) refers to the left(right) contact from which free electrons tunnel in and out to the molecules, while  $\Gamma_{L(R)}$  is the level width function that quantifies the tunneling from the contacts to the molecular junction, while the hopping  $V$  quantifies the contribution of the mixed spatial states 1 and 2.

The Hamiltonian for the model can be written as:

$$H^H = H_c + H_{cen} + H_T, \quad (3.4)$$

with

$$\begin{aligned}
H_c &= \sum_{k, \alpha \in \{L, R\}} \epsilon_{k\alpha\sigma} c_{k\alpha\sigma}^\dagger c_{k\alpha\sigma}, \\
H_{cen} &= \sum_{n, \sigma}^2 \epsilon_{n\sigma} d_{n\sigma}^\dagger d_{n\sigma} + (V d_{1\sigma}^\dagger d_{2\sigma} + h.c.), \\
H_T &= \sum_{k, \sigma} (V_{kL\sigma, 1\sigma} c_{kL, \sigma}^\dagger d_{1, \sigma} + V_{kR\sigma, 2\sigma} c_{kR\sigma}^\dagger d_{2, \sigma} + h.c.),
\end{aligned} \tag{3.5}$$

where  $\sigma = \{\uparrow, \downarrow\}$  is the spin label.  $H_{cen}$  has thus the following matrix representation in the basis of the localized states  $|n, \sigma\rangle$ :

$$\hat{H}_{cen} = \begin{pmatrix} \epsilon_{1\uparrow} & 0 & V & 0 \\ 0 & \epsilon_{1\downarrow} & 0 & V \\ V & 0 & \epsilon_{2\uparrow} & 0 \\ 0 & V & 0 & \epsilon_{2\downarrow} \end{pmatrix}.$$

The NEGF technique leads to an explicit expression for  $\mathbf{G}^r(E)$  given by Eq.(3.3). In this study, we will adopt the simplest case for the level width function  $\mathbf{\Gamma}_{L(R)}(E)$ , assuming a constant density of states in the contacts over the energy interval around the chemical potential ( $\mu_{L(R)}$ ). This is known as the Wide Band Limit (WBL) approximation, which is extensively used in quantum transport analysis across various structures, not limited to molecular junctions [1, 4, 44]. Thus, the approximation for  $\mathbf{\Sigma}_\alpha^r(E)$  under the Wide Band Limit (WBL) assumption is given by:

$$\begin{aligned}
\mathbf{\Sigma}_L^r(E) &= -\frac{i}{2}\mathbf{\Gamma}_L \simeq -\frac{i}{2} \begin{pmatrix} \gamma_L^\uparrow & 0 & 0 & 0 \\ 0 & \gamma_L^\downarrow & 0 & 0 \\ 0 & 0 & 0 & 0 \\ 0 & 0 & 0 & 0 \end{pmatrix}, \\
\mathbf{\Sigma}_R^r(E) &= -\frac{i}{2}\mathbf{\Gamma}_R \simeq -\frac{i}{2} \begin{pmatrix} 0 & 0 & 0 & 0 \\ 0 & 0 & 0 & 0 \\ 0 & 0 & \gamma_R^\uparrow & 0 \\ 0 & 0 & 0 & \gamma_R^\downarrow \end{pmatrix},
\end{aligned} \tag{3.6}$$

as a result, we observe that the tunneling is now characterized by  $\mathbf{\Gamma}$  rather than  $\Sigma^r(E)$  (see Fig. 3.1). This implies that the effect of the contacts on the scattering process is now governed solely by the lifetime of the electronic density of states in the contacts within the scattering region.

Then, Eq.(3.3) gets the following explicit form:

$$\mathbf{G}^r(E) = \begin{pmatrix} E - \epsilon_{1\uparrow} + \frac{i}{2}\gamma_L^\uparrow & 0 & -V & 0 \\ 0 & E - \epsilon_{1\downarrow} + \frac{i}{2}\gamma_L^\downarrow & 0 & -V \\ -V & 0 & E - \epsilon_{2\uparrow} + \frac{i}{2}\gamma_R^\uparrow & 0 \\ 0 & -V & 0 & E - \epsilon_{2\downarrow} + \frac{i}{2}\gamma_R^\downarrow \end{pmatrix}^{-1}, \quad (3.7)$$

with:

$$\begin{aligned} \epsilon_{n\sigma} &\equiv \epsilon_n + \hat{\sigma}\Delta, \\ \gamma_\alpha^\sigma &\equiv \frac{\gamma_\alpha}{2} (1 + \hat{\sigma}p_\alpha), \end{aligned} \quad (3.8)$$

being the free spin dependent parameters. Let's note in Eq.(3.8) that:

- $\Delta$  is called the spin degeneration term due to the presence of a magnetic field in the central region. It is a free parameter that changes the spin splitting of the site energy  $\epsilon_n$ .
- $p_\alpha \in [-1, 1]$  is called the polarization term, and it describes the magnetic behavior of the contact  $\alpha = \{L, R\}$ . It mimics the presence of a ferromagnetic contact.
- The effective Hamiltonian returns to its spin-independent state if  $\Delta = 0$  and  $p_\alpha = 0$ . If so, the NEGF Eq.(3.7) becomes:

$$\mathbf{G}^r(E) = \begin{pmatrix} E - \epsilon_1 + \frac{i}{2}\gamma_L & -V \\ -V & E - \epsilon_2 + \frac{i}{2}\gamma_R \end{pmatrix}^{-1}, \quad (3.9)$$

Some points about Eq.(3.9) include that it has free parameters like the site energies  $\epsilon_n$ , the hopping term  $V$ , and the widths  $\gamma_L, \gamma_R$ . Also, Eq.(3.9) needs numerical calculations to fully analyze the charge (spin) transmission and the thermopower effect. Therefore, the widths will be set to a single value ( $\gamma_L = \gamma_R = \gamma$ ) to reduce the number of free parameters.

### 3.3 T-shape model

The T-shape model describes the electron flow mediated by two linked (by the hopping  $V$ ) discrete energy levels, the same as in the linear double dot model, but in a vertical configuration. In this way, we include quantum interference effects, which are absent in the double-dot model presented in the previous section. Fig.3.2 shows the common schematic representation that is used to model the electron transport in molecular junctions [3, 36] and double quantum dots [4, 44]. The main transport channel is given by the L-site 1-R pathway (or vice versa), while site 2 is not directly involved in the transport process as it has no connection to the electronic baths.

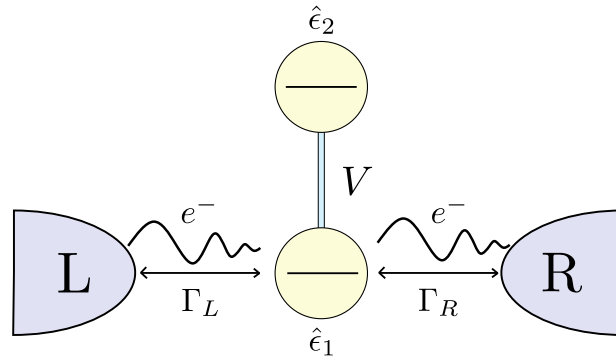


Figure 3.2: Schematic representation for the spin-dependent electron transport in a vertical junction. Here  $\Gamma_{L(R)}$  is the tunneling rate from the left to right contact while the hopping  $V$  quantifies the contribution of the mixed spatial states 1 and 2.

Let's make an analogous of the entire process from Ch.3.2 for solving this system. The Hamiltonian  $H^T$  is:

$$H^T = H_c + H_{cen} + H_T, \quad (3.10)$$

where the spin dependent expressions for the effective Hamiltonians of each zone are:

$$\begin{aligned} H_c &= \sum_{k, \alpha \in \{L, R\}} \epsilon_{k\alpha\sigma} c_{k\alpha\sigma}^\dagger c_{k\alpha\sigma}, \\ H_{cen} &= \sum_{n, \sigma}^2 \epsilon_{n\sigma} d_{n\sigma}^\dagger d_{n\sigma} + (V d_{1\sigma}^\dagger d_{2\sigma} + h.c.), \\ H_T &= \sum_{k, \alpha \in \{L, R\}} V_{k\alpha\sigma, 1\sigma} c_{k\alpha\sigma}^\dagger d_{1\sigma} + h.c. \end{aligned} \quad (3.11)$$

The corresponding matrix form of the Hamiltonian of the central region is given by:

$$\hat{H}_{cen} = \begin{pmatrix} \epsilon_{1\uparrow} & 0 & V & 0 \\ 0 & \epsilon_{1\downarrow} & 0 & V \\ V & 0 & \epsilon_{2\uparrow} & 0 \\ 0 & V & 0 & \epsilon_{2\downarrow} \end{pmatrix}.$$

Using the previously introduced Wide Band Limit (WBL) in the retarded self-energies leads to:

$$\Sigma_{\alpha}^r(E) = -\frac{i}{2}\Gamma_{\alpha} \simeq -\frac{i}{2} \begin{pmatrix} \gamma_{\alpha}^{\uparrow} & 0 & 0 & 0 \\ 0 & \gamma_{\alpha}^{\downarrow} & 0 & 0 \\ 0 & 0 & 0 & 0 \\ 0 & 0 & 0 & 0 \end{pmatrix}, \quad (3.12)$$

for the  $\alpha = \{L, R\}$  contacts. From which we notice the level-width function  $\Gamma_R$  definition in Eq.(3.12) is different from the same one but of the linear double-dot model (3.6) as the site 1 is connected to both contacts. Finally, Eq.(3.3) gets the explicit form:

$$\mathbf{G}^r(E) = \begin{pmatrix} E - \epsilon_{1\uparrow} + \frac{i}{2}\gamma_T^{\uparrow} & 0 & -V & 0 \\ 0 & E - \epsilon_{1\downarrow} + \frac{i}{2}\gamma_T^{\downarrow} & 0 & -V \\ -V & 0 & E - \epsilon_{2\uparrow} & 0 \\ 0 & -V & 0 & E - \epsilon_{2\downarrow} \end{pmatrix}^{-1}, \quad (3.13)$$

with  $\gamma_T^{\sigma} = \gamma_L^{\sigma} + \gamma_R^{\sigma}$  being the main difference with respect to the Eq.(3.7). This is because the position in the matrix (3.13) for the right width  $\gamma_R$  is different from the matrix (3.7) of the linear double-dot model presented in the previous section.

The free spin-dependent parameters are controlled by the same terms as the Ch.3.2 (i.e.  $\Delta$  and  $p_{\alpha}$ ). So, the spin-independent case of (3.13) is:

$$\mathbf{G}^r(E) = \begin{pmatrix} E - \epsilon_1 + \frac{i}{2}\gamma_T & -V \\ -V & E - \epsilon_2 \end{pmatrix}^{-1}. \quad (3.14)$$

### 3.4 T-shape dimer model

The T-shape dimer model consists of a combination of the previous models. Fig.3.3 describes the electron flow between two terminals (contacts) mediated by a central region whose configuration ensembles 4 discrete energy level structures, also called sites, which are organized into two linked vertical configurations, like the T-shape model but each one connected by a hopping  $\omega$ , that are horizontally connected only through one of the two sites by hopping  $V$ , like the linear double dot model. This scheme is useful to figure and model the electron transport in systems such as the array of laterally coupled quantum dots [9] which is the generalized case for N vertical configurations horizontally connected.

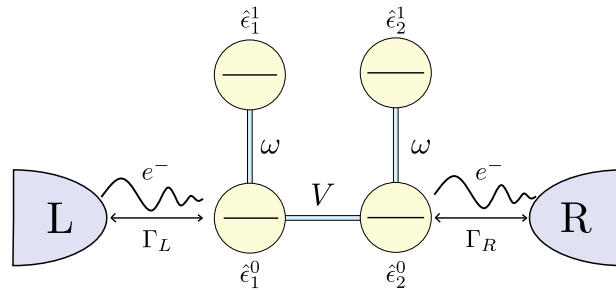


Figure 3.3: Schematic representation for the spin-dependent transport for an array of two laterally coupled double quantum dots (DQDs). Here  $\omega$  quantifies the mixed states contribution for the sites  $\{(0, 1), (1, 1)\}$  and  $\{(0, 2), (1, 2)\}$  while  $V$  quantifies the mixed states contribution for the sites  $\{(0, 1), (0, 2)\}$ . The generalization of this model for N laterally coupled DQDs is used for studies in thermal spin filters [9].

The Hamiltonian for this model is:

$$\begin{aligned}
 H_c &= \sum_{k, \alpha \in \{L, R\}} \epsilon_{k\alpha\sigma} c_{k\alpha\sigma}^\dagger c_{k\alpha\sigma}, \\
 H_{cen} &= \sum_{n, \sigma}^2 \left( \epsilon_{n\sigma}^0 b_{n\sigma}^\dagger b_{n\sigma} + \epsilon_{n\sigma}^1 a_{n\sigma}^\dagger a_{n\sigma} \right) + \sum_{n, \sigma}^2 \left( \omega b_{n\sigma}^\dagger a_{n\sigma} + h.c. \right) + \left( V b_{1\sigma}^\dagger b_{2\sigma} + h.c. \right), \quad (3.15) \\
 H_T &= \sum_{k, \sigma} \left( V_{kL\sigma, 1\sigma} c_{kL\sigma}^\dagger b_{1\sigma} + V_{kR\sigma, 2\sigma} c_{kR\sigma}^\dagger b_{2\sigma} + h.c. \right),
 \end{aligned}$$

notice that the non-interacting central region  $H_{cen}$  contains two creation/annihilation operators  $\{b_{n\sigma}^\dagger, a_{n\sigma}^\dagger\}/\{b_{n\sigma}, a_{n\sigma}\}$ . Since the side sites (i.e.  $\{(1, 1), (1, 2)\}$ ) are non-interacting, we can rewrite the  $H_{cen}$  and thus the overall Hamiltonian in terms of a new creation/annihilation operator  $d_{n\sigma}^\dagger$  that considers the effective contributions of the side sites energies  $\epsilon_n^1$  over the connected sites  $\epsilon_n^0$ .

We can derive such an effective contribution in a rigorous way by considering the total Green's function and during the equation of motion technique implementation, design the functions related to the sites (1, 1) and (1, 2) as contributions for the Green's function of the sites (0, 1) and (0, 2).

Alternatively, we can work faster over the matrix form by renormalizing the elements of the overall  $\hat{H}_{cen}$ . To obtain that, we will focus only in the terms (assuming no spin dependence) that relates  $b_n^\dagger/b_n$  with  $a_n^\dagger/a_n$  from  $H_{cen}$ :

$$H_s = \sum_n^2 (\epsilon_n^0 b_n^\dagger b_n + \epsilon_n^1 a_n^\dagger a_n) + \sum_n^2 (\omega b_n^\dagger a_n + h.c.),$$

now, we use the Schrödinger equation for this case, to get:

$$\begin{aligned} H_s \psi &= E \psi \\ \Rightarrow \begin{pmatrix} \epsilon_n^0 & \omega \\ \omega & \epsilon_n^1 \end{pmatrix} \begin{pmatrix} b_n \\ a_n \end{pmatrix} &= E \begin{pmatrix} b_n \\ a_n \end{pmatrix}, \end{aligned}$$

that is a set of linear algebraic equations which we can solve for  $b_n$  and obtain:

$$\left( \epsilon_n^0 + \frac{\omega^2}{E - \epsilon_n^1} \right) b_n = E b_n,$$

from which we can redefine in terms of the new operator  $d_n$ :

$$\Rightarrow \left( \epsilon_n^0 + \frac{\omega^2}{E - \epsilon_n^1} \right) d_n = \epsilon_n d_n,$$

and then only includes the spin label:

$$\epsilon_{n\sigma} \equiv \epsilon_{n\sigma}^0 + \frac{\omega^2}{E - \epsilon_{n\sigma}^1},$$

in this way we assert that Hamiltonian dimension can be reduced by considering effective energy sites.

Now, we rewrite the Hamiltonian (3.15) to get:

$$\begin{aligned}
H_c &= \sum_{k, \alpha \in \{L, R\}} \varepsilon_{k\alpha\sigma} c_{k\alpha\sigma}^\dagger c_{k\alpha\sigma}, \\
H_{cen} &= \sum_{n, \sigma}^2 \varepsilon_{n\sigma} d_{n\sigma}^\dagger d_{n\sigma} + (V d_{1\sigma}^\dagger d_{2\sigma} + h.c.), \\
H_T &= \sum_{k, \sigma} (V_{kL\sigma, 1\sigma} c_{kL, \sigma}^\dagger d_{1\sigma} + V_{kR\sigma, 2\sigma} c_{kR\sigma}^\dagger d_{2\sigma} + h.c.),
\end{aligned} \tag{3.16}$$

where:

$$\varepsilon_{n\sigma} \equiv \epsilon_{n\sigma}^0 + \frac{\omega^2}{E - \epsilon_{n\sigma}^1},$$

noticing that the GF is the Eq.(3.2) and  $H_{cen}$  is allowed to be in matrix representation:

$$\hat{H}_{cen} = \begin{pmatrix} \varepsilon_{1\uparrow} & 0 & V & 0 \\ 0 & \varepsilon_{1\downarrow} & 0 & V \\ V & 0 & \varepsilon_{2\uparrow} & 0 \\ 0 & V & 0 & \varepsilon_{2\downarrow} \end{pmatrix},$$

then the NEGF technique leads to the explicit expression for  $\mathbf{G}^r(E)$  Eq.(3.3), where  $\mathbf{\Sigma}^r = \mathbf{\Sigma}_L^r + \mathbf{\Sigma}_R^r$  and  $\mathbf{\Sigma}_\alpha^r(E)$  is given by the WBL:

$$\begin{aligned}
\mathbf{\Sigma}_L^r(E) &= -\frac{i}{2}\mathbf{\Gamma}_L \simeq -\frac{i}{2} \begin{pmatrix} \gamma_L^\uparrow & 0 & 0 & 0 \\ 0 & \gamma_L^\downarrow & 0 & 0 \\ 0 & 0 & 0 & 0 \\ 0 & 0 & 0 & 0 \end{pmatrix}, \\
\mathbf{\Sigma}_R^r(E) &= -\frac{i}{2}\mathbf{\Gamma}_R \simeq -\frac{i}{2} \begin{pmatrix} 0 & 0 & 0 & 0 \\ 0 & 0 & 0 & 0 \\ 0 & 0 & \gamma_R^\uparrow & 0 \\ 0 & 0 & 0 & \gamma_R^\downarrow \end{pmatrix}.
\end{aligned}$$

Then, Eq.(3.3) gets the following explicit form:

$$\mathbf{G}^r(E) = \begin{pmatrix} E - \varepsilon_{1\uparrow} + \frac{i}{2}\gamma_L^\uparrow & 0 & -V & 0 \\ 0 & E - \varepsilon_{1\downarrow} + \frac{i}{2}\gamma_L^\downarrow & 0 & -V \\ -V & 0 & E - \varepsilon_{2\uparrow} + \frac{i}{2}\gamma_R^\uparrow & 0 \\ 0 & -V & 0 & E - \varepsilon_{2\downarrow} + \frac{i}{2}\gamma_R^\downarrow \end{pmatrix}^{-1}, \quad (3.17)$$

where the free spin-dependent parameters are:

$$\begin{aligned} \epsilon_{n\sigma}^i &\equiv \epsilon_n^i + \hat{\sigma}\Delta, \\ \gamma_\alpha^\sigma &\equiv \frac{\gamma_\alpha}{2} (1 + \hat{\sigma}p_\alpha). \end{aligned} \quad (3.18)$$

As a result, Eq.(3.17) combines the previous two models, with Eq.(3.7) providing the matrix structure, while  $\varepsilon_{n\sigma} \equiv \epsilon_{n\sigma}^0 + \frac{\omega^2}{E - \epsilon_{n\sigma}^1}$  accounts for the contributions from Eq.(3.13).

The free spin dependent parameters are controlled by the same terms as the Ch.3.2 (i.e.  $\Delta$  and  $p_\alpha$ ). Then, the spin independent version of Eq.(3.17) is:

$$\mathbf{G}^r(E) = \begin{pmatrix} E - \varepsilon_1 + \frac{i}{2}\gamma_L & -V \\ -V & E - \varepsilon_2 + \frac{i}{2}\gamma_R \end{pmatrix}^{-1}. \quad (3.19)$$

### 3.5 Michaeli-Geyer Model

The CISS effect has been demonstrated in organic systems characterized by helical symmetry, enabling spin filtering without needing an applied magnetic field. Consequently, the primary approach to analyze spin electron transport involves considering three-dimensional systems. However, for numerical purposes, a one-dimensional model that captures the essential features of spin electron transport in helical structures is desirable, as it reduces computational complexity. In this context, Michaeli and Naaman [49] reduced the problem to an effective one-dimensional problem and then Geyer et al. systematized such a model to analyze the CISS effects [10]. As a result, the Michaeli-Geyer model was designed to analyze the CISS effect by utilizing a curved path in 3D space, thereby reducing the problem to a one-dimensional analysis. Fig.3.4 depicts the central region under a continuous Hamiltonian in a 3D space. In this adapted model, electrons from the left contact tunnel

to the bottom of the system, traverse the curved path through the helix, and finally tunnel to the right contact.

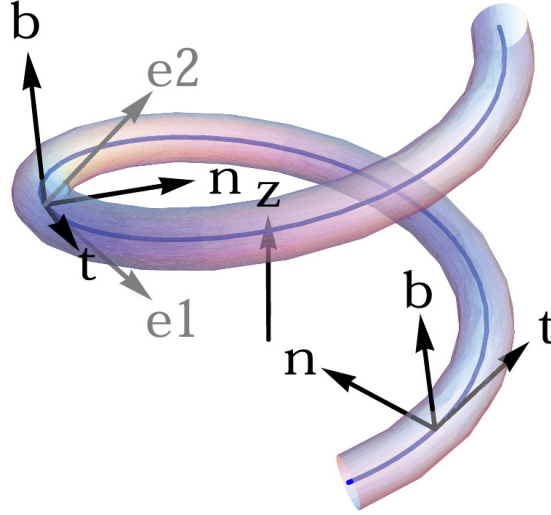


Figure 3.4: Schematic representation of the Helical Cylinder system. Here  $\{\mathbf{t}, \mathbf{e}_1, \mathbf{e}_2\}$  refers to the rotated frame and  $\{\mathbf{t}, \mathbf{n}, \mathbf{b}\}$  refers to the Frenet frame, both basis vectors to parametrize the curve and global z-axis. Extracted from Ref.[10]

The model is characterized by a central region Hamiltonian formulated in terms of the Frenet frame which refers to the set of unitary vectors designed to parametrize the curve (helix) in 3D (see Fig. 3.4). By constraining the electron motion to a curved trajectory, we can reduce the spatial degrees of freedom and employ an effective one-dimensional Hamiltonian. This approach leverages the quantized version of the classical Hamilton function for a particle confined to a curve. Ultimately, the effective Hamiltonian utilized in this study is derived from the tight-binding discretization of the one-dimensional Hamiltonian where it is assumed sites in a spiral path with their respective hybridization term between neighbor sites and strong spin-orbit coupling (SOC) term due to a generic scalar potential (not necessarily an electromagnetic) constructed upon the Frenet frame coordinates [10].

So, the effective Hamiltonian  $H^{hel}$  used is based upon the second quantization model presented by Ref.[10] that is:

$$H^{hel} = H_c + H_{cen} + H_T, \quad (3.20)$$

where the explicit spin-dependent terms, for  $N = 2$ , are:

$$\begin{aligned}
H_c &= \sum_{k, \alpha \in \{L, R\}} \epsilon_{k\alpha\sigma} c_{k\alpha\sigma}^\dagger c_{k\alpha\sigma}, \\
H_{cen} &= \sum_{n, \sigma} \epsilon_{n\sigma} d_{n\sigma}^\dagger d_{n\sigma} + \sum_{n, \sigma}^{N-1} \left( d_{n+1\sigma}^\dagger \hat{V} d_{n\sigma} + h.c. \right) + \lambda_2 L \sum_{n, \sigma, \sigma'}^N d_{n\sigma}^\dagger (\boldsymbol{\sigma} \cdot \mathbf{B})_{\sigma\sigma'} d_{n\sigma'}, \quad (3.21) \\
H_T &= \sum_{k, \sigma} \left( V_{kL\sigma, 1\sigma} c_{kL, \sigma}^\dagger d_{1\sigma} + V_{kR\sigma, 2\sigma} c_{kR, \sigma}^\dagger d_{2\sigma} + h.c. \right),
\end{aligned}$$

with:  $\hat{V} \equiv -t\delta_{\sigma\sigma'} - i\lambda_1 (\boldsymbol{\sigma} \cdot \mathbf{A})_{\sigma\sigma'}$ , where  $\mathbf{B}$  plays the role of an effective magnetic field and  $\boldsymbol{\sigma} \cdot \mathbf{A}$  plays the role of a geometric Gauge potential. The GF is defined as the Eq.(3.2):

$$G_{nm, \sigma\sigma'}(t, t') = (-i) \langle T \{ d_{n\sigma}(t), d_{m\sigma'}^\dagger(t') \} \rangle,$$

given that  $H_{cen}$  can exhibit a discrete spectrum and assuming that  $\mathbf{A} = (0, 0, 0)$  and  $\mathbf{B} = (0, B, B)$ , the matrix representation of  $H_{cen}$  is as follows:

$$\hat{H}_{cen} = \begin{pmatrix} \epsilon_{1\uparrow} + \lambda_2 LB & -i\lambda_2 LB & -t & 0 \\ i\lambda_2 LB & \epsilon_{1\downarrow} - \lambda_2 LB & 0 & -t \\ -t & 0 & \epsilon_{2\uparrow} + \lambda_2 LB & -i\lambda_2 LB \\ 0 & -t & i\lambda_2 LB & \epsilon_{2\downarrow} - \lambda_2 LB \end{pmatrix}, \quad (3.22)$$

so, the NEGF technique leads to the explicit expression for  $\mathbf{G}^r(E)$  i.e. Eq.(3.3):

$$G^r = [EI - \hat{H}_{cen} - \boldsymbol{\Sigma}^r(E)]^{-1},$$

where  $\boldsymbol{\Sigma}^r = \boldsymbol{\Sigma}_L^r + \boldsymbol{\Sigma}_R^r$  and  $\boldsymbol{\Sigma}_\alpha^r(E)$  is given by the WBL:

$$\boldsymbol{\Sigma}_L^r(E) = -\frac{i}{2} \boldsymbol{\Gamma}_L \simeq -\frac{i}{2} \begin{pmatrix} \gamma_L^\uparrow & 0 & 0 & 0 \\ 0 & \gamma_L^\downarrow & 0 & 0 \\ 0 & 0 & 0 & 0 \\ 0 & 0 & 0 & 0 \end{pmatrix},$$

$$\Sigma_R^r(E) = -\frac{i}{2}\Gamma_R \simeq -\frac{i}{2} \begin{pmatrix} 0 & 0 & 0 & 0 \\ 0 & 0 & 0 & 0 \\ 0 & 0 & \gamma_R^\uparrow & 0 \\ 0 & 0 & 0 & \gamma_R^\downarrow \end{pmatrix}.$$

Then, Eq.(3.3) takes the following explicit form:

$$\mathbf{G}^r(E) = \begin{pmatrix} E - \epsilon_{1\uparrow} - \lambda_2 LB + \frac{i}{2}\gamma_L^\uparrow & i\lambda_2 LB & t & 0 \\ -i\lambda_2 LB & E - \epsilon_{1\downarrow} + \lambda_2 LB + \frac{i}{2}\gamma_L^\uparrow & 0 & t \\ t & 0 & E - \epsilon_{2\uparrow} - \lambda_2 LB + \frac{i}{2}\gamma_R^\uparrow & i\lambda_2 LB \\ 0 & t & -i\lambda_2 LB & E - \epsilon_{2\downarrow} + \lambda_2 LB + \frac{i}{2}\gamma_R^\uparrow \end{pmatrix}^{-1}. \quad (3.23)$$

### 3.6 Extended Michaeli-Geyer Model

The extended Michaeli-Geyer model takes the entire model proposed by Ref.[10] but attaching side dots to the central tight-binding chain to now include quantum interference (QI) effects during the electron transport. In this regard, the only change is due to the onsite energies, which must be renormalized.

After renormalization process, the effective Hamiltonian for such a model  $H_{s-d}^{hel}$  is:

$$H_{s-d}^{hel} = H_c + H_{cen} + H_T, \quad (3.24)$$

where the explicit spin-dependent terms are:

$$\begin{aligned} H_c &= \sum_{k, \alpha \in \{L, R\}} \varepsilon_{k\alpha\sigma} c_{k\alpha\sigma}^\dagger c_{k\alpha\sigma}, \\ H_{cen} &= \sum_{n, \sigma} \varepsilon_{n\sigma} d_{n\sigma}^\dagger d_{n\sigma} + \sum_{n, \sigma}^{N-1} (d_{n+1\sigma}^\dagger \hat{V} d_{n\sigma} + h.c.) + \lambda_2 L \sum_{n, \sigma, \sigma'}^N d_{n\sigma}^\dagger (\boldsymbol{\sigma} \cdot \mathbf{B})_{\sigma\sigma'} d_{n\sigma'}, \\ H_T &= \sum_{k, \sigma} (V_{kL\sigma, 1\sigma} c_{kL, \sigma}^\dagger d_{1\sigma} + V_{kR\sigma, 2\sigma} c_{kR\sigma}^\dagger d_{2\sigma} + h.c.), \end{aligned} \quad (3.25)$$

with:  $\hat{V} \equiv -t\delta_{\sigma\sigma'} - i\lambda_1 (\boldsymbol{\sigma} \cdot \mathbf{A})_{\sigma\sigma'}$  and  $\varepsilon_{n\sigma} \equiv \epsilon_{n\sigma}^0 + \frac{\omega^2}{E - \epsilon_{n\sigma}^0}$ . The GF is defined as the Eq.(3.2):

$$G_{nm, \sigma\sigma'}(t, t') = (-i)\langle T\{d_{n\sigma}(t), d_{m\sigma'}^\dagger\} \rangle,$$

the next steps about definitions for  $\hat{H}_{cen}$  and  $\mathbf{G}^r(E)$  are analogous.

In what follows, we will assume the null vector for  $\mathbf{A}$ ,  $\mathbf{A} = (0, 0, 0)$  while 0 for the x component and the same values for the y and z components of  $\mathbf{B}$ ,  $\mathbf{B} = (0, B, B)$ . So, the matrix representation of  $H_{cen}$  is as follows:

$$\hat{H}_{cen} = \begin{pmatrix} \varepsilon_{1\uparrow} + \lambda_2 LB & -i\lambda_2 LB & -t & 0 \\ i\lambda_2 LB & \varepsilon_{1\downarrow} - \lambda_2 LB & 0 & -t \\ -t & 0 & \varepsilon_{2\uparrow} + \lambda_2 LB & -i\lambda_2 LB \\ 0 & -t & i\lambda_2 LB & \varepsilon_{2\downarrow} - \lambda_2 LB \end{pmatrix}, \quad (3.26)$$

the NEGF technique leads to the explicit expression for  $\mathbf{G}^r(E)$ :

$$G^r = [EI - \hat{H}_{cen} - \Sigma^r(E)]^{-1},$$

where  $\Sigma^r = \Sigma_L^r + \Sigma_R^r$  and  $\Sigma_a^r(E)$  is given by the WBL. It follows the same matrix elements from the retarded self energy matrices in Ch. 3.5.

Then, Eq.(3.3) takes the following explicit form:

$$\mathbf{G}^r(E) = \begin{pmatrix} E - \varepsilon_{1\uparrow} - \lambda_2 LB + \frac{i}{2}\gamma_L^\uparrow & i\lambda_2 LB & t & 0 \\ -i\lambda_2 LB & E - \varepsilon_{1\downarrow} + \lambda_2 LB + \frac{i}{2}\gamma_L^\uparrow & 0 & t \\ t & 0 & E - \varepsilon_{2\uparrow} - \lambda_2 LB + \frac{i}{2}\gamma_R^\uparrow & i\lambda_2 LB \\ 0 & t & -i\lambda_2 LB & E - \varepsilon_{2\downarrow} + \lambda_2 LB + \frac{i}{2}\gamma_R^\uparrow \end{pmatrix}^{-1}, \quad (3.27)$$

which is identical to Eq.(3.23) but with  $\varepsilon_{n\sigma} \equiv \epsilon_{n\sigma}^0 + \frac{\omega^2}{E - \epsilon_{n\sigma}^1}$  instead of  $\epsilon_{n\sigma}$ .

# Chapter 4

## Results and Discussion

In this chapter, we will discuss (spin-dependent) quantum transport using the effective models introduced in the previous chapter. Our focus will be on thermopower and the effects of quantum interference on it. In the final part of the chapter, the modified Michaeli-Geyer model, which includes spin-orbit interaction, will also be investigated.

### 4.1 Linear double-dot model: Landauer Transmission

We start our discussion with the transmission function of this model, which does not display any quantum interference (QI) effects and which will serve as a reference point when introducing QI. Firstly, we want to see the effect of the hopping term  $V$  and the onsite energy  $\{\epsilon_1, \epsilon_2\}$  and with  $\Delta = 0$  when the charge carrier flow is spin-independent ( $p_L = p_R = 0$ ) for a given spectral broadening  $\gamma$ . The corresponding Landauer transmission is shown in Fig. 4.1.

We notice in Fig.4.1a) that the numerical value at the transmission peaks is 2, which corresponds to the maximum allowed value for transmission instead of the usual 1. This occurs because the transport is divided into two channels, one for each spin. Since the maximum value per spin channel is 1, the total transmission, which is the contribution of both channels, is 2. These transmission peaks ( $T_{max} = 2$ ) remain constant as we vary  $V$  because the site energies are equal ( $\epsilon_1 = \epsilon_2$ ). The peaks are located at two energies that get closer if  $|V| \rightarrow |\gamma|$  and keep away if  $|V| > |\gamma|$ . In contrast, in Fig.4.1b), we see a similar relationship between the peak energies and the parameters  $|V|$  and  $|\gamma|$  as in a), indicating that the distance between peaks is generally controlled by  $|V|$  regardless of whether the

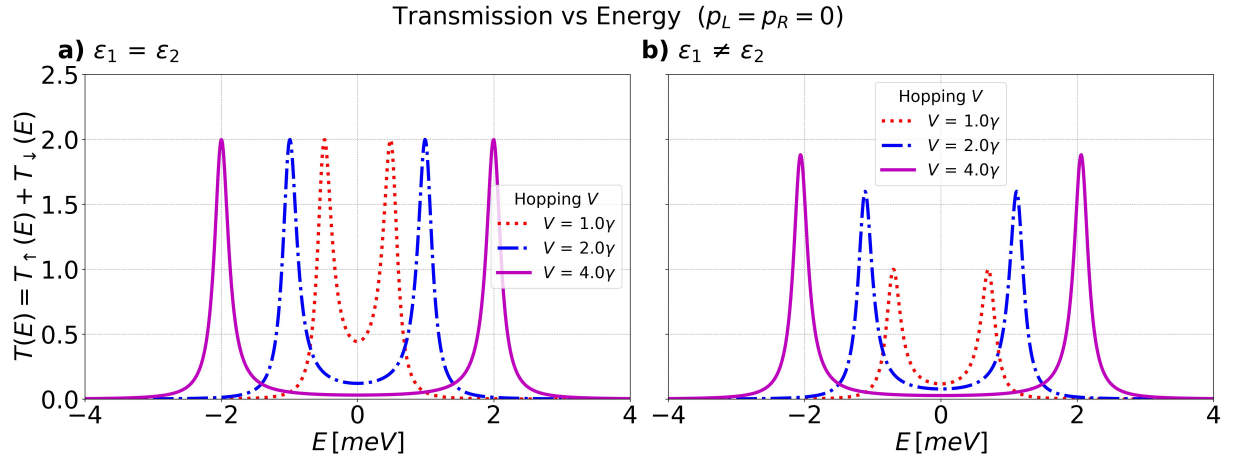


Figure 4.1: Landauer Transmission for the linear double dot model; when  $\Delta = 0 \text{ meV}$ ,  $\gamma = 0.5 \text{ meV}$  and  $p_\alpha = 0$ ; for different values of the hopping term  $V$  in an energy interval of  $[-4, 4] \text{ meV}$ , with a) The same site energies,  $\epsilon_1 = \epsilon_2 = 0 \text{ meV}$ . b) Different site energies,  $\epsilon_1 = -0.5 \text{ meV}$  and  $\epsilon_2 = 0.5 \text{ meV}$ . The peaks from both figures are called resonances and represent the energy where the Transmission is the maximum (i.e.  $T_{max}$ ).

site energies are equal or not. However, unlike in Fig.4.1a), the transmission peaks are no longer constant as  $V$  varies because the site energies are now different ( $\epsilon_1 \neq \epsilon_2$ ). The peak values decrease ( $T_{max} \rightarrow 0$ ) as  $|V| \rightarrow |\gamma|$ , while they approach to the maximum value allowed ( $T_{max} \rightarrow 2$ ) if  $|V| \gg |\gamma|$ .

We can explain analytically the behavior of the peak value for different values of  $V$  by considering the explicit total Landauer transmission derived from Eq.(3.7) when  $\Delta = 0$  and  $p_\alpha = 0$ :

$$T(E) = 2 \frac{\left(\frac{\gamma^2}{4}\right) V^2}{\left[(E - \epsilon_1)(E - \epsilon_2) - \left(\frac{\gamma}{4}\right)^2 - V^2\right]^2 + \left(\frac{\gamma}{4}\right)^2 (2E - \epsilon_1 - \epsilon_2)^2}. \quad (4.1)$$

Firstly, if we consider  $\epsilon_1 = \epsilon_2 \equiv \epsilon$ :

$$T(E) = 2 \frac{\left(\frac{\gamma^2}{4}\right) V^2}{\left[(E - \epsilon)^2 - \left(\frac{\gamma}{4}\right)^2 - V^2\right]^2 + \frac{\gamma^2}{4} (E - \epsilon)^2},$$

we can obtain a value near to  $T_{max}$  if:

$$(E - \epsilon)^2 - \left(\frac{\gamma}{4}\right)^2 - V^2 = 0,$$

$$\Rightarrow E_{\pm} = \epsilon \pm \sqrt{\left(\frac{\gamma}{4}\right)^2 + V^2}, \quad (4.2)$$

then, evaluating  $E_{\pm}$  over  $T(E)$ :

$$\begin{aligned} \Rightarrow T(E_{\pm}) &= \frac{2V^2}{(E_{\pm} - \epsilon)^2}, \\ &= 2 \frac{V^2}{\left(\frac{\gamma}{4}\right)^2 + V^2}, \end{aligned}$$

which, after dividing by the broadening  $\gamma$ , results in:

$$\Rightarrow T(E_{\pm}) = 2 \frac{\left(\frac{V}{\gamma}\right)^2}{\frac{1}{16} + \left(\frac{V}{\gamma}\right)^2}. \quad (4.3)$$

From Eq.(4.3), we obtain  $T(E_{\pm}) \approx 1.9$  if we evaluate  $\left|\frac{V}{\gamma}\right| \rightarrow 1$  for any  $\epsilon$  and  $T(E_{\pm}) \approx 2 \equiv T_{max}$  if we evaluate  $\left|\frac{V}{\gamma}\right| \gg 1$  for any  $\epsilon$ .

On the other hand, we make an analogous process for  $\epsilon_1 \neq \epsilon_2$  and we obtain:

$$E_{\pm} = \frac{(\epsilon_1 + \epsilon_2)}{2} \pm \frac{1}{2} \sqrt{(\epsilon_1 - \epsilon_2)^2 + 4 \left(\frac{\gamma}{4}\right)^2 + 4V^2},$$

from which we get, after evaluating in  $T(E)$  and dividing by  $\gamma$ :

$$T(E_{\pm}) = 8 \frac{\left(\frac{V}{\gamma}\right)^2}{\frac{1}{4} + 4 \left(\frac{V}{\gamma}\right)^2 + \left(\frac{\epsilon_1 - \epsilon_2}{\gamma}\right)^2},$$

we highlight the behavior of  $T(E_{\pm})$  if  $\left|\frac{V}{\gamma}\right| \rightarrow 1$ :

$$T(E_{\pm}) = \frac{8}{\frac{1}{4} + 4 + \frac{(\epsilon_1 - \epsilon_2)^2}{V^2}}, \quad (4.4)$$

which is dependent of  $V$  as follows:  $T(E_{\pm}) \approx 0$  if  $|V| < |\epsilon_1 - \epsilon_2|$  and  $T(E_{\pm}) \approx 2 \equiv T_{max}$  if  $|V| \gg |\epsilon_1 - \epsilon_2|$ . Additionally, we highlight the behavior of  $T(E_{\pm})$  if  $\left|\frac{V}{\gamma}\right| \gg 1$  (no matter the values for  $\epsilon_{1(2)}$ ) that is independent of  $V$ :

$$T(E_{\pm}) \approx \frac{8}{4} = 2 \equiv T_{max}, \quad (4.5)$$

and the behavior of  $T(E_{\pm})$  if  $\left|\frac{V}{\gamma}\right| \ll 1$  (no matter the values for  $\epsilon_{1(2)}$ ) that is also indepen-

dent of  $V$ :

$$T(E_{\pm}) \approx 0. \quad (4.6)$$

Therefore, from the behavior of Eqs. (4.3)-(4.6) concerning  $\left|\frac{V}{\gamma}\right|$  and  $\epsilon_{1(2)}$ , we conclude that the transmission peak values  $T(E_{\pm})$  depend on  $V$  only if  $\left|\frac{V}{\gamma}\right| \approx 1$  and  $\epsilon_1 \neq \epsilon_2$ , because we observe that  $0 < T(E_{\pm}) < T_{max}$ , according to Eq.(4.4). Meanwhile, we have that  $T(E_{\pm}) \approx 0$  for  $\left|\frac{V}{\gamma}\right| \ll 1$  (no matter the values for  $\epsilon_{1(2)}$ ), according to Eq.(4.6). Conversely, according to Eqs. (4.3) and (4.5), we see that  $T(E_{\pm}) = T_{max}$  will be constant for the remaining cases. Specially we notice that if  $\left|\frac{V}{\gamma}\right| \gg 1$  then  $T(E_{\pm}) = T_{max} = 2$  will be constant no matter whether site energies are the same ( $\epsilon_1 = \epsilon_2$ ) or not ( $\epsilon_1 \neq \epsilon_2$ ). If so, we can call  $T(E_{\pm}) = T_{max}$  as resonance and  $E_{\pm}$  as resonance energies.

We can physically understand the influence of  $\left|\frac{V}{\gamma}\right|$  on  $T_{max}$  if we use the semi-classical analogy of a damped-driven oscillator system. If so, the spectral broadening ( $\gamma$ ) can be related to friction (dissipation) into an environment (the metal contacts) [50]. Depending on the strength  $\gamma$  of the coupling to this environment, we will have three cases: underdamped, critically damped, or overdamped [50]. Thus, well-defined transmission resonances can only be found in the underdamped limit, corresponding to a weak/intermediate coupling to the electronic baths (i.e.  $|V| \gg |\gamma|$  and  $|V| > |\gamma|$  respectively). On the contrary, if the coupling with the environment  $\gamma$  is very large (i.e.  $|V| \ll |\gamma|$ ), then  $T_{max} \rightarrow 0$  because the concept of resonance is not anymore relevant, and the system interacting with the electrodes loses its "identity". We will, therefore, consider only the underdamped case  $|V| \gg |\gamma|$ . If so, we can drop the difference between energy sites and, from now on, consider by assumption only the case when they are the same, i.e.  $\epsilon_1 = \epsilon_2 = 0 \text{ meV}$  as our reference point because in the underdamped limit, the transmission profile will be quite similar no matter whether  $\epsilon_1 = \epsilon_2$  or  $\epsilon_1 \neq \epsilon_2$ .

### 4.1.1 Contact polarization influence

Next, let's analyze the effect of the electrode polarization on the transmission (both total and per spin channel). If we consider  $p_L$  and  $p_R$  to vary, we need to include the contact ( $L/R$ ) and spin ( $\sigma$ ) dependence in the transmission. So, when we assume the underdamped case  $\left|\frac{V}{\gamma}\right| \gg 1$  and  $\epsilon_1 = \epsilon_2 = 0 \text{ meV}$ , the transmission per spin channel  $T_{\sigma}(E)$  and total

transmission  $T(E) = T_{\uparrow}(E) + T_{\downarrow}(E)$  will have the shapes shown in Fig.4.2.

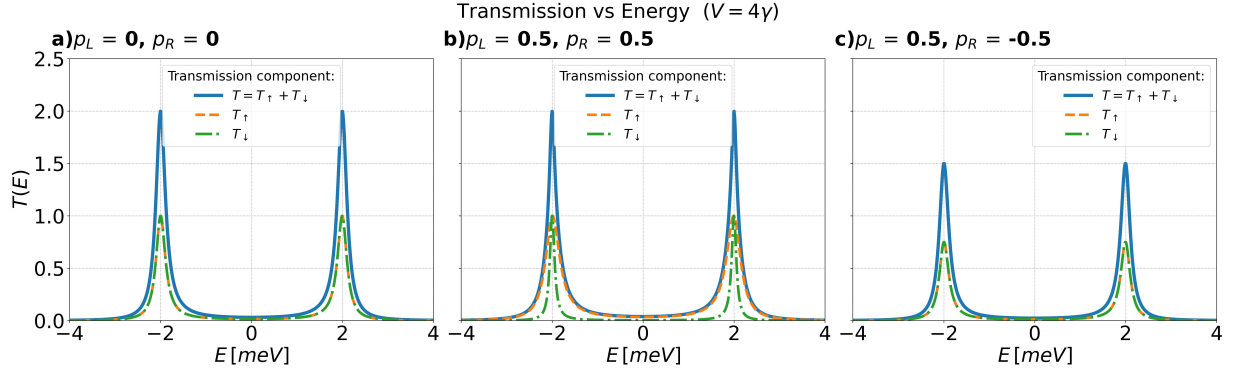


Figure 4.2: Landauer transmission for the double-dot model ( $\epsilon_1 = \epsilon_2 = 0 \text{ meV}$ ,  $\Delta = 0 \text{ meV}$ ,  $\gamma = 0.5 \text{ meV}$  and  $V = 4\gamma$ ) for different polarization values  $p_\alpha$ . The solid line represents the total transmission profile while the dashed/dash-dot is for the spin up/down transmission.

We notice that Fig.4.2a) shows  $T_{\uparrow}(E)$  has the same shape as  $T_{\downarrow}(E)$ , and  $T = T_{\uparrow} + T_{\downarrow}$  follows the same profile as Fig.4.1a) due to the zero polarization. In panel b), since the polarizations are the same ( $p_L = p_R = 0.5$ ),  $T = T_{\uparrow} + T_{\downarrow}$  has the same shape as panel a) despite  $T_{\uparrow}(E)$  is broader around the resonances in comparison to  $T_{\downarrow}(E)$ . Lastly, in panel c), we notice that the resonance values for  $T_\sigma(E)$  decrease, and thus for  $T(E)$  as well, because the polarizations now are opposite ( $p_L = 0.5$ ,  $p_R = -0.5$ ).

We can explain analytically this behavior by considering the Landauer transmission per spin channel derived from Eq.(3.7) if  $\epsilon_1 = \epsilon_2 = 0 \text{ meV}$  and  $\Delta = 0$ :

$$T_\sigma(E) = \frac{\gamma_L^\sigma \gamma_R^\sigma V^2}{\left[ E^2 - \left(\frac{1}{2}\right)^2 \gamma_L^\sigma \gamma_R^\sigma - V^2 \right]^2 + \left(\frac{E}{2}\right)^2 (\gamma_T^\sigma)^2},$$

the resonance energies per spin channel  $E_\pm^\sigma$ :

$$E_\pm^\sigma = \pm \sqrt{\left(\frac{1}{2}\right)^2 \gamma_L^\sigma \gamma_R^\sigma + V^2}, \quad (4.7)$$

and therefore,  $T_{max}^\sigma \equiv T_\sigma(E_\pm^\sigma)$ :

$$T_{max}^\sigma = \frac{\gamma_L^\sigma \gamma_R^\sigma V^2}{\left(\frac{\gamma_T^\sigma}{2}\right)^2 (E_\pm^\sigma)^2}, \quad (4.8)$$

where  $\gamma_\alpha^\sigma = \frac{\gamma}{2} (1 + \hat{\sigma} p_\alpha)$ , with  $\hat{\sigma} = \{+, -\}$  for spin up and down respectively.

If we consider  $p_L = p_R = 0$ , the broadening becomes:

$$\begin{aligned}\gamma_\alpha^\sigma &= \frac{\gamma}{2}, \\ \Rightarrow \gamma_L^\sigma \gamma_R^\sigma &= \left(\frac{\gamma}{2}\right)^2, \\ \Rightarrow \gamma_T^\sigma &= \gamma,\end{aligned}$$

while the transmission expression  $T_\sigma(E)$  becomes:

$$T_{\uparrow(\downarrow)}^\sigma(E) = \frac{\left(\frac{\gamma}{2}\right)^2 V^2}{\left[E^2 - \left(\frac{\gamma}{4}\right)^2 - V^2\right]^2 + \left(\frac{\gamma}{2}\right)^2 E^2}, \quad (4.9)$$

lastly,  $T_{max}^\sigma$  is, after dividing by  $\gamma$  and considering the underdamped limit  $|V| \gg |\gamma|$ :

$$T_{max}^{\uparrow(\downarrow)} = \frac{\left(\frac{V}{\gamma}\right)^2}{\left(\frac{1}{4}\right)^2 + \left(\frac{V}{\gamma}\right)^2} \approx 1,$$

we conclude the transmission per spin channel will have the same broadening  $\gamma$  and resonance  $T_{max}^{\uparrow(\downarrow)} = 1$  and thus  $T_{max} = 2$ .

We can make the analogous for  $p_L = p_R = 0.5$ :

$$\begin{aligned}\gamma_{L(R)}^\uparrow &= \frac{3}{4}\gamma, \quad \gamma_{L(R)}^\downarrow = \frac{1}{4}\gamma, & T_{max}^\uparrow &= \frac{\left(\frac{V}{\gamma}\right)^2}{\left(\frac{3}{8}\right)^2 + \left(\frac{V}{\gamma}\right)^2} \approx 1, \\ \gamma_L^\uparrow \gamma_R^\uparrow &= \left(\frac{3}{4}\gamma\right)^2, \quad \gamma_L^\downarrow \gamma_R^\downarrow = \left(\frac{1}{4}\gamma\right)^2, & \Rightarrow & \\ \gamma_T^\uparrow &= \frac{3}{2}\gamma, \quad \gamma_T^\downarrow = \frac{1}{2}\gamma, & T_{max}^\downarrow &= \frac{\left(\frac{V}{\gamma}\right)^2}{\left(\frac{1}{8}\right)^2 + \left(\frac{V}{\gamma}\right)^2} \approx 1,\end{aligned}$$

we notice that the transmission -up component will be broader than the spin down because  $\gamma_T^\uparrow > \gamma_T^\downarrow$  and the resonance in the total transmission will be the same as panel a) because  $T_{max} = T_{max}^\uparrow + T_{max}^\downarrow = 2$ .

We also make the analogous for  $p_L = 0.5, p_R = -0.5$ :

$$\begin{aligned}\gamma_L^\uparrow = \gamma_R^\downarrow &= \frac{3}{4}\gamma, \quad \gamma_L^\downarrow = \gamma_R^\uparrow = \frac{1}{4}\gamma, & T_{max}^\uparrow &= \frac{3}{4} \frac{\left(\frac{V}{\gamma}\right)^2}{\left(\frac{1}{2}\right)^2 \left(\frac{3}{16}\right)^2 + \left(\frac{V}{\gamma}\right)^2} \approx \frac{3}{4}, \\ \gamma_L^\uparrow \gamma_R^\uparrow &= \gamma_L^\downarrow \gamma_R^\downarrow = \frac{3}{16}\gamma^2, & \Rightarrow & \\ \gamma_T^\uparrow = \gamma_T^\downarrow &= \gamma, & T_{max}^\downarrow &= \frac{3}{4} \frac{\left(\frac{V}{\gamma}\right)^2}{\left(\frac{1}{2}\right)^2 \left(\frac{3}{16}\right)^2 + \left(\frac{V}{\gamma}\right)^2} \approx \frac{3}{4},\end{aligned}$$

we conclude that the transmission for spin up and spin down will have the same broadening ( $\gamma_T^\uparrow = \gamma_T^\downarrow$ ) and resonance ( $T_{max}^\uparrow = T_{max}^\downarrow$ ). However, the difference now is that  $T^{max} = \frac{3}{2} = 1.5$  because  $T_{max}^{\uparrow(\downarrow)} = \frac{3}{4} = 0.75$ .

We can summarize the influence of the previous and additional polarization values on the transmission peaks by considering Eq.(4.8):

$$T_{max}^\sigma = \frac{\gamma_L^\sigma \gamma_R^\sigma}{\left(\frac{\gamma_T^\sigma}{2}\right)^2} \frac{V^2}{(E_\pm^\sigma)^2},$$

which, after applying the weak/intermediate coupling with the electronic baths, simplifies to:

$$\Rightarrow T_{max}^\sigma = \frac{\gamma_L^\sigma \gamma_R^\sigma}{\left(\frac{\gamma_T^\sigma}{2}\right)^2}, \quad (4.10)$$

that is dependent of the spectral broadening values  $\gamma_L^\sigma$ ,  $\gamma_R^\sigma$  and  $\gamma_T^\sigma$ . Since we know that polarization term  $p_\alpha$  controls the spectral broadening, we obtain the Table 4.1 after using Eq.(4.10) for a variety of polarization term values.

Table 4.1: Max. amplitude for different polarization values

$p_L$	$p_R$	$\gamma_L^\uparrow \gamma_R^\uparrow$	$\gamma_L^\downarrow \gamma_R^\downarrow$	$\left(\frac{\gamma_T^\uparrow}{2}\right)^2$	$\left(\frac{\gamma_T^\downarrow}{2}\right)^2$	$T_{max}^\uparrow$	$T_{max}^\downarrow$	$T_{max}$
0	0	$\left(\frac{\gamma}{2}\right)^2$	$\left(\frac{\gamma}{2}\right)^2$	$\left(\frac{\gamma}{2}\right)^2$	$\left(\frac{\gamma}{2}\right)^2$	1	1	2
0.5	0.5	$\left(\frac{3}{4}\gamma\right)^2$	$\left(\frac{1}{4}\gamma\right)^2$	$\left(\frac{3}{4}\gamma\right)^2$	$\left(\frac{1}{4}\gamma\right)^2$	1	1	2
1	1	$(\gamma)^2$	0	$(\gamma)^2$	0	1	0	1
0.5	-0.5	$\left(\frac{3}{16}\gamma^2\right)$	$\left(\frac{3}{16}\gamma^2\right)$	$\left(\frac{\gamma}{2}\right)^2$	$\left(\frac{\gamma}{2}\right)^2$	0.75	0.75	1.5
1	-1	0	0	$\left(\frac{\gamma}{2}\right)^2$	$\left(\frac{\gamma}{2}\right)^2$	0	0	0
1	0	$\left(\frac{\gamma^2}{2}\right)$	0	$\left(\frac{3}{4}\gamma\right)^2$	$\left(\frac{\gamma}{4}\right)^2$	$\frac{8}{9}$	0	$\frac{8}{9}$

Therefore, if we consider for instance, the extreme case  $p_L = 1$  and  $p_R = 0$  which corresponds to the flow of only one spin channel from the  $L$ -electrode and of both spin channels from the  $R$ -electrode, we will have the profile from the Fig.4.3. We can see in 4.3a) that  $T_{max}^\uparrow = 0.89$  while in panel b)  $T_{max}^\downarrow = 0$  and therefore in c)  $T_{max} = 0.89$  because according to the Table 4.1:  $T_{max}^\uparrow = \frac{8}{9} \approx 0.89$  and  $T_{max}^\downarrow = 0$ .

We can interpret the polarization as connected to the magnetization of the contact but also to the spectral broadening. This means that the magnetic alignment of the contacts controls the density of states around the Fermi energy because of the mean lifetime. So,

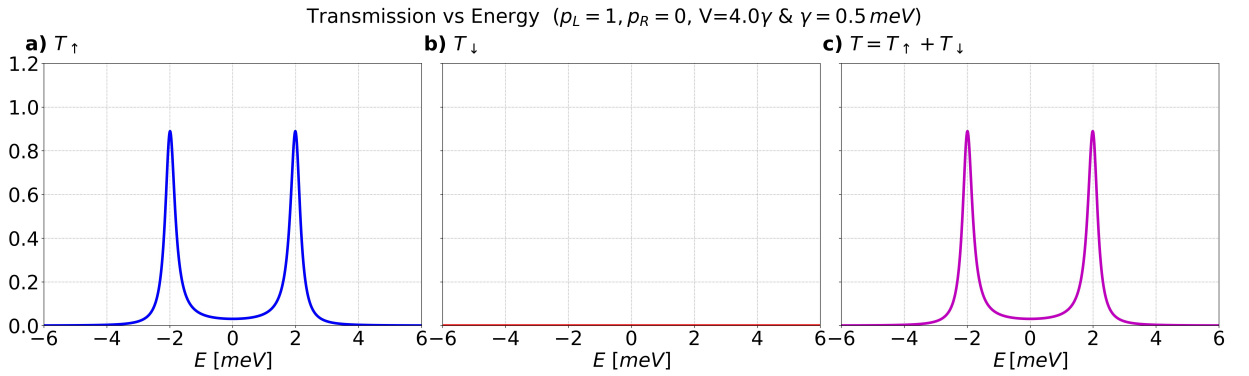


Figure 4.3: Landauer Transmission for the linear double dot model ( $\epsilon_1 = \epsilon_2 = 0 \text{ meV}$ ,  $\Delta = 0 \text{ meV}$ ,  $\gamma = 0.5 \text{ meV}$  and  $V = 4\gamma$ ) for polarization  $p_L = 1$  and  $p_R = 0$  in an energy interval of  $[-4, 4] \text{ meV}$ . The transmission is divided into spin channels: a) for spin up, b) for spin down, and c) for the total contribution of a) and b). Transmission near the Fermi energy is allowed only for one spin channel.

if we set the same polarization for both contacts (e.g. spin up  $0 < p < 1$ ), we will see that the electronic density of states with spin-up alignment in both contacts will increase or decrease according to  $p$ . This increment/decrement is expressed in the total lifetime per spin channel  $\gamma_T^\sigma$ , e.g. the first three rows in Table 4.1. Another way to understand this is if we can think that  $p_\alpha$  controls the rate of tunneling of electrons, with a given spin alignment, between the contacts and the scattering zone around the Fermi energy. So, we can make spin filtering because the electron flow per spin channel is limited or enhanced by  $p_\alpha$ , indicating the importance of the magnetization of the contacts during the spin-dependent electron transport process.

## 4.2 T-shape model: Anti- and Fano- resonances

The linear double-dot model displayed for weak to moderate coupling to the metallic contacts two well-defined transmission resonances separated by a gap controlled by the inter-dot hopping (for equal on-site energies). At resonance, the total transmission reached the maximum of two related to the degenerate spin-up and spin-down channels. We will now see that the qualitative behavior of the T-shape junction differs in some respects from the double-dot model; in particular, the phenomenon of quantum interference will appear at certain energies.

The transmission function for unpolarized metallic contacts  $p_L = p_R = 0$  and  $\Delta = 0$  is

shown in Fig.4.4. In panel a), we see that  $T(E)$  shows similar shapes as in Fig.4.1a) in the weak/intermediate coupling regime. However, as we move to the strong coupling regime, the gap remains (it does not disappear), in contrast to Fig.4.1a), where the gap vanishes in the strong coupling regime. Afterward, we notice in panel b)  $T(E)$  also shows the same behavior as Fig.4.1b) for the weak/intermediate coupling regime. However, additionally to the gap conservation, we notice the resonances do not diminish as we go to the strong coupling regime (they get preserved).

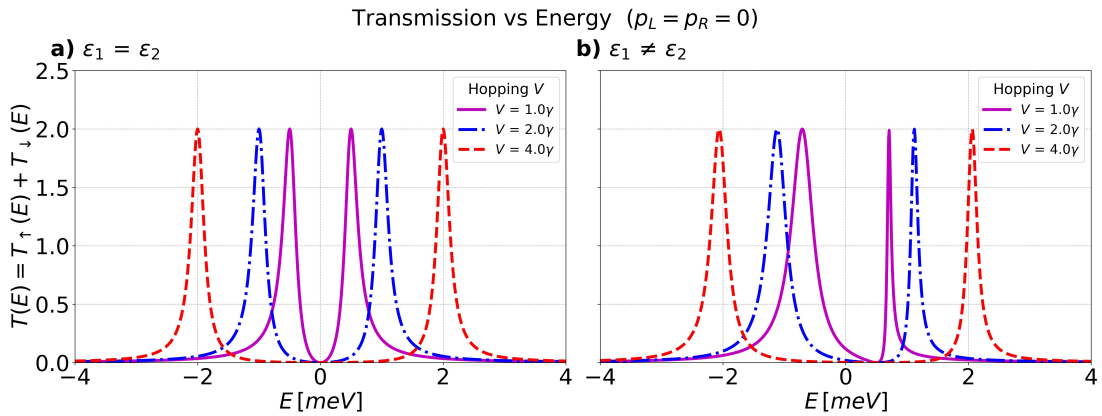


Figure 4.4: Transmission for T-shape model; when  $\Delta = 0 \text{ meV}$ ,  $\gamma = 0.5 \text{ meV}$  and  $p_\alpha = 0$ . For different values of hopping term  $V$  within an energy interval of  $[-4, 4] \text{ meV}$ , we observe distinct Quantum Interference profiles. a) When the site energies are equal, e.g.,  $\epsilon_1 = \epsilon_2 = 0 \text{ meV}$  and  $V = 1 \gamma$  we have a case of antiresonance (symmetric shape). b) When the site energies are not equal, e.g.,  $\epsilon_1 = -0.5 \text{ meV}$  and  $\epsilon_2 = 0.5 \text{ meV}$  and  $V = 1 \gamma$  we have a case of Fano resonance (asymmetric shape).

We can explain analytically the effects of the coupling regime  $\left|\frac{V}{\gamma}\right|$  and site energy  $\{\epsilon_1, \epsilon_2\}$  over the resonances in  $T(E)$  by considering the explicit expression for the transmission from Eq.(3.13) when we have unpolarized contacts  $p_\alpha = 0$  and  $\Delta = 0$ :

$$T(E) = 2 \frac{\left(\frac{\gamma}{2}\right)^2 (E - \epsilon_2)^2}{\left[(E - \epsilon_1)(E - \epsilon_2) - V^2\right]^2 + \left(\frac{\gamma}{2}\right)^2 (E - \epsilon_2)^2}, \quad (4.11)$$

$$= 2 \frac{\left(\frac{\gamma}{2}\right)^2}{\left(E - \epsilon_1 - \frac{V^2}{(E - \epsilon_2)}\right)^2 + \left(\frac{\gamma}{2}\right)^2}. \quad (4.12)$$

First, from Eq.(4.12), we can get  $T_{max}$  if [3]:

$$E - \epsilon_1 - \frac{V^2}{(E - \epsilon_2)} = 0,$$

from which we obtain the resonance energies ( $E_{\pm}$ ):

$$\Rightarrow E_{\pm} = \frac{\epsilon_1 + \epsilon_2}{2} \pm \frac{\sqrt{(\epsilon_1 - \epsilon_2)^2 + 4V^2}}{2}, \quad (4.13)$$

that if we evaluate in  $T(E)$ :

$$\Rightarrow T(E_{\pm}) = 2 \frac{\left(\frac{\gamma}{2}\right)^2}{\left(\frac{\gamma}{2}\right)^2} = 2 = T_{max}, \quad (4.14)$$

we conclude that the resonances ( $T_{max} = 2$ ) are preserved regardless of the spectral broadening strength and regardless the site energy values (see Fig.4.4) because the evaluation of the resonance energies (4.13) over  $T(E)$  leads to Eq.(4.14) that does not explicitly depend on the parameters:  $\left\{ \left| \frac{V}{\gamma} \right|, \epsilon_1, \epsilon_2 \right\}$ .

In addition to the resonance energy conservation, we notice that within the energy interval where the gap appears, there is an energy at which the transmission value is zero ( $T(E_{anti}) = 0$ ). We can explain this analytically by considering the numerator of Eq.(4.11):

$$(E - \epsilon_2) = 0 \Rightarrow E_{anti} = \epsilon_2, \quad (4.15)$$

which is called antiresonance energy, then evaluating in  $T(E)$ :

$$T(E_{anti}) = 0,$$

that also has no dependence on the site energies nor the strength of  $V$  or  $\gamma$  because the numerical value is zero. Since the gap is located at  $T(E_{anti}) = 0$ , we conclude the gap is preserved no matter the site energies nor the coupling strength  $\left| \frac{V}{\gamma} \right|$  (see Fig.4.4). This explains analytically why the gap does not disappear while variation in the site energies and coupling regime are performed in the Fig.4.4 and the reason why it is present in the Fig.4.4 but not in Fig.4.1.

Despite the resonances and antiresonance values being constant against variations, their

locations are dependent on both the site energy values and the strength of the intra-dot hopping  $V$  because Eqs.(4.13) and (4.15) are dependent on these parameters. We draw attention in Fig.4.4a) where the resonance-antiresonance profile is given according to equations (4.13) and (4.15) when  $\epsilon_1 = \epsilon_2 \equiv \epsilon$ :

$$\begin{aligned} E_{\pm} &= \epsilon \pm V, \\ E_{anti} &= \epsilon, \end{aligned} \quad (4.16)$$

this means that the curve is symmetric with respect to the antiresonance no matter the value of the intra-dot hopping  $V$  because the antiresonance energy is located at exactly the middle of the two resonance energies according to Eq.(4.16). For panel b), the resonance-gap profile is given according to the same equations, but when the site energies are not the same:

$$\begin{aligned} E_{\pm} &= \frac{\epsilon_1 + \epsilon_2}{2} \pm \frac{\sqrt{(\epsilon_1 - \epsilon_2)^2 + 4V^2}}{2}, \\ E_{anti} &= \epsilon_2, \end{aligned} \quad (4.17)$$

now, the curve is still symmetric with respect to the antiresonance for  $|V| \gg |\gamma|$  but as we approximate the intra-dot hopping to the spectral broadening ( $|V| \sim |\gamma|$ ), the curve becomes asymmetric with respect to the antiresonance because according to Eq.(4.17) the antiresonance energy is not located in the middle of the two resonances energies. Specifically  $E_{\pm}$  are symmetric with respect to  $E = \frac{\epsilon_1 + \epsilon_2}{2}$  while  $E_{anti} = \epsilon_2$ , such difference is not appreciated for larger intra-dot hopping values; however, the difference starts to become appreciable as we diminish the value of the intra-dot hopping parameter  $V$ . Lastly, we call such a remarkable asymmetric curve in Fig.4.4b) a *Fano Resonance* (FR) [3, 36].

We can explain physically the positive and negative peaks in the transmission by considering the interaction between the discrete quantum states from the sites with the continuous quantum states from the electrodes during the electron flow. Consequently, we have a superposition between the quantum mechanical waves which will produce both *quantum interference* (QI) effects i.e. constructive, where  $T \rightarrow T_{max}$ , and destructive, where  $T = 0$ . As a result, Fano resonances (FR) appear in the "critically damped and overdamped" limit due to the interference between the bound states of the sites and the tunneling continuum

states of the electrodes [36]. This behavior is different from the "identity" loss presented in the situation of the linear double dot. Additionally, we can conclude that the transmission function will exhibit antiresonance or FR depending on the ratio between the difference in the site energies ( $\epsilon_1, \epsilon_2$ ) and the coupling term (intra-dot hopping)  $V$ , Eq.(4.18)[3]:

$$\frac{|\epsilon_1 - \epsilon_2|}{|V|}. \quad (4.18)$$

Antiresonance shape appears if the ratio is lesser than the unity ( $|\epsilon_1 - \epsilon_2|/|V| \ll 1$ ) while Fano resonance appears for the opposite case ( $|\epsilon_1 - \epsilon_2|/|V| \gg 1$ ). Fano resonances has been an object of intense studies in electron-transfer to molecular and thermoelectric devices because, as we will see, they may lead to dramatic changes in the Seebeck coefficient [36]. So, by assumption, we will take the site energies as  $\epsilon_1 \neq \epsilon_2$  and the intra-dot hopping term as  $|V| \sim |\gamma|$  to consider Fano resonance effects.

#### 4.2.1 Contact polarization influence

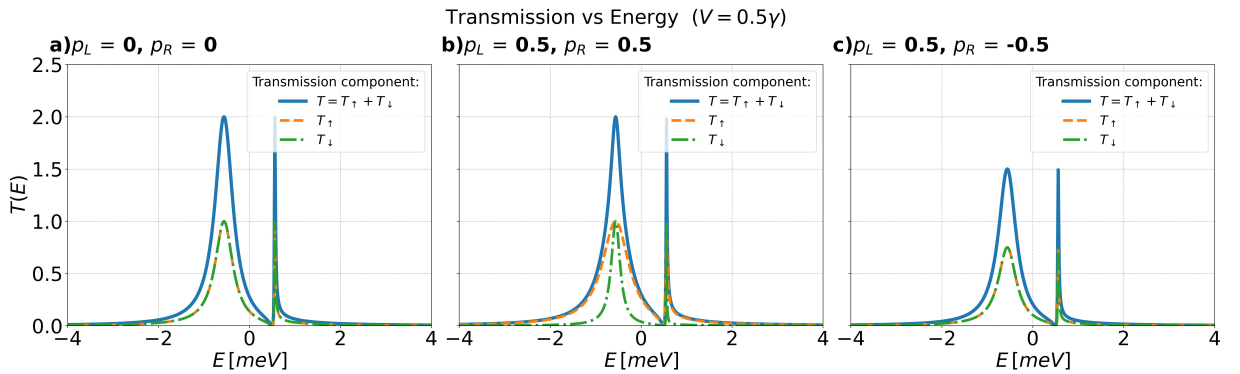


Figure 4.5: Fano resonance for different values of polarization  $p_\alpha$ . Here, the solid line represents the total transmission profile while the dashed/dash-dot is for the spin up/down transmission. The parameters are:  $\epsilon_1 = -0.5 \text{ meV}$ ,  $\epsilon_2 = 0.5 \text{ meV}$ ,  $\Delta = 0$ ,  $\gamma = 0.5 \text{ meV}$  and  $V = 0.5 \gamma$

Now, we treat the polarization effects over the transmission ( $p_L \neq 0$  and  $p_L \neq 0$ ). So, when we follow the condition for the Fano resonance from Eq.(4.18), and we include polarization effects, the transmission will exhibit the QI shapes from Fig. 4.5. We highlight that in Fig.4.5a) the asymmetric curve is conserved for the total transmission. In panel b), additionally to the asymmetric curve preservation in the total transmission, the up component of the transmission shows a broader lineshape in comparison to the spin down

component. Lastly, in panel c) the curves and broadening are preserved, but only the positive peaks variate. Therefore, we infer the influence is practically the same as the linear double dot case.

### 4.3 T-shape dimer model

The T-shape model showed not only two transmission resonances that stay stable against site energy and hopping variations, but also the existence of a well defined antiresonance transmission that is stable against the same variations as well. These resonances and antiresonance perform quantum interference effects such as Fano resonance that is presented when the difference between the site energies is greater than the intra-hopping strength in the "critically damped/overdamped" regime. Implying that the inclusion of monomers that are not connected directly to the electron baths produces FR. Here, we will show that the T-shape dimer model exhibits qualitatively the same QI peaks but also well defined symmetric curves.

From Fig.3.3, we observe a combination between the double dot and T-shape model (see Fig.3.1 and Fig.3.2), so the parameters are given based on the analysis from the previous models. Since sites  $\epsilon_1^0$  and  $\epsilon_2^0$  are aligned with the contacts and mediated by

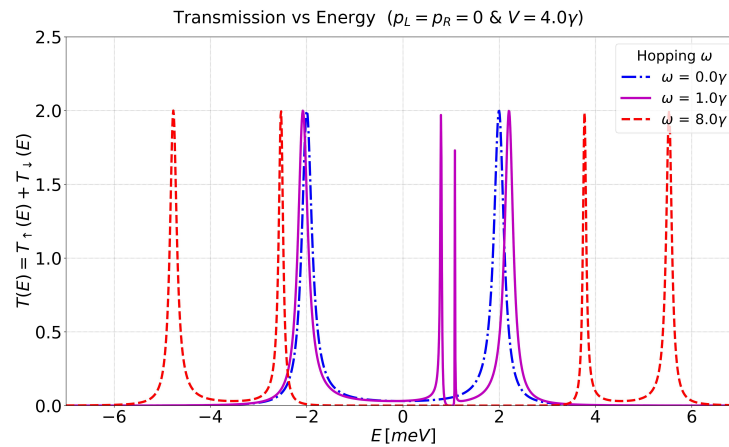


Figure 4.6: Quantum Interference profiles for the T-shape dimer model; when  $\epsilon_1^0 = \epsilon_2^0 = 0 meV$ ,  $\epsilon_1^1 = \epsilon_2^1 = 1 meV$ ,  $\Delta = 0 meV$ ,  $\gamma = 0.5 meV$ ,  $p_\alpha = 0$  and  $V = 4\gamma$ ; for different values of intra-hopping  $\omega$ .

the hopping  $V$  (called inter-hopping), we set the same site energies  $\epsilon_1^0 = \epsilon_2^0 = 0 meV$  and weak/intermediate environment-contact coupling  $V = 4\gamma$  to be similar to the linear double

dot model. On the other hand, since sites  $\epsilon_1^1$  and  $\epsilon_2^1$  ensembles a T configuration with  $\epsilon_1^0$  and  $\epsilon_2^0$  respectively, mediated by the hopping  $\omega$  (called intra-hopping), we set  $\epsilon_1^1 = \epsilon_2^1 = 1 \text{ meV}$  by convenience because it is the most simple setup that accomplishes the conditions from the T model to obtain FR while  $\omega$  is allowed to take any value because the resonance-antiresonance stability against to the intra-hopping variations. Thus, the corresponding Landauer transmission curve for these parameters and unpolarized electrodes  $p_\alpha = 0$  is shown in Fig.4.6.

We can see in Fig.4.6 the transmission for different values of intra-hopping. For large values, the transmission shows 4 peaks mediated by a big gap that separates it into two groups of peaks, each one almost similar to the double-dot case. While,  $|\omega| \sim |\gamma|$ , the gap gets reduced while the symmetric peaks begin to get deformed until they produce Fano resonances, for values  $|\omega| \sim |\gamma|$  which accomplish  $|\epsilon_i^1 - \epsilon_i^0|/|\omega| \gg 1$ . After, the component related to the T model is turned off when  $\omega = 0$ , as a result the standard shape of a transmission for double-dot model is performed (see Fig. 4.1). By assumption we will take the case where FR appears (i.e.,  $|\gamma| > |\omega| > 0 \Rightarrow |V| \gg |\omega| > 0$ ).

We can understand physically the system by first considering the linear double dot model. In this sense, the tunneling states during the electron flow will be more rich and stable in the eigenstates of the system (energy resonances  $E_\pm$ ) because of the weak electrodes-system coupling. Now, considering the T-shape model, Fano resonance appears because the bound states from the sites will interfere with the mentioned tunneling states. Consequently, this implies that we can add QI effects (e.g., Fano resonance) to a given system by the addition of new sites that are not connected to the central tunneling path.

### 4.3.1 Contact polarization influence

If we include magnetic influence to the FR profile, i.e.  $p_L \neq 0$  and  $p_R \neq 0$ , the transmission will exhibit the shapes shown in Fig.4.7. We notice that the profiles exhibit the merging of the Fano resonances into a single one for  $|\omega| < |\gamma|$ . And, as it was mentioned before, the polarization only changes the maximum amplitude and preserves the FR profile, as the double-dot and T-shape configurations.

Finally, we can conclude that the extra degrees of freedom given by the spin (i.e., polarization and magnetic effects) will not affect the transmission (total and per spin

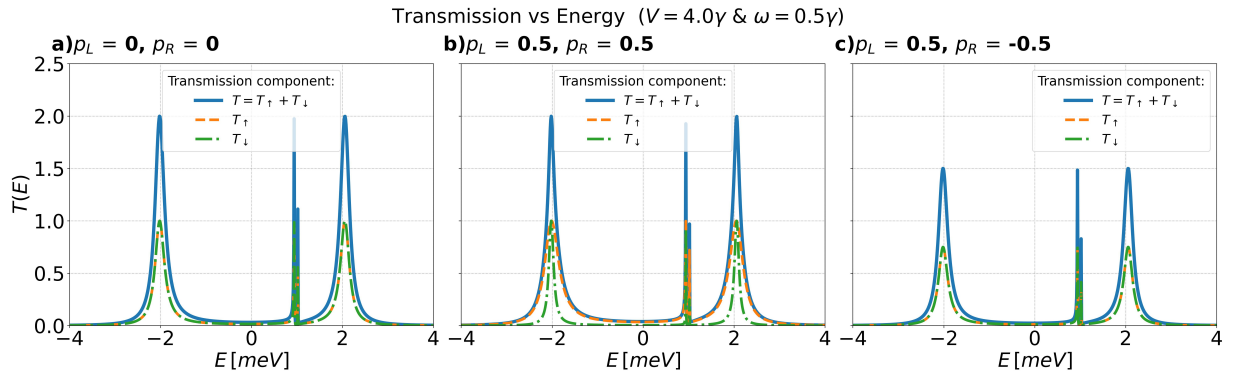


Figure 4.7: Fano resonance for the T-shape dimer model; when  $\epsilon_1^0 = \epsilon_2^0 = 0 \text{ meV}$ ,  $\epsilon_1^1 = \epsilon_2^1 = 1 \text{ meV}$ ,  $\gamma = 0.5 \text{ meV}$ ,  $V = 4\gamma$  and  $\omega = 0.5\gamma$ ; for different values of polarization  $p_\alpha$ . Here, the solid line represents the total transmission profile while the dashed/dash-dot is for the spin up/down transmission.

channel) more than in the maxima flow rate and broadening. To put it another way, we are making spin filtering based on the application of external magnetic fields.

## 4.4 Michaeli-Geyer Model: CISS effect

The T-shape dimer model shows a transmission profile that has Fano resonances in the gap from the T-shape model and two well-defined resonances in the underdamped regime from the linear double dot model. So far, we also notice that spin filtering is performed if magnetic fields are applied in the electrodes, otherwise not.

We will now see a helical model from a simplified point of view. As a result, we see qualitatively that spin filtering can be achieved not only through magnetic fields but also through chiral (not necessarily helical) geometries.

The transmission profiles for the case where the electrodes have zero polarization, also called non-magnetic (NM) electrodes, are shown in Fig.4.8 for the interval energy of  $[-6, 6] \text{ meV}$ . In panel a) from Fig.4.8, we observe two curves. The dashed line curve (when  $L = 0$ ) displays the same profile with two peaks at the eigenstates of the system as the spin up component transmission from Fig.4.2a), while the solid line curve (when  $L = +1$ ) displays four peaks at the four eigenstates of the system in which two of them have their maxima value at  $T_\uparrow \sim 0.9$ , while the remaining two at  $T_\downarrow \sim 0.1$ . In panel b) we have the same behavior as a) but now for  $L = +1$  the peaks  $T_\downarrow \sim 0.1$  are at the energy location where  $T_\uparrow \sim 0.9$  in panel a), the same happens for  $T_\downarrow \sim 0.1$  respect to  $T_\uparrow \sim 0.9$ . In

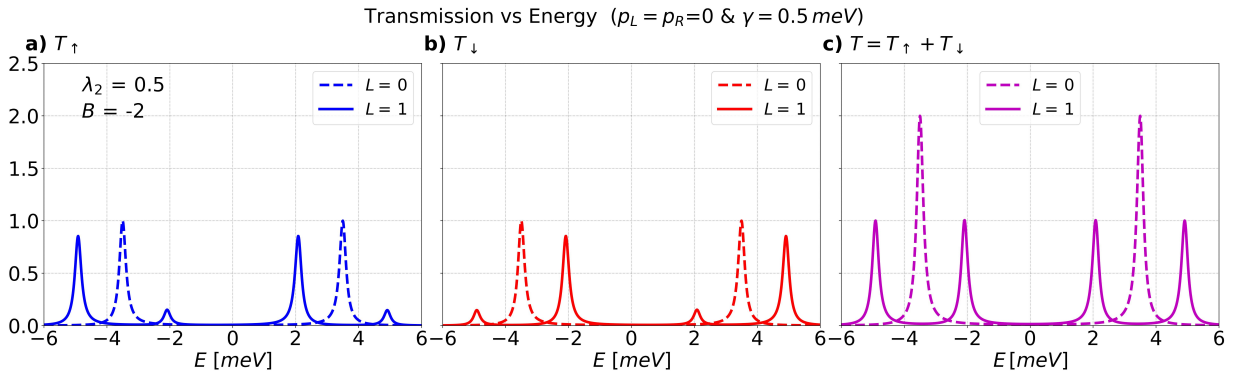


Figure 4.8: Landauer transmission for the simplified chiral molecule [10] ( $n=2$  lattice sites case) for the angular momentum ( $L = 0, +1$ ),  $\epsilon_1 = \epsilon_2 = 0 \text{ meV}$ ,  $\gamma = 0.5 \text{ meV}$ ,  $t = 7\gamma$ ,  $\lambda_2 = 0.5$  and  $B = -2$ . The transmission is divided into spin channels: a) for spin up, b) for spin down, and c) for the total contribution of a) and b). When  $L = 0$ , we recover the linear double dot case (dashed lines); for  $L = +1$ , we have the CISS effect due to the coupling in the spin orbit term (solid line).

panel c) we have the curves produced by adding the previously curves. As a result, we see that when  $L = 0$  we recover the linear double dot case. Since the spin polarization results from breaking time-reversal symmetry (TRS) upon selection of a given value  $L$  [10], we will assume  $L = +1$  as fixed from now on.

From the four peaks for  $L = +1$  in  $T(E)$ , we understand that each of the original eigenstates from the system, that were 2, suffer a spin splitting despite no external magnetic field is applied during the net current flow. We can explain physically such result by noting the terms  $\pm\lambda_2 LB$  in the main diagonal of Eq.(3.22) which plays a role analogous to  $\Delta \neq 0$ . So, one may guess that the spin-orbit interaction (SOI) involved is a type of Zeeman splitting due to the presence of the effective magnetic field  $\mathbf{B}$ , as we can observe in Eq.(3.21). However, according to Ref. [10],  $\mathbf{B}$  is derived from the projection of the spin-orbit coupling (SOC) term from the 3-dimensional to the 1-dimensional effective model. This SOC term in the 3 dimensional system comes from a generic scalar field, not necessarily an electromagnetic one, which is constructed upon the Frenet frame coordinates, indicating that  $\mathbf{B}$  is endowed with a geometric origin tied to the holonomic constraints of the helical path instead of the usual electromagnetic origin, e.g. electrons' motion in the helical path. Consequently, it is more appropriate to refer to  $\mathbf{B}$  as a "geometric" magnetic field rather than an effective magnetic field. And, since this geometric magnetic field gets preserved in the discrete simplified version as well (see Eq.(3.21)), we conclude that the dimer-like model

inherits the geometric magnetic field of the complex 1D effective model, and such magnetic field will not break the time-reversal invariance (TRS). Since this Zeeman splitting is not produced by an standard external magnetic field as it usually is, we will refer to this as a quasi-Zeeman splitting from now on.

Additionally, from the maxima values in the peaks for  $T_\sigma(E)$ , we understand that during the electron flow, particles with a given spin orientation are realigned in the opposite direction due to the interaction between the geometric magnetic field and the intrinsic dipole moment of the electrons. As a result, we see the chiral system will perform the electron flow in a preferential spin orientation for a given eigenstate of the system, a spin filtering process is happening. Such a phenomenon is the so called Chirality Induced Spin Selectivity (CISS) effect.

The CISS effect implies that a chiral molecule, not necessary helical, can perform spin filtering/polarization without the needed of a external magnetic field. Such polarization can be quantified as follows. If we compute the total transmission  $T(E)$  for a case with

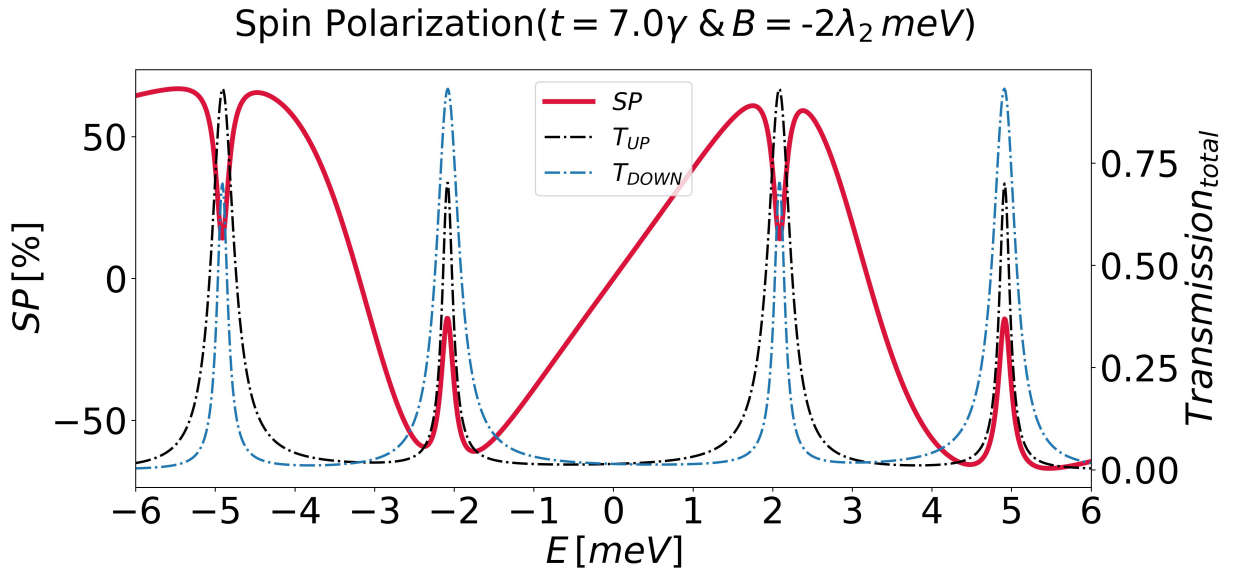


Figure 4.9: Spin Polarization (solid red line) and Landauer transmissions (dashed black and blue lines) for  $\epsilon_1 = \epsilon_2 = 0$  meV,  $\gamma = 0.5$  meV,  $t = 7\gamma$ ,  $\lambda_2 = 0.5$ ,  $B = -2$  and  $L = +1$ .  $T_{UP}$  highlights the Transmission for  $p_L = 1$ ,  $p_R = 0$ .  $T_{DOWN}$  highlights the Transmission for  $p_L = -1$ ,  $p_R = 0$ .

Ferromagnetic-Nonmagnetic (FM-NM) contacts, i.e.  $p_L = 1$ ,  $p_R = 0$  and  $p_L = -1$ ,  $p_R = 0$ ; we will obtain the transmissions  $T_{UP}$  and  $T_{DOWN}$ , respectively, which serve to compute the percentage of spin polarization ( $SP$ ), Eq. (4.19), to measure the effectiveness of the

chiral system to be a spin filter,

$$SP = \frac{T_{UP} - T_{DOWN}}{T_{UP} + T_{DOWN}} \cdot 100\%. \quad (4.19)$$

Fig.4.9 shows the profiles of  $T_{UP}$ ,  $T_{DOWN}$ , and  $SP$ . We note that the maximum spin polarization is approximately 60%, indicating that the chiral structure aligns the majority of the total electron spins in the up orientation. Conversely, the minimum spin polarization is around  $-60\%$ , indicating a preference for the down orientation. In this regard, it is observed that  $SP$  favors the up orientation for energy intervals corresponding to  $[-6, -4] \text{ meV}$  and  $[1, 3] \text{ meV}$  where there are two of the four eigenstates of the system, while it favors the down orientation for intervals corresponding to  $[-3, -1] \text{ meV}$  and  $[4, 6] \text{ meV}$  where there are two remained eigenstates. However, an unexpected reversal in spin alignment preference is noted at the energy resonances. It is important to mention that these behaviors are smooth, indicating a gradual transition in  $SP$  alignment along the curve.

As conclusion, the Michaeli-Geyer model proves that the CISS effect consists of producing a spin polarization in the continuous tunneling quantum states from the contacts and a quasi-Zeeman splitting in the discrete quantum states from the sites due to the helical geometry, that prefers to allow the passing of particles with a unique spin alignment further than the other. Additionally, the results demonstrate that the linear-double dot model can fully inherit the effects of the helical model (i.e., quasi-Zeeman splitting and spin filtering). So, these results can be used for molecules with chiral centers or even include new structures for the analysis and generalize such results to the helical system version.

## 4.5 Extended Michaeli-Geyer model: Fano resonance and Spin Polarization

From the Micheli-Geyer model, we learn that chiral geometries can replicate the effects of a magnetic field, such as the quasi-Zeeman splitting, which does not break the TRS, and the spin filtering, which occurs when TRS is broken, all without the need to apply an external magnetic field. Additionally, we can quantify such effects with the spin polarization percentage. Now, in this modified model, we will see qualitatively how the Fano resonance

affects the spin filtering process.

We can see in Fig.4.10 the resulting transmission (per spin channel and total) profile for the angular momentum  $L = +1$  over the interval energy of  $[-6, 6] \text{ meV}$  for the same parameters given in Sec.4.4 and Sec.4.3. We can see the overall analysis is analogous

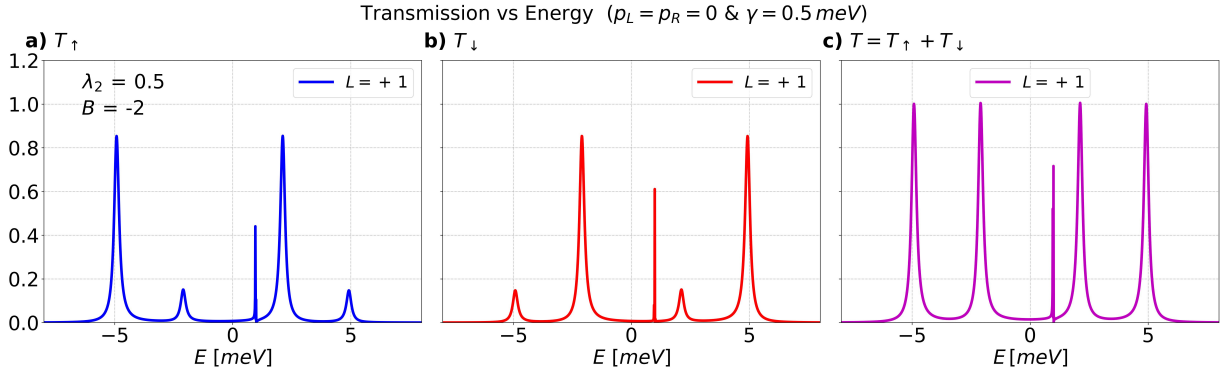


Figure 4.10: Landauer transmission (QI profiles) for the simplified chiral molecule [10] ( $n=2$  lattice sites case), including side dots, for the angular momentum  $L = +1$ :  $\epsilon_1^0 = \epsilon_2^0 = 0 \text{ meV}$ ,  $\epsilon_1^1 = \epsilon_2^1 = 1 \text{ meV}$ ,  $\gamma = 0.5 \text{ meV}$ ,  $t = 7\gamma$ ,  $\omega = 0.4\gamma$ ,  $\lambda_2 = 0.5$  and  $B = -2$ . For  $L = +1$  we have the spin filtering due to the coupling in the spin orbit term. Additionally, we have Fano resonances.

to the one performed in the Michaeli-Geyer model with respect to the linear double dot model. Since for  $L = 0$ , we recover the T-shape dimer model case, where we notice the appearance of Fano resonances as the result of the interaction between continuous and discrete quantum states (more information see Ch.4.3), we thus drop such value from the figure. So, when  $L = +1$ , we recover the profile of the chiral model presented in Fig.4.8 but including Fano resonances due to the inclusion of new sites  $\epsilon_i^1$  to the "chiral" linear double-dot configuration of  $\epsilon_i^0$  via intrahopping  $\omega$ , which produces a destructive quantum interference effect. We draw attention to the appearance of only one FR due to the small value given to the intrahopping  $\omega$  as it was mentioned in Ch.4.3.

As the previous section, we compute the total transmission  $T(E)$  for  $p_L = 1$ ,  $p_R = 0$  and  $p_L = -1$ ,  $p_R = 0$ ; to obtain  $T_{UP}$ ,  $T_{DOWN}$  and  $SP$ . But in this case, we will study whether FR affects the effectiveness of the chiral system as a spin filter. Fig.4.11 presents  $T_{UP}$ ,  $T_{DOWN}$  and  $SP$  profiles. We notice an abruptly increasing and decreasing of  $SP$  at the same location for the FR in  $T_{UP}$  and  $T_{DOWN}$ .

Lastly, we can organize the behavior of the chiral-like dimers to be a spin filter in the

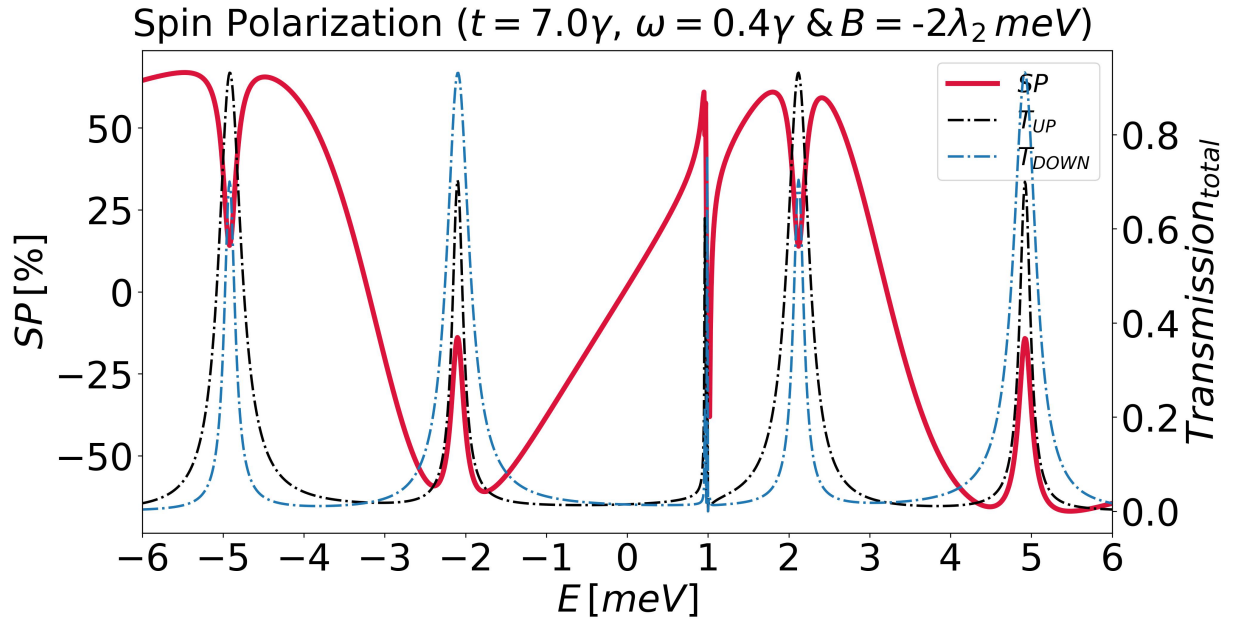


Figure 4.11: Spin Polarization (solid red line) and Landauer transmissions (QI profiles) for  $\epsilon_1^0 = \epsilon_2^0 = 0 \text{ meV}$ ,  $\epsilon_1^1 = \epsilon_2^1 = 1 \text{ meV}$ ,  $\gamma = 0.5 \text{ meV}$ ,  $t = 7\gamma$ ,  $\omega = 0.4\gamma$ ,  $\lambda_2 = 0.5$  and  $B = -2$ .  $T_{UP}$  (dashed black line) highlights the transmission for  $p_L = 1$ ,  $p_R = 0$ .  $T_{DOWN}$  (dashed blue line) highlights the Transmission for  $p_L = -1$ ,  $p_R = 0$ .

Table 4.2. We can conclude that FR profile affects through the inclusion of a *discontinuity* in the  $SP$  behavior. This discontinuity indicates that spin polarization can abruptly change sign within an incredibly small energy interval.

Table 4.2: Spin filtering behavior for chiral-like dimers

$SP$	Michaeli-Geyer	Extended Michaeli-Geyer
Discontinuity	✓	×

## 4.6 Thermopower analysis

We learned about electron and spin transport aspects of the dimer-like systems. The wire-like dimer configurations showed that electron (charge) transport rates reach their maximum at energies that belong to the eigenstates of the system. Such eigenstates will change depending on the coupling between monomer-monomer (hopping terms) and monomer-electrodes (tunneling terms), producing QI phenomena like anti- and Fano resonances. The chiral-like dimer configurations showed the preference of the electron transport in a determined alignment (spin) at the same eigenstates for molecules that follow the men-

tioned geometry. Now, we will address a related aspect that we have overlooked until now; heat transport. The heat transport analysis is linked to the electron and spin transport because it reflects how efficient they are. Generally, as heat transport increases, electron transport decreases. However, under certain conditions, heat can enhance the electron, and thus spin transport. Specifically, we want to deal with the Seebeck effect in the chiral molecules with and without QI effects. So, we will qualitatively see the conditions and the efficiency in which the heat flows produce charge and spin flows in chiral molecules and whether this efficiency can be enhanced by including quantum interference (QI) effects.

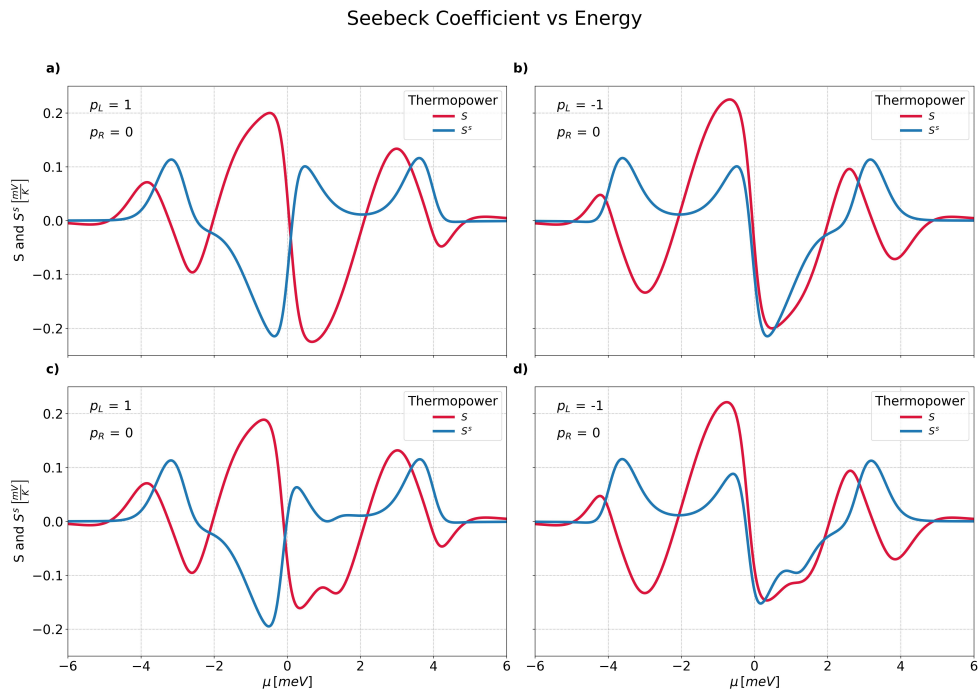


Figure 4.12: Charge (red line) and Spin (blue line) thermopower for a) the Michaeli-Geyer model based on  $T_{UP}$ , b) based on  $T_{DOWN}$ , c) the Michaeli-extended model based on  $T_{UP}$  and d)  $T_{DOWN}$ . The analysis was performed under cryogenic conditions (approximately  $T = 3K$ ).

Fig.4.12 shows the Seebeck Coefficient (SC)  $S$  and its spin extension, the Spin Seebeck Coefficient (SSC)  $S^s$ , for the Michaeli-Geyer model and its modified model upon the previously computed  $T_{UP}$  and  $T_{DOWN}$  for a range of energies around the fermi level  $\mu$ . The calculations were performed in the low-temperature regime, approximately near from the liquid helium boiling point ( $T=4.2$  K), where the quantum effects dominates. In panel a) and c) we see that the red line curve, which states for  $S$ , has three peaks and three valleys that are associated to regions between resonances of the  $T_{UP}$  spectrum (see Figs.4.9

and 4.11). The blue line curve, which states for  $S^s$ , has also peaks and valleys associated to regions between resonances in  $T_{UP}$ . For the remaining b) and d) panels we have the same behavior, the peaks and valleys are associated to regions between resonances in the transmission spectra  $T_{DOWN}$  (see Figs.4.9 and 4.11).

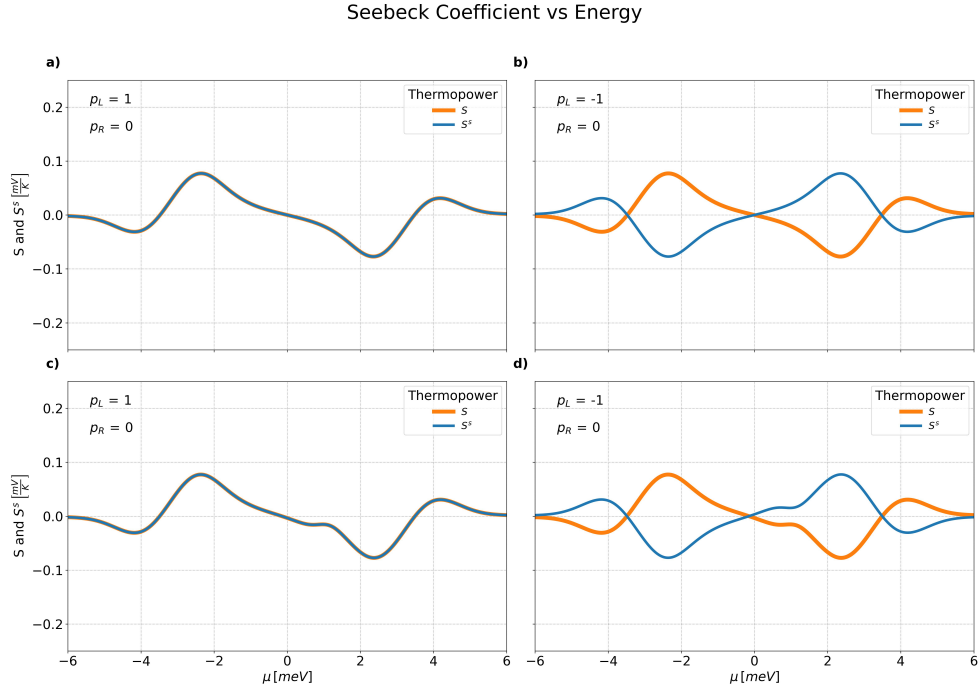


Figure 4.13: Charge (orange line) and Spin (blue line) thermopower for a) the linear double-dot model based on  $T_{UP}$ , b) based on  $T_{DOWN}$ , c) the T-shape dimer model based on  $T_{UP}$ , and d)  $T_{DOWN}$ . The analysis was performed under cryogenic conditions (approximately  $T = 3K$ ).

To understand the effect of the chiral geometry, we calculate numerically  $S$  and  $S^s$  for the wire-like dimer configurations (see Fig.4.13). By comparing Fig.4.12 and Fig.4.13, we observe that the chiral geometry has a significant impact on the efficiency of converting heat to electric and spin currents ( $S$  and  $S^s$ ) because the peaks and valleys of the wire-like dimer configurations are generally around  $|S| \sim |0.1|$ , whereas those of the chiral-like dimer configurations are approximately  $|S| \sim |0.2|$ , which is twice as large.

We conclude that chiral-like dimers can produce spin currents from temperature differences through the Spin Seebeck effect (SSE), indicating their potential as thermal spin filters. This result suggests possible applications from a design perspective. For example, the array of laterally coupled double quantum dots (DQDs) studied by Fu *et al.* demonstrated that, by applying an external magnetic field, the coupled DQD array can function

as a perfect thermal spin filter [9]. Given that the DQD array does not need to be very large for device applications and the relative facility of QDs structure fabrication, we may infer a potential application of the extended Michaeli-Geyer model to approximate a system of two laterally coupled DQDs but including, in some way, the chirality. This is because the chirality of the system replaces the external magnetic field, yielding the spin filtering behavior observed in the work of Fu *et al.* [9]. Alternatively, a generalization of this model to a large helical path is also considered for approximating an array of laterally coupled DQDs but forming a helical path. In any case, both ideas deserves further studies in future works.

Now, in order to understand the effect of Fano resonances inclusion in the chiral-like configuration, we must compare the  $S$  and  $S^s$  profiles in panels a) and b) with those in panels c) and d) of Fig.4.12. For the  $S$  profile, we see that the Fano resonance has a small impact on efficiency because, in c), we observe a finite discontinuity instead of the usual valley seen in a), around the energies where FR appears in the transmission spectra, i.e.,  $E_{anti} = \epsilon_n^1 = 1, meV$  (see Fig.4.11). The same happens for the spin Seebeck coefficient in which the discontinuity appears in the same interval energy. Such discontinuities change the values in the efficiency from  $S = -0.2$  and  $S^s = 0.1$ , see panel a), to  $S \approx -0.15$  and  $S^s \approx 0.5$ , see panel c). We find similar results if we compare b) with respect to d).

Consequently, since the maximum efficiency is obtained if  $|S| \rightarrow 1$  and  $|S^s| \rightarrow 1$ , we could conclude that the FR would not enhance the efficiency of the conversion of heat into charge and spin currents in chiral-like dimer configurations. Actually, we assert that FR would reduce the efficiency because  $|S| \rightarrow 0$  and  $|S^s| \rightarrow 0$  in the antiresonance energy  $E_{anti}$ .

However, when comparing with other works (Refs. [9, 51, 52, 53]), we find different results, as FR is generally expected to enhance the efficiency of this conversion. This inconsistency may arise from the specific assumptions employed in each model. For instance, in molecular junction devices, we find such efficiency increment when the FR is located near the Fermi level [51]. In lateral quantum dots, the enhancement in the thermopower is pronounced in the vicinity of the FR [52] and when we deal in a specific low-temperature regime [9, 52]. Tunneling and hopping are also crucial factors, being that the coupling between contacts/electrodes and the scattering system (represented by  $\gamma$ ) must deal in the

strong coupling regime, i.e.  $|\gamma| > |V| \Rightarrow \left| \frac{V}{\gamma} \right| < 1$  [9, 52]. This is because, in the weak coupling regime, strong correlations for the inter-dot hopping ( $V$ ) change the picture of the physical properties in unexpected manners [51] that can be non-beneficial.

In conclusion, the limitation of the model in thermoelectric conversion due to FR arises from selecting not only the weak coupling to the electron baths  $\left( \left| \frac{V}{\gamma} \right| \gg 1 \right)$  in which the "identity" loss is avoided but also a temperature regime that is not considered in the lateral double quantum dots systems [9]. However, if we assume a strong coupling, although the desired enhancement due to FR would be obtained, we will be subjected to the "identity" loss of the eigenstates of the system, as it is mentioned in the chapter 4.1.

Therefore, an appropriate choice of the tunneling parameter in our model is guided by balancing the perspectives of the two coupling regimes. A suitable candidate is  $|V| > |\omega| > 0$ , which corresponds to the intermediate coupling regime. In addition to the tunneling choice, we have to consider an appropriate low-temperature regime. A suitable candidate is  $0.12K < T < 1.2K$ , temperature regimes utilized by Fu *et al.* for the DQDs array [9]. In any case, the thermoelectric efficiency is significantly influenced by the tunneling and specific low-temperature regimes, often overlooked aspects in this thesis that warrant further exploration in future works.

# Chapter 5

## Conclusions

In this thesis, numerical computations based on Green's function formalism were performed to obtain the transmission coefficients in dimer-like systems with both straight and chiral geometries. These computations revealed that chiral-like dimers behave similarly to wire-like dimers subjected to external magnetic fields, although these effects are induced solely by the chiral geometry. Consequently, the computations were used to obtain the thermopower  $S$  and spin thermopower  $S^s$  from where we saw qualitatively the effect of chiral geometries over two-terminals transport processes in comparison to the wire geometry case.

We conclude that transport per spin channel from contacts depends on the magnetization that controls the population of the electronic density of states near to the Fermi energy for a given spin alignment, and such magnetization is modulated numerically by the polarization term of the contacts. As a result, we obtain a spin polarization based on the magnetization of the contacts.

From the electron transport between nonmagnetic contacts mediated by wire-like dimer models, we highlight transmission shapes without quantum interference for the linear double dot model and T-shape dimer model (for zero intrahopping value), and the opposite for the T-shape model and T-shape dimer model (for non-zero intrahopping values). Specifically, if the intrahopping term is larger with respect to spectral broadening, the quantum interference (QI) will exhibit a normal antiresonance pattern. For smaller intrahopping terms with respect to spectral broadening but different from zero, the QI shape exhibits a Fano resonance (FR) pattern. Fano resonances are special because they show the interaction (superposition) between the continuous quantum states from the terminals (contacts)

and the discrete quantum states of the sites. Therefore, we conclude that the inclusion of sites not connected directly to the contacts (i.e., side sites) induces QI phenomena and such phenomena can become FR due to the adequate tuning of the correlations given by the intra- and inter-dot hopping.

Additionally, from the electron and spin transport between ferromagnetic and non-magnetic contacts mediated by the simplified version of the Michaeli-Geyer model, we observe that the chiral-like dimer model induces a quasi-Zeeman splitting due to the effective magnetic field inherited from the spiral model. This field does not break time-reversal symmetry (TRS), but it is possible to break it upon election of an angular quantum number and thus obtain spin polarization. Lastly, the inclusion of side sites in the modified model introduces quantum interference (QI) phenomena. Specifically, Fano resonance appears in the spin-polarized current as asymmetrical discontinuities.

Finally, although Fano resonances appear in both charge and spin transmission coefficients as abrupt discontinuities, we observe that their influence on thermopower and spin thermopower is controlled. Additionally, these discontinuities have proven to shift the efficiency from values far from zero to values close to zero within the energy interval where FR happens. In conclusion, we find that Fano resonances may decrease the efficiency of chiral-like dimer models. However, such results have been proven in the weak tunneling coupling regime and at  $T = 3K$ .

Our findings that were proven for dimer-like models can serve as a reference for investigations in molecules with chiral centers and even for helical molecules. However, for helical systems, further investigations need to be performed to see whether such results can be generalized to spiral geometries. Additionally, further investigation into both tunneling coupling and temperature regimes is also needed to determine whether FR can enhance efficiency. Finally, from a design standpoint, we can suggest possible approximations for quantum dots systems in order to develop perfect thermal spin filters, which also needs more investigations.

# Bibliography

- [1] J. A.-P. Haug H., *Quantum Kinetics in Transport and Optics of Semiconductors*, 2nd ed., ser. Springer Series in Solid-State Sciences, 123. Springer, 2008. [Online]. Available: <http://gen.lib.rus.ec/book/index.php?md5=684b71233f050f7d621925939e5b46c1>
- [2] M. Shirdel-Havar and R. Farghadan, “Thermal magnetoresistance and spin thermopower in c60 dimers,” *Journal of Physics: Condensed Matter*, vol. 32, no. 28, p. 285302, 2020.
- [3] D. Nozaki, S. M. Avdoshenko, H. Sevinçli, R. Gutierrez, and G. Cuniberti, “Prediction of quantum interference in molecular junctions using a parabolic diagram: understanding the origin of fano and anti-resonances,” in *Journal of Physics: Conference Series*, vol. 427, no. 1. IOP Publishing, 2013, p. 012013.
- [4] J. Barański and T. Domański, “Fano-type interference in quantum dots coupled between metallic and superconducting leads,” *Physical Review B—Condensed Matter and Materials Physics*, vol. 84, no. 19, p. 195424, 2011.
- [5] A. Ptok, K. Rodríguez, and K. J. Kapcia, “Superconducting monolayer deposited on substrate: Effects of the spin-orbit coupling induced by proximity effects,” *Physical Review Materials*, vol. 2, no. 2, p. 024801, 2018.
- [6] Q.-f. Sun and X. Xie, “Quantum transport through a graphene nanoribbon–superconductor junction,” *Journal of Physics: Condensed Matter*, vol. 21, no. 34, p. 344204, 2009.
- [7] K. Esfarjani, M. Zebarjadi, and Y. Kawazoe, “Thermoelectric properties of a nanocontact made of two-capped single-wall carbon nanotubes calculated within the

- tight-binding approximation,” *Physical Review B—Condensed Matter and Materials Physics*, vol. 73, no. 8, p. 085406, 2006.
- [8] X.-F. Chen, W. Luo, T.-F. Fang, Y. Paltiel, O. Millo, A.-M. Guo, and Q.-F. Sun, “Topologically nontrivial and trivial zero modes in chiral molecules,” *Physical Review B*, vol. 108, no. 3, p. 035401, 2023.
- [9] H.-H. Fu and K.-L. Yao, “Perfect thermal spin filter and pure spin thermoelectric generator based on a laterally coupled double quantum-dot array,” *Europhysics Letters*, vol. 103, no. 5, p. 57011, 2013.
- [10] M. Geyer, R. Gutierrez, and G. Cuniberti, “Effective hamiltonian model for helically constrained quantum systems within adiabatic perturbation theory: Application to the chirality-induced spin selectivity (ciss) effect,” *The Journal of chemical physics*, vol. 152, no. 21, 2020.
- [11] McGraw-Hill, *McGraw Hill Encyclopedia of Science Technology*, 10th ed., ser. McGraw Hill Encyclopedia of Science and Technology. McGraw-Hill Professional, 2007, vol. Volume 18. [Online]. Available: <http://gen.lib.rus.ec/book/index.php?md5=8c139825cb382f9b628015c746d981f4>
- [12] I. P. Dilip Kondepudi, *Modern Thermodynamics: From Heat Engines to Dissipative Structures*, 2nd ed. Wiley, 2014. [Online]. Available: <http://gen.lib.rus.ec/book/index.php?md5=64d9209a9ba09456424bb360d538cc9b>
- [13] S. Maekawa, T. Kikkawa, H. Chudo, J. Ieda, and E. Saitoh, “Spin and spin current—from fundamentals to recent progress,” *Journal of Applied Physics*, vol. 133, no. 2, 2023.
- [14] G. E. Moore, “Cramming more components onto integrated circuits,” *Proceedings of the IEEE*, vol. 86, no. 1, pp. 82–85, 1998.
- [15] M. D. Stiles and J. Miltat, “Spin-transfer torque and dynamics,” *Spin dynamics in confined magnetic structures III*, pp. 225–308, 2006.

- [16] A. Tulapurkar, Y. Suzuki, A. Fukushima, H. Kubota, H. Maehara, K. Tsunekawa, D. Djayaprawira, N. Watanabe, and S. Yuasa, “Spin-torque diode effect in magnetic tunnel junctions,” *Nature*, vol. 438, no. 7066, pp. 339–342, 2005.
- [17] T. Yang, T. Kimura, and Y. Otani, “Giant spin-accumulation signal and pure spin-current-induced reversible magnetization switching,” *Nature Physics*, vol. 4, no. 11, pp. 851–854, 2008.
- [18] G. E. Bauer, E. Saitoh, and B. J. Van Wees, “Spin caloritronics,” *Nature materials*, vol. 11, no. 5, pp. 391–399, 2012.
- [19] S. R. Boona, R. C. Myers, and J. P. Heremans, “Spin caloritronics,” *Energy & Environmental Science*, vol. 7, no. 3, pp. 885–910, 2014.
- [20] K. Ray, S. Ananthavel, D. Waldeck, and R. Naaman, “Asymmetric scattering of polarized electrons by organized organic films of chiral molecules,” *Science*, vol. 283, no. 5403, pp. 814–816, 1999.
- [21] R. Naaman and D. H. Waldeck, “Spintronics and chirality: spin selectivity in electron transport through chiral molecules,” *Annual review of physical chemistry*, vol. 66, no. 1, pp. 263–281, 2015.
- [22] C. D. Aiello, J. M. Abendroth, M. Abbas, A. Afanasev, S. Agarwal, A. S. Banerjee, D. N. Beratan, J. N. Belling, B. Berche, A. Botana *et al.*, “A chirality-based quantum leap,” *ACS nano*, vol. 16, no. 4, pp. 4989–5035, 2022.
- [23] D. K. Bhowmick, T. K. Das, K. Santra, A. K. Mondal, F. Tassinari, R. Schwarz, C. E. Diesendruck, and R. Naaman, “Spin-induced asymmetry reaction—the formation of asymmetric carbon by electropolymerization,” *Science advances*, vol. 8, no. 31, p. eabq2727, 2022.
- [24] B. P. Bloom, Z. Chen, H. Lu, and D. H. Waldeck, “A chemical perspective on the chiral induced spin selectivity effect,” *National Science Review*, p. nwae212, 06 2024. [Online]. Available: <https://doi.org/10.1093/nsr/nwae212>

- [25] I. N. Zambrano García, “Tunneling through a spin barrier in chiral molecules,” B.S. thesis, Universidad de Investigación de Tecnología Experimental Yachay, 2020.
- [26] M. A. Sanmartin Castillo, “Two terminal devices for the ciss effect analytical and modeling,” B.S. thesis, Universidad de Investigación de Tecnología Experimental Yachay, 2022.
- [27] M. A. Escobar Ordóñez, “Modeling of chiral induced spin selectivity effect under a magnetic field perturbation,” B.S. thesis, Universidad de Investigación de Tecnología Experimental Yachay, 2022.
- [28] W. O. Amrein, A. M. Hinz, and D. B. Pearson, *Sturm-Liouville theory: past and present*. Springer Science & Business Media, 2005.
- [29] S. J. B. Tom Lancaster, *Quantum Field Theory for the Gifted Amateur*. Oxford University Press, 2014. [Online]. Available: <http://gen.lib.rus.ec/book/index.php?md5=8673f60f9fded3dcb00a475c3fc61999>
- [30] D. N. Zubarev, “Double-time green functions in statistical physics,” *Soviet Physics Uspekhi*, vol. 3, no. 3, p. 320, 1960.
- [31] S. Datta, *Electronic Transport in Mesoscopic Systems*, ser. Cambridge Studies in Semiconductor Physics and Microelectronic Engineering. Cambridge University Press, 1997. [Online]. Available: <http://gen.lib.rus.ec/book/index.php?md5=664157630de544455f0d8a7491f70963>
- [32] J.-W. Jiang, J.-S. Wang, and B. Li, “A nonequilibrium green’s function study of thermoelectric properties in single-walled carbon nanotubes,” *Journal of Applied Physics*, vol. 109, no. 1, 2011.
- [33] P.-H. Chang, F. Mahfouzi, N. Nagaosa, and B. K. Nikolić, “Spin-seebeck effect on the surface of a topological insulator due to nonequilibrium spin-polarization parallel to the direction of thermally driven electronic transport,” *Physical Review B*, vol. 89, no. 19, p. 195418, 2014.

- [34] S.-g. Cheng, “Spin thermopower and thermoconductance in a ferromagnetic graphene nanoribbon,” *Journal of Physics: Condensed Matter*, vol. 24, no. 38, p. 385302, 2012.
- [35] McGraw-Hill, *McGraw Hill Encyclopedia of Science Technology*, 10th ed., ser. McGraw Hill Encyclopedia of Science and Technology. McGraw-Hill Professional, 2007, vol. Volume 10. [Online]. Available: <http://gen.lib.rus.ec/book/index.php?md5=75ac9cc6cb87e5b42f37648aba2608d1>
- [36] D. Nozaki, S. M. Avdoshenko, H. Sevincli, and G. Cuniberti, “Quantum interference in thermoelectric molecular junctions: A toy model perspective,” *Journal of applied physics*, vol. 116, no. 7, 2014.
- [37] Y. Li, J. A. Mol, S. C. Benjamin, and G. A. D. Briggs, “Interference-based molecular transistors,” *Scientific Reports*, vol. 6, no. 1, p. 33686, 2016.
- [38] C. Nappi, F. Romeo, L. Parlato, F. Di Capua, A. Aloisio, and E. Sarnelli, “Quantum interference in single-molecule superconducting field-effect transistors,” *The Journal of Physical Chemistry C*, vol. 122, no. 21, pp. 11 498–11 504, 2018.
- [39] P. Gehring, J. M. Thijssen, and H. S. van der Zant, “Single-molecule quantum-transport phenomena in break junctions,” *Nature Reviews Physics*, vol. 1, no. 6, pp. 381–396, 2019.
- [40] N. L. Plaszkó, P. Rakyta, J. Cserti, A. Kormányos, and C. J. Lambert, “Quantum interference and nonequilibrium josephson currents in molecular andreev interferometers,” *Nanomaterials*, vol. 10, no. 6, p. 1033, 2020.
- [41] Q.-f. Sun, J. Wang, and T.-h. Lin, “Resonant andreev reflection in a normal-metal–quantum-dot–superconductor system,” *Physical Review B*, vol. 59, no. 5, p. 3831, 1999.
- [42] T. Domański, A. Donabidowicz, and K. Wysokiński, “Influence of pair coherence on charge tunneling through a quantum dot connected to a superconducting lead,” *Physical Review B—Condensed Matter and Materials Physics*, vol. 76, no. 10, p. 104514, 2007.

- [43] T. Rejec, R. Žitko, J. Mravlje, and A. Ramšak, “Spin thermopower in interacting quantum dots,” *Physical Review B—Condensed Matter and Materials Physics*, vol. 85, no. 8, p. 085117, 2012.
- [44] A. Calle, M. Pacheco, and P. Orellana, “Fano effect and andreev bound states in t-shape double quantum dots,” *Physics Letters A*, vol. 377, no. 21-22, pp. 1474–1478, 2013.
- [45] G. Benenti, G. Casati, K. Saito, and R. S. Whitney, “Fundamental aspects of steady-state conversion of heat to work at the nanoscale,” *Physics Reports*, vol. 694, pp. 1–124, 2017.
- [46] L. López Gómez, “Transporte electrónico en materiales cuánticos,” 2022.
- [47] S. Datta, *Quantum Transport: Atom to Transistor*, 2nd ed. Cambridge University Press, 2005. [Online]. Available: <http://gen.lib.rus.ec/book/index.php?md5=f3d69e2c70bc61c136337f786ae4042b>
- [48] K.-I. Uchida, S. Takahashi, K. Harii, J. Ieda, W. Koshibae, K. Ando, S. Maekawa, and E. Saitoh, “Observation of the spin seebeck effect,” *Nature*, vol. 455, no. 7214, pp. 778–781, 2008.
- [49] K. Michaeli and R. Naaman, “Origin of spin-dependent tunneling through chiral molecules,” *The Journal of Physical Chemistry C*, vol. 123, no. 27, pp. 17 043–17 048, 2019.
- [50] F. S. C. Jr., *Waves (Berkeley Physics Course, Volume 3)*. Mcgraw-Hill Book Comp., 1968. [Online]. Available: <http://gen.lib.rus.ec/book/index.php?md5=0580745cb47c796dbb3963a7b6945367>
- [51] C. M. Finch, V. M. García-Suárez, and C. J. Lambert, “Giant thermopower and figure of merit in single-molecule devices,” *Phys. Rev. B*, vol. 79, p. 033405, Jan 2009. [Online]. Available: <https://link.aps.org/doi/10.1103/PhysRevB.79.033405>
- [52] P. Trocha and J. Barnaś, “Large enhancement of thermoelectric effects in a double quantum dot system due to interference and coulomb correlation

phenomena,” *Phys. Rev. B*, vol. 85, p. 085408, Feb 2012. [Online]. Available: <https://link.aps.org/doi/10.1103/PhysRevB.85.085408>

- [53] V. M. García-Suárez, R. Ferradás, and J. Ferrer, “Impact of fano and breit-wigner resonances in the thermoelectric properties of nanoscale junctions,” *Phys. Rev. B*, vol. 88, p. 235417, Dec 2013. [Online]. Available: <https://link.aps.org/doi/10.1103/PhysRevB.88.235417>